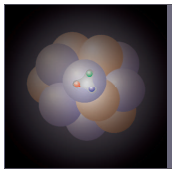

Institut für
Theoretische Physik I

JUSTUS-LIEBIG-
UNIVERSITÄT
GIESSEN

Kaon and Pion production at CBM energies

Diplomarbeit

presented by

Markus Wagner

from Giessen

Institut für Theoretische Physik I
Justus-Liebig-Universität Giessen

Giessen, March 2004

Contents

1 Introduction **1**

2 The BUU Model **5**
2.1 The BUU equation 5
2.1.1 Relativistic generalisation 7
2.1.2 The Potential 8
2.2 Considered Particles 9
2.3 The Collision Term 9
2.3.1 Baryon-Baryon Reactions 9
2.3.2 Meson-Baryon Reactions 13
2.3.3 Meson-Meson Reactions 14

3 The Fritiof Model **17**
3.1 The Lund Model 18
3.1.1 The fragmentation function 22
3.1.2 Massive quarks and baryons 25
3.1.3 Annihilation processes 27
3.1.4 The Formation time 31
3.1.5 Comparison to data 32
3.1.6 πN Collisions 33

4 From proton induced reactions to heavy-ion collisions **39**
4.1 Proton induced Reactions 39
4.2 Si+Au 41
4.3 Heavy-Ion Collisions 48
4.3.1 Centrality selection 48
4.3.2 Particle yields at 10.7 A·GeV/c 50
4.3.3 Strangeness production 54

5 Excitation Functions **59**
5.1 The Statistical Model 67
5.1.1 The Grand Canonical ensemble 69
5.1.2 The exact conservation of charges 70

5.1.3 Results 72

6 Off-shell pions, resonance lifetimes and string-string collisions 75
6.1 Off-shell pions 75
6.2 Resonance lifetimes 80
6.3 String-String collisions 82

7 Summary and Outlook 87

A Deutsche Zusammenfassung 91

Chapter 1

Introduction

During the first few microseconds after the big bang the universe went through a phase transition where the quarks and gluons were confined into hadrons. One aim of heavy-ion physics is to create the reverse process, i.e. to deconfine the hadrons into quarks and gluons. This state of matter is called the quark-gluon plasma. In Fig. 1.1 one sees the phase diagram of QCD according to our present understanding as a function of density and temperature. Accelerator facilities like RHIC (Relativistic Heavy Ion Collider) or the LHC (Large Hadron Collider) try to reach the phase boundary with very high temperatures and low baryon density (cf. Fig. 1.1). Another possibility to reach the quark gluon plasma is to create a high baryon density, which is expected to be highest at beam energies around 30 A·GeV [KL95]. The reason for the high densities is that the collision partners are stopped to a certain amount. So they cannot leave the collision zone as fast as the new particles enter the collision zone and therefore high densities are created. Pioneering work at large baryon densities was done at the AGS (Alternating Gradient Synchrotron) in Brookhaven, where the energy range up to 15 A·GeV was explored. CBM (Compressed Baryon Matter), the future facility at GSI, will provide beams from 2 A·GeV to 40 A·GeV and one aim is to scan for indications of the deconfinement phase transition.
One believes that an indirect signal for the quark-gluon plasma is an enhancement of strangeness production. The main qualitative idea, which was first suggested by Rafelski and Müller [RM82], is that the strange quarks are thought to be produced more easily via the fusion of gluons in that deconfined state as compared to the production in highly threshold suppressed inelastic hadronic collisions. That effect should then be seen most easily in the most abundant strange particles, the kaons. At the AGS and the SPS the K^+/π^+ ratio was studied and one found indeed a maximum in the ratio at about 30 A·GeV [A$^+$02].
The underlying theory which describes the dynamics of quarks and hadrons is the Quantum Chromodynamics (QCD). In QCD the exchange particles are the gluons, which are the analogue of the photons of QED (Quantum Electrodynamics). Unlike the photons, the gluons carry a charge themselves. Therefore they

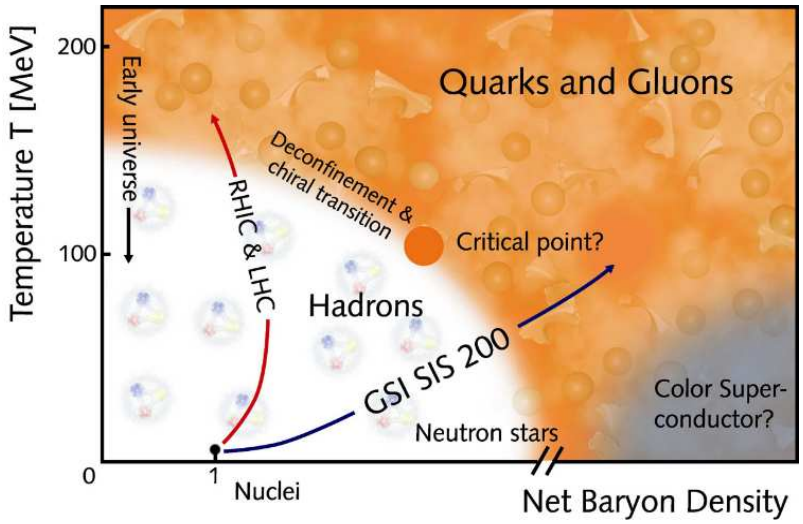

Figure 1.1: The QCD-phase diagram as a function of density and temperature taken from [KHu].

can also interact with each other, which leads to the peculiar property of QCD that the coupling constant increases at low momentum transfers. Due to the increase of the coupling constant, perturbation theory is not applicable at low energies and the confinement and the deconfinement cannot be understood from QCD calculations. The only hints at which temperatures the phase transition might occur come from lattice QCD calculations and they suggest a critical temperature $T_c \approx 150 - 180$ MeV for the deconfinement phase transition.
In this work we will study kaon and pion yields and especially the K^+/π^+ ratio within a transport model based on the BUU equation. Similar studies have already been performed with other codes, as for example RQMD (Relativistic Quantum Molecular Dynamics) [WLS+99] or HSD (Hadron String Dynamics) and UrQMD (Ultra-relativistic Quantum Molecular Dynamics) [WBCS03]. The RQMD model explained the ratio in terms of hadronic rescattering and has been in agreement with data. HSD and UrQMD did not reproduce the peak in the ratio but in their calculations the discrepancy were due to the pions and not to the kaons. We will come back to that issue in Chapter 5.
The energy range, we are interested in, is from 2 A·GeV up to 40 A·GeV. The problem in that energy range is that one has to deal with different kind of reactions and degrees of freedom. At the lower energies, for example, one has to deal with resonance scattering, whereas at the higher energies we describe reactions within a string model. In the first chapter we will present our model and show its results in elementary reactions. The next chapter is devoted to the most important ingredient (at CBM energies), the string model. Then we will work our way from proton induced reactions to heavy-ion collisions and we will put emphasis

on the development of the K^+ and π^+ rapidity spectra. After we have studied the system size dependence for strangeness production, we will study the energy dependence. That will be done in Chapter 5, where we will show the excitation functions in comparison to data and other models. The thermal model will also be discussed and compared to our model. We will see that our model is not able to reproduce the peak, which exists in the data. Therefore we will study the influence of some modifications of our model. In particular we will show the influence of off-shell effects and resonance life times on the particle production and we will discuss string-string collisions. Finally we will close the work with a summary and an outlook.

Chapter 2

The BUU Model

In the present work we describe heavy-ion collisions with a transport theory based on the Boltzmann-Uehling-Uhlenbeck (BUU) equation. This equation describes the space-time evolution of a many-body system under the influence of a mean-field potential and a collision term. Since we have performed most of the calculations in the cascade modus, which means without potential, we will focus on the collision term in our discussion and only give a brief description of the BUU equation itself.
The model, which is used in the present study, is described in detail in [Eff99]. We will try to give a self contained overview but we will also often refer to that work. In [Eff99], however, the model is not used for high-energy heavy-ion collisions and the description of the string model is very short. Therefore we will put emphasis on those parts and on the things which have changed.

2.1 The BUU equation

The BUU equation is an equation for the phase-space density $f(\vec{r},\vec{p},t)$. We will first write down the equation and afterwards briefly discuss its structure. For a derivation we refer to the literature [KB62, Dan84, BM90]. The BUU equation is given by

$$\left(\frac{\partial}{\partial t}+\frac{\partial H_{mf}}{\partial \vec{p}}\frac{\partial}{\partial \vec{r}}-\frac{\partial H_{mf}}{\partial \vec{r}}\frac{\partial}{\partial \vec{p}}\right) f(\vec{r},\vec{p},t)=\Sigma^{<}(1\pm f)-\Sigma^{>}f \tag{2.1}$$

with

$$\begin{aligned}\Sigma^{<}(1\pm f)-\Sigma^{>}f=&\int \frac{d^3p_2}{(2\pi)^3}\frac{d^3p_3}{(2\pi)^3}\frac{d^3p_4}{(2\pi)^3}(2\pi)^4\delta^{(4)}(p+p_2-p_3-p_4)\\ &\times|M|^2(f_3f_4(1\pm f_2)(1\pm f)-ff_2(1\pm f_3)(1\pm f_4)),\end{aligned} \tag{2.2}$$

where M is the invariant matrix element, $f_i=f(\vec{r}_i,\vec{p}_i,t)$ the phase-space density for one particle species and H_{mf} is the Hamiltonian which is in a non-relativistic

setting

$$H(\vec{r},\vec{p},t) = \frac{\vec{p}^2}{2m} + U(\vec{r},\vec{p},t) \tag{2.3}$$

and $U(\vec{r},\vec{p},t)$ is the single-particle mean-field potential. We will discuss the relativistic Hamiltonian in Section 2.1.1 and 2.1.2.
If the right hand side of Eq. (2.1) is zero, the equation is also called the Vlasov equation. The meaning of that equation is easy to see, if one recalls Liouville's theorem which says that the phase-space density along the phase-space trajectory of a member of the ensemble is constant

$$\frac{df_N}{dt} = 0. \tag{2.4}$$

$f_N = f_N(\vec{r}_1,\vec{p}_1,\ldots,\vec{r}_N,\vec{p}_N,t)$ is the N-body phase-space density. If one neglects the dynamical correlations between the particles and assumes that the N-body phase-space density can be written as a product of the one body phase-space densities

$$f_N(\vec{r}_1,\vec{p}_1,\ldots,\vec{r}_N,\vec{p}_N,t) = \prod_{i=1}^{N} f_1(\vec{r}_i,\vec{p}_i,t), \tag{2.5}$$

we get the Vlasov equation

$$\frac{df}{dt} = \frac{\partial f}{\partial t} + \frac{\partial H}{\partial \vec{r}}\frac{\partial f}{\partial \vec{p}} - \frac{\partial H}{\partial \vec{p}}\frac{\partial f}{\partial \vec{r}} = 0. \tag{2.6}$$

So the left hand side of Eq. (2.1) describes the time evolution of the phase-space density of a system of non-interacting particles under the influence of a potential U.
In situations, we are interested in, e.g. a heavy-ion collision, we cannot neglect the hard short-ranged interactions between the particles and therefore we need the right hand side of Eq. (2.1), which is called the collision term. We want to discuss the structure of the collision term by looking at a two body process

$$1 + 2 \rightarrow 3 + 4. \tag{2.7}$$

The right hand side of Eq. (2.1) is made up of two terms, the gain term $\Sigma^{<}(1 \pm f)$ and the loss term $\Sigma^{>} f$. The loss term describes the possibility of a particle to scatter out from the phase-space cell, we are looking at. The integral is performed over all possible collision partners, i.e. over p_2 and over all possible final states with momenta p_3 and p_4. The probability for the scattering process is proportional to the density of the initial state, which is taken care of by the factor $f_1 f_2 (f_1 \equiv f)$. In case of fermions, the final state is Pauli blocked, which is expressed by including the factors $(1 - f_3)$ and $(1 - f_4)$. In case of bosons the final state is Bose enhanced and the factors change to $(1 + f_3)$ and $(1 + f_4)$. The transition probability is given by the cross section, which is proportional to the

invariant matrix element squared $|M|^2$, which explains the factor $|M|^2$. Similar, the gain term describes a scattering into the phase-space cell under consideration. The processes which are taken into account in the present model are described in Section 2.3.
For resonances, we actually solve in our model a slightly modified transport equation, where one does not use the on-shell approximation :

$$\left(\frac{\partial}{\partial t}+\frac{\partial H_{mf}}{\partial \vec{p}}\frac{\partial}{\partial \vec{r}}-\frac{\partial H_{mf}}{\partial \vec{r}}\frac{\partial}{\partial \vec{p}}\right)F(\vec{r},\vec{p},t,\mu)=\Sigma^{<}(1\pm f)\mathcal{A}-\Sigma^{>}F, \tag{2.8}$$

where $F(\vec{r},\vec{p},t,\mu)=f(\vec{r},\vec{p},t,\mu)\mathcal{A}(\vec{r},\vec{p},t,\mu)$ is the spectral distribution function, $\mathcal{A}$ is the spectral function given by

$$\mathcal{A}(\vec{r},\vec{p},t,\mu)=\frac{2}{\pi}\frac{\mu^2\Gamma_{tot}(\vec{r},\vec{p},t,\mu)}{(\mu^2-M_0^2)^2+\mu^2\Gamma_{tot}(\vec{r},\vec{p},t,\mu)} \tag{2.9}$$

and μ is the mass of the resonance. $\mathcal{A}$ is normalized according to the measure $d\mu$ instead of $dp_0/2\pi$. For a more detailed description we refer to [Eff99].
If there are N particle species in the code, we have to solve a coupled set of N differential equations

$$D_i f_i = I_i(f_1,\ldots,f_N). \tag{2.10}$$

D_i is a differential operator, representing the left hand side of Eq. (2.8) and I_i is the collision integral, which in case of N particle species might depend on N one body phase-space densities. Solving such a set of equations is analytically out of reach and so we have to rely on an approximation scheme. The method we use to solve those equations is the test-particle method, where the spectral distribution function is approximated by a discrete density of a certain number of so called test particles

$$F(\vec{r},\vec{p},t,\mu)=\frac{1}{N}\sum_i \delta(\vec{r}-\vec{r}_i(t))\frac{(2\pi)^3}{g}\delta(\vec{p}-\vec{p}_i(t))\delta(\mu-\mu_i(t)), \tag{2.11}$$

where N is the number of test particles per physical particle and g is the degeneration factor in case of inner degrees of freedom. The normalisation is again suited for an integration over $d\mu$. For a detailed description of the numerical realisation we refer to [Eff99].

2.1.1 Relativistic generalisation

In order to get a relativistic generalisation of Eq. (2.1), we use a relativistic Hamiltonian and we modify the collision integral. The relativistic Hamiltonian is given by

$$H_{mf}=\sqrt{(M_0+U_S)^2+(\vec{\Pi})^2}+U_V^0, \tag{2.12}$$

where U_S is a scalar potential, U_V is a vector potential and

$$\Pi = p - U_V \tag{2.13}$$

the kinetic four-momentum (cf. [Eff99]).
The collision integral changes to (cf. [Eff99])

$$\begin{aligned}\Sigma^<(1 \pm f) - \Sigma^> f = \frac{1}{2\Pi_0} \int & \frac{d^3\Pi_2}{(2\pi)^3 2\Pi_2^0} \frac{d^3\Pi_3}{(2\pi)^3 2\Pi_3^0} \frac{d^3\Pi_4}{(2\pi)^3 2\Pi_3^0} \\ & \times (2\pi)^4 \delta^{(4)}(p + p_2 - p_3 - p_4) \frac{1}{2} |M|^2 \\ & \times (f_3 f_4 (1 \pm f_2)(1 \pm f) - f f_2 (1 \pm f_3)(1 \pm f_4)).\end{aligned} \tag{2.14}$$

2.1.2 The Potential

In the last section we introduced the relativistic Hamiltonian and the relativistic collision integral, where one encounters the vector potential U_V. For numerical simplicity we set $U_V = 0$, but we will account for it in the following different way. The four current j_μ is given by an integration over the phase-space density

$$j_\mu = g \int \frac{d^3p}{(2\pi)^3} \frac{p^\mu}{p^0} f(\vec{r}, \vec{p}, t), \tag{2.15}$$

where g is the degeneracy of the one particle state. The local restframe is the system where the spacial components of j_μ vanish. In that system the density is given by

$$\rho_{lrf} = \rho(\vec{r}) = \sqrt{j^\mu j_\mu}. \tag{2.16}$$

The potential is parametrized according to a suggestion of Welke et al. [WPK+88]

$$U(\vec{r}, \vec{p}) = A \frac{\rho(\vec{r})}{\rho_0} + B \left(\frac{\rho(\vec{r})}{\rho_0} \right)^\tau + \frac{2C}{\rho_0} g \int \frac{d^3p'}{(2\pi)^3} \frac{f(\vec{r}, \vec{p}')}{1 + \frac{(\vec{p} - \vec{p}')^2}{\Lambda^2}}. \tag{2.17}$$

Since that potential is numerically very expensive, we approximate the phase-space density by the phase-space density at temperature $T = 0$:

$$f(\vec{r}, \vec{p}) = \theta(p_F(\vec{r}) - |\vec{p}|), \tag{2.18}$$

where the local Fermi momentum p_F is given by

$$p_F(\vec{r}) = \left(\frac{6}{g} \pi^2 \rho(\vec{r}) \right)^{\frac{1}{3}}. \tag{2.19}$$

We take that potential to be the zeroth component of the vector potential in the local restframe, so that H_{mf}^{lrf} is given by

$$H_{mf}^{lrf} = \sqrt{M_0^2 + \vec{p}_{lrf}^{\,2}} + U_{lrf}(\vec{r}, \vec{p}). \tag{2.20}$$

The effective scalar potential is now defined such that

$$(U_S + M_0)^2 + \vec{p}^2_{lrf} = (\sqrt{M_0^2 + \vec{p}^2_{lrf}} + U_{lrf})^2. \tag{2.21}$$

Setting $U_V = 0$ is therefore not an approximation because in a spin symmetric system in the local restframe $\vec{U}_V$ vanish anyway.

2.2 Considered Particles

In Tab. 2.1, 2.2, 2.3 and 2.4 we list all particles, which are incorporated in the BUU model. We also list the charmed particles for completeness, although they have not much influence on the dynamics of the reactions, we are looking at. The parameters are taken from the work of Manley [MS92].

2.3 The Collision Term

In this section we will summarize the interactions which are implemented in the BUU model. In general the collisions are divided into three sections: the baryon-baryon reactions, the baryon-meson reactions and the meson-meson reactions, which will be described in the next three subsections. The general criterion for collisions is a semiclassical geometrical method, which is based on a relativistic algorithm from Kodama et al. [K$^+$84]. First we calculate the distance of the particles in their center-of-mass system, which is then compared to a maximal distance $b_{max} = \sqrt{\sigma_{\rm tot}/\pi}$, which is the radius of the total cross section $\sigma_{\rm tot}$ for the reaction. Then we determine if the current time step is the time step at which the particles reach their closest distance. If the distance in their center-of-mass system is smaller than b_{max} and they reach their closest distance in the time step under consideration the particles will collide and in case of several final states, the state is chosen by a Monte Carlo decision with the probability according to the respective exclusive cross sections.

2.3.1 Baryon-Baryon Reactions

For invariant energies of $\sqrt{s} > 2.6$ GeV we use the Fritiof model, which will be explained in Chapter 3 to describe baryon-baryon reactions. Below those energies the following reactions are taken into account

Resonance	Decay probabilities in %								
	$N\pi$	$N\eta$	$N\omega$	$K\Lambda$	$\Delta\pi$	$N\rho$	$N\Sigma$	$N^*\pi$	$\Delta\rho$
$N(938)$	0	0	0	0	0	0	0	0	0
$P_{33}(1232)$	100	0	0	0	0	0	0	0	0
$P_{11}(1440)$	69	0	0	0	22_P	0	9	0	0
$P_{11}(1535)$	51	43	0	0	0	3_S	1	2	0
$S_{11}(1650)$	89	3	0	0	2_D	3_S	2	1	0
$S_{11}(2090)$	10	0	0	0	6_D	49_S	5	30	0
$D_{13}(1520)$	59	0	0	0	5_S,15_D	21_S	0	0	0
$D_{13}(1700)$	1	0	0	0	$5_S, 79_D$	13_S	2	0	0
$D_{13}(2080)$	23	0	0	0	$3_S, 21_D$	26_S	27	0	0
$D_{15}(1675)$	47	0	0	0	53_D	0	0	0	0
$G_{17}(2190)$	22	0	49	0	0	29_D	0	0	0
$P_{11}(1710)$	9	0	0	37	49_P	3_P	2	0	0
$P_{11}(2100)$	15	0	0	2	24_P	27_P	32	0	0
$P_{13}(1720)$	13	0	0	0	0	87_P	0	0	0
P_{13}	26	0	30	0	0	44_P	0	0	0
$F_{15}(1680)$	70	0	0	0	$10_P, 1_F$	$5_P, 2_F$	12	0	0
$F_{15}(2000)$	8	0	0	0	12_P	$60_P, 15_F$	5	0	0
$F_{17}(1990)$	6	94	0	0	0	0	0	0	0
$S_{31}(1620)$	9	0	0	0	62_D	$25_S, 4_D$	0	0	0
$S_{31}(1900)$	4	0	0	0	16_D	$5_S, 33_D$	0	6	0
$D_{33}(1700)$	14	0	0	0	$74_S, 4_D$	8_S	0	0	0
$D_{33}(1940)$	18	0	0	0	$7_S, 40_D$	35_S	0	0	0
$D_{35}(1930)$	18	0	0	0	0	0	0	0	82_D
$D_{35}(2350)$	2	0	0	0	0	0	0	0	98_D
P_{31}	8	0	0	0	0	0	0	28	64_P
$P_{31}(1910)$	23	0	0	0	0	10_P	0	67	0
$P_{33}(1600)$	12	0	0	0	68_P	0	0	20	0
$P_{33}(1920)$	2	0	0	0	83_P	0	0	15	0
F_{35}	2	0	0	0	$28_P, 48_F$	22_P	0	0	0
$F_{35}(1905)$	12	0	0	0	1_P	87_P	0	0	0
$F_{37}(1950)$	38	0	0	0	18_F	0	0	0	44_F

Table 2.1: Included baryons with S=0 and their decay properties. The index at the decay probabilities corresponds to the relative angular momentum of the outgoing particles.

Resonance	Γ_0 [MeV]	Decay probabilities in %						
		$\Lambda\pi$	NK	$\Sigma\pi$	$\Sigma^*\pi$	$\Lambda\eta$	NK^*	$\Lambda^*\pi$
$\Lambda(1116)$	0	0	0	0	0	0	0	0
$\Sigma(1189)$	0	0	0	0	0	0	0	0
$P_{13}(1385)$	36	88	0	12	0	0	0	0
$S_{01}(1405)$	50	0	0	100	0	0	0	0
$D_{03}(1520)$	16	0	46	43	11	0	0	0
$P_{01}(1600)$	150	0	35	65	0	0	0	0
$P_{11}(1660)$	100	40	20	40	0	0	0	0
$S_{01}(1670)$	35	0	25	45	0	30	0	0
$D_{13}(1670)$	60	15	15	70	0	0	0	0
$D_{03}(1690)$	60	0	25	30	45	0	0	0
$S_{11}(1750)$	90	10	30	60	0	0	0	0
$D_{15}(1775)$	120	20	45	5	10	0	0	20
$S_{01}(1800)$	300	0	35	35	30	0	0	0
$P_{01}(1810)$	150	0	35	20	0	0	45	0
$F_{05}(1820)$	80	0	60	12	28	0	0	0
$D_{05}(1830)$	95	0	5	60	35	0	0	0
$P_{03}(1890)$	100	0	30	10	30	0	30	0
$F_{15}(1915)$	180	25	25	10	15	0	5	20
$G_{07}(2100)$	200	0	30	5	45	0	20	0
$F_{05}(2110)$	200	0	15	30	0	0	55	0

Table 2.2: Properties of the included baryons with S=-1.

baryon	M_0[MeV]	Γ_0[MeV]	S	C
Ξ	1315	0	-2	0
Ξ^*	1530	9	-2	0
Ω	1672	0	-3	0
Λ_C	2285	0	0	1
Σ_C	2455	0	0	1
Σ_C^*	2530	0	0	1
Ξ_C	2466	0	-1	1
Ξ_C^*	2465	0	-1	1
Ω_C	2704	0	-2	1

Table 2.3: Properties of the included baryons with S $<$ -1 or C=1.

Meson	M_0 [MeV]	Γ_0 [MeV]	J	I	S	C	decay channels
π	138	0	0	1	0	0	
η	547	$1.2 \cdot 10^{-3}$	0	0	0	0	$\gamma\gamma(40\%)$, $\pi^+\pi^-\pi^0(28\%), 3\pi^0(32\%)$
ρ	770	151	1	1	0	0	$\pi\pi$
σ	800	800	0	0	0	0	$\pi\pi$
ω	782	8.4	1	0	0	0	$\pi\pi(2\%), \pi^0\gamma(9\%)$, $\pi^+\pi^-\pi^0(89\%)$
η'	958	0.2	0	0	0	0	$\rho^0\gamma(31\%), \pi\pi\eta(69\%)$
ϕ	1020	4.4	1	0	0	0	$\rho\pi(13\%)$, $K\overline{K}(84\%), \pi^+\pi^-\pi^0(3\%)$
η_c	2980	0	0	0	0	0	
J/Ψ	3097	0	1	0	0	0	
K	496	0	0	$\frac{1}{2}$	1	0	
$\overline{K}$	496	0	0	$\frac{1}{2}$	-1	0	
K^*	892	50	1	$\frac{1}{2}$	1	0	$K\pi$
$\overline{K}^*$	892	50	1	$\frac{1}{2}$	-1	0	$\overline{K}\pi$
D	1869	0	0	$\frac{1}{2}$	0	1	
$\overline{D}$	1869	0	0	$\frac{1}{2}$	0	-1	
D^*	2007	0	1	$\frac{1}{2}$	0	1	
$\overline{D}^*$	2007	0	1	$\frac{1}{2}$	0	-1	
D_S	1969	0	0	0	1	1	
$\overline{D}_S$	1969	0	0	0	-1	-1	
D_S^*	2112	0	0	0	1	1	
$\overline{D}_S^*$	2112	0	0	0	-1	-1	

Table 2.4: Properties of the included mesons.

$$\begin{array}{rcl} NN & \rightarrow & NN \\ NN & \leftrightarrow & NR \\ NN & \leftrightarrow & \Delta\Delta \\ NN & \leftrightarrow & NN\pi \\ NN & \rightarrow & NN\omega \\ NR & \leftrightarrow & NR' \\ BB & \rightarrow & NYK \\ BB & \rightarrow & NY^*K \\ BB & \rightarrow & NNK\overline{K}, \end{array}$$

where N stands for a nucleon, R for a resonance, Y for a hyperon, Y^* for a hyperon resonance and B for a nucleon or a resonance except of Δ. The exact parametrisations and comparison to data can be looked up in [Eff99].

2.3.2 Meson-Baryon Reactions

Here we use the Fritiof model for invariant energies above 2.0 GeV. For $\sqrt{s} < 2.0$ GeV the collisions are treated via resonance production. In particular we use the Breit-Wigner formula

$$\sigma_{ab\rightarrow R\rightarrow f} = \frac{2J_R+1}{(2J_a+1)(2J_b+1)} \frac{4\pi}{S_{ab}p_{ab}^2} \frac{s\Gamma_{R\rightarrow ab}\Gamma_{R\rightarrow f}}{(s-(M_R^2))^2 + s\Gamma_{tot}^2}, \tag{2.22}$$

where p_{ab} is the center-of-mass momentum, $\sqrt{s}$ the invariant mass, M_R the pole mass of the resonance, $S_{ab} = 1/(m_a m_b)$ is a statistical factor, the J's are spins of the particles and the Γ's are the widths. Since we propagate resonances explicitly, we sum over all possible decay channels to get the cross sections for the resonance production only (for a detailed description see [Eff99]). If all resonances are included we overestimate the total cross section for $\pi^- p$ collisions. Therefore we neglect all resonances which are assigned one star in [MS92]. At pion momenta above 1.5 GeV the total cross section seems to saturate whereas the resonance cross section drops. We treat this discrepancy as a non resonant two-pion-production background

$$\sigma^{bg}_{\pi N\rightarrow N\pi\pi} = \sigma^{exp}_{\pi N\rightarrow X} - \sum_R \sigma_{\pi N\rightarrow R}. \tag{2.23}$$

If we neglect the one star resonances the $\pi^+ p$ cross section turns out to be too low and therefore we treat the discrepancy again as a non resonant background, which is equal to the contribution of the one star resonances.

$$\sigma^{bg}_{\pi p\rightarrow \pi p} = \sum_{R(1star)} \sigma_{\pi+p\rightarrow R\rightarrow \pi p} \tag{2.24}$$

$$\sigma^{bg}_{\pi p\to N\pi\pi} = \sum_{R(1star)} \sigma_{\pi+p\to R\to N\pi\pi} \tag{2.25}$$

In addition we consider the following non resonant processes explicitly

$$\begin{array}{rcl} \pi N & \leftrightarrow & \omega N \\ \pi N & \rightarrow & \omega\pi N \\ \omega N & \rightarrow & \pi\pi N \\ \omega N & \rightarrow & \omega N \\ \pi N & \leftrightarrow & \phi N \\ \phi N & \rightarrow & \pi\pi N \\ \phi N & \rightarrow & \phi N \\ \pi N & \leftrightarrow & \eta\Delta. \end{array}$$

For processes including an ω-meson we have to subtract the resonance contributions which couple to the $N\omega$-channel.
For strangeness production we included the following processes

$$\begin{array}{rcl} \pi N & \leftrightarrow & \Lambda K \\ \pi N & \leftrightarrow & \Sigma K \\ \pi N & \rightarrow & NK\overline{K} \\ \pi\Delta & \leftrightarrow & \Lambda K \\ \pi\Delta & \leftrightarrow & \Sigma K \\ \pi\Delta & \rightarrow & NK\overline{K}. \end{array}$$

For $\pi N \rightarrow \Lambda K$ again we have to subtract the resonance contributions. Those processes are important at the low AGS energies and of course below, whereas at higher energies those channels become unimportant in comparison to the string channels. We will discuss that in more detail in Section 4.3.3.
For processes involving strange particles the following reactions are incorporated

$$\begin{array}{rcl} \overline{K}N & \rightarrow & \overline{K}N \\ \overline{K}N & \leftrightarrow & \pi\Lambda \\ \overline{K}N & \leftrightarrow & \pi\Sigma \\ \overline{K}N & \leftrightarrow & \pi Y^* \\ KN & \rightarrow & KN \\ KN & \rightarrow & K\pi N. \end{array}$$

These reactions are important in order to get the right relation between strange mesons and strange baryons.
The parametrisations of all those processes can be looked up in [Eff99].

2.3.3 Meson-Meson Reactions

In the meson-meson channel the resonance cross sections are included according to the decay properties which are listed in Tab. 2.4. In addition we put in

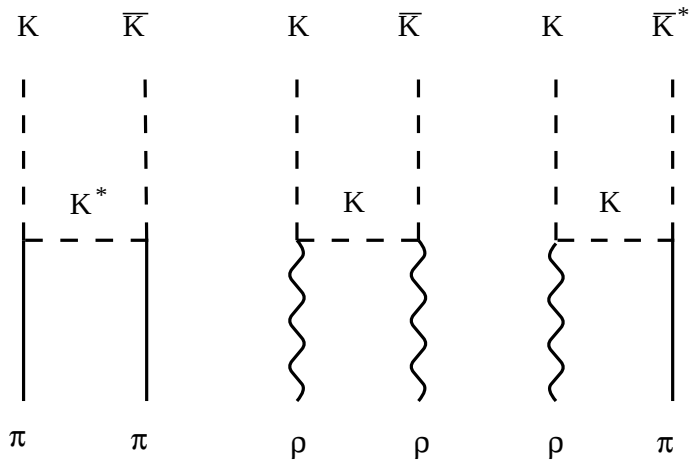

Figure 2.1: Feynman-diagrams for $MM \to K\overline{K}$.

background terms, which account for the strangeness production. In [BKWX91] the cross sections for $\pi\pi \to K\overline{K}$, $\pi\rho \to K\overline{K}$ and $\rho\rho \to K\overline{K}$ were calculated by considering the diagrams in Fig. 2.1. We use a parametrisation of $\pi\pi \to K\overline{K}$ from [CBM+97], which is based on these calculations.

$$\sigma_{\pi\pi\to K\overline{K}} = C6.075\text{mb}\left(1 - \frac{(2m_K)^2}{s}\right)^{0.76}, \tag{2.26}$$

where C is the Clebsch-Gordan coefficient for the respective isospin channels

$$C = \sum_I \mid \langle i_1 i_2 m_1 m_2 \mid i_1 i_2 I M\rangle \mid^2 \mid \langle i_3 i_4 m_3 m_4 \mid i_3 i_4 I M\rangle \mid^2 . \tag{2.27}$$

The sum runs over all possible isospin configurations and i_k and m_k are the total isospin and the z'th component of the particle k. The particles are numbered according to $(1 + 2 \to 3 + 4)$. For simplicity we take the same cross section for $\rho\rho \to K\overline{K}$ and $\pi\rho \to K\overline{K}$ since the isospin in the incoming channel is the same. This is not exactly the result from [BKWX91] as we will discuss later. For all other reactions with two nonstrange mesons in the incoming channel we assume a constant value of 2 mb for the cross section. The back reactions are included and their values are calculated according to detailed balance.
Now we briefly want to motivate our choice for the cross sections, we just described. In [BKWX91] the authors also studied medium effects and the result was that the cross section from Fig. 2.1 increase significantly. So in principal there is a lot of freedom to choose the value of the cross sections. In [BKWX91] and references therein the vacuum cross sections are always of the order of a few mb and therefore we think, that our choice of the strangeness production cross section for meson-meson reactions is reasonable. Since the elementary reactions

are not accessible experimentally, we have to check our choice of the cross sections in heavy-ion collisions by checking the yields of kaons, which will be done later. That will give us of course just a rough estimate of our cross sections since many other collisions influence the dynamics.

Chapter 3

The Fritiof Model

At the energy regime we are interested in, we encounter the problem that we are not able to describe hadron-hadron collisions from first principles since we are at the non-perturbative region of QCD. So we have to rely on models, like the Lund string model [And87], which we want to discuss in the following.
The picture is that in a hadron-hadron collision there are many soft parton collisions which add up to a sizeable longitudinal momentum transfer. In the Fritiof model it is assumed that there is no exchange of color, like in other string models, e.g. the VENUS model [Wer93]. Now we want to describe how the momentum transfers are determined and in order to do that we will use lightcone coordinates which will turn out to be useful, especially when we describe the string fragmentation.
The lightcone coordinates are defined as follows

$$p^{\pm} = E \pm p_z \tag{3.1}$$

and so the four momentum of two hadrons with masses m_1 and m_2 in the center-of-mass system with four momenta in usual coordinates $(E, p, 0_t)$, $(E, -p, 0_t)$, are given by

$$P_1^i = \left(p_{1+}, \frac{m_1^2}{p_{1+}}, 0_t\right), \qquad P_2^i = \left(\frac{m_2^2}{p_{2-}}, p_{2-}, 0_t\right), \tag{3.2}$$

where i stands for initial. It is easy to see that

$$p_{k+}p_{k-} = m_k^2 \qquad , \qquad k = 1, 2. \tag{3.3}$$

After the momentum transfer $Q = (Q_+, Q_-, \vec{Q}_t)$ we get two excited hadrons with four momenta

$$P_1^f = \left(p_+ - Q_+, \frac{m_1^2}{p_+} + Q_-, \vec{Q}_t\right), \; P_2^i = \left(\frac{m_2^2}{p_-} + Q_+, p_- - Q_-, \vec{Q}_t\right). \tag{3.4}$$

The momentum transfer scales according to the following distribution

$$\text{Prob} \sim \frac{dP_{1-}^f}{P_{1-}^f}\frac{dP_{2+}^f}{P_{2+}^f}, \tag{3.5}$$

where

$$P^f_{1-} \equiv \frac{m_1^2}{p_{1+}} + Q_-, \qquad P^f_{2+} \equiv \frac{m_2^2}{p_{2-}} + Q_+. \tag{3.6}$$

This longitudinal momentum transfer determines which energy will be available for particle production.
The transverse momentum transfer is distributed according to a Gauss function with $\langle Q_t^2 \rangle = 0.01$ GeV^2/c^2, which corresponds to $\sigma = 0.2$.

$$\text{Prob}(Q_t) \approx \frac{1}{\sqrt{\pi}\sigma} \exp\left(\frac{-Q_t^2}{\sigma^2}\right) \tag{3.7}$$

An important point is that the Fritiof model does not reproduce the experimentally known elastic cross sections and so the decision whether an elastic or an inelastic process is happening is put in by hand [Fal].
Once the excited hadrons are generated they decay by the Lund fragmentation which will be described in the next section.

3.1 The Lund Model

Most of the informations about the Lund Model, which will be presented in the following have been obtained from [And98]. We start out by looking at a massless relativistic string in one dimension. The string plays the role of a constant force field acting on a charge and an anticharge, which sit at the endpoints. We identify the charges as massless quark and antiquark with triplet 3, resp. $\overline{3}$, color charges. They form a so called yoyo hadron, which is in that model a meson. We neglect the masses of the quarks and the production of baryons for simplicity. There are no conceptual differences in implementing those issues and we discuss these points later.
The equation of motion for a particle under a constant force $-\kappa$ is simply

$$\frac{dp}{dt} = -\kappa. \tag{3.8}$$

In our case for massless particles, it is easy to show that the model is covariant, since (with $c = 1$), we know that $E = p$ and $x = t$ and after a Lorentz boost we have

$$t' = \gamma(t - \beta x) = \gamma(1 - \beta)t, \qquad p' = \gamma(p - \beta E) = \gamma(1 - \beta)p \tag{3.9}$$

and therefore

$$\frac{dp}{dt} = \frac{dp'}{dt'}.$$

The solution to the equation of motion is obviously

$$p(t) = p_0 - \kappa t \equiv \kappa(t_0 - t). \tag{3.10}$$

We also need an expression for the kinetic energy, which we get by

$$\frac{dE}{dx} = \frac{dE}{dp}\frac{dp}{dt}\frac{dt}{dx} = -\kappa \tag{3.11}$$

and the corresponding equation of motion is

$$E(x) = E_0 - \kappa x \equiv \kappa(x_0 - x). \tag{3.12}$$

Now we describe the yoyo hadrons in more detail. In Fig. 3.1 one can see the trajectories of the particles together with their energy at certain times. At $t = 0$ the particles both have lightcone momenta $2E_0$ and they start to separate and to stretch the color field in between them. At time t_A they are a distance $2t_A$ apart and their remaining energy is $E_0 - \kappa t_A$. At time $t_B = E_0/\kappa$ they lost all their energy and they reverse the direction of motion. On the way back they eat up the color field between them and therefore increase their energy until they meet again and they restored their original energy E_0. Now the whole motion starts again but the role of the q and the $\overline{q}$ are exchanged. We note that the total area $\overline{A}$ spanned by the force field in space-time is related to the mass m of the system by

$$\kappa^2\overline{A}^2 = \kappa^2\frac{4E_0^2}{\kappa^2} = m^2. \tag{3.13}$$

In Fig. 3.2 we see the yoyo mode after a boost in the positive direction. The sides of the rectangle now change from $2E_0$ to $2E_0\exp(-y)$ and $2E_0$ to $2E_0\exp(y)$ respectively, according to the transformation properties of the lightcone coordinates under a Lorentz boost.

The fragmentation is described by assuming that if the mass of the state is larger than the mass of a hadron, new $q\overline{q}$-pairs can be produced along the field. This corresponds to a breaking of the strings. The pair will immediately start to separate due to the attraction of the original quarks and antiquarks. In that way they will eat up the field energy between them and so there is no field between the newly produced pair. Now the original quarks and the newly produced quarks build together two hadrons and the string in between can break up again (see Fig. 3.3). That procedure goes on until all yoyo states have the masses of physical hadrons.

Now we want to discuss the ordering of the process and in order to do that we have to consider the energy momentum properties of the string pieces. We look at a state with one quark produced at the vertex A and the other quark produced at B with space-time coordinates and energy momentum given by $(x_j, t_j), (p_j, E_j)$, for $j = A, B$ (cf. Fig. 3.4). According to the equations of motion (3.10, 3.12), the total energy E and total momentum p of the two quarks meeting at O is

$$E = E_A + E_B = \kappa(x_A - x_B), \tag{3.14}$$

$$p = p_A + p_B = \kappa(t_A - t_B). \tag{3.15}$$

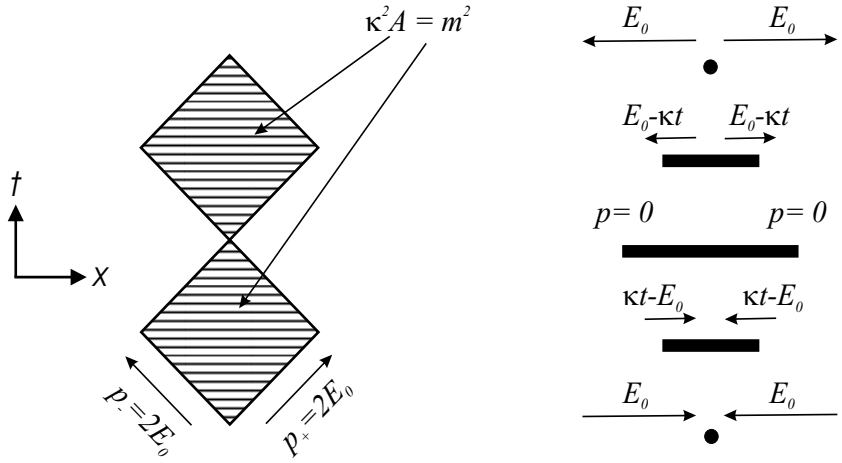

Figure 3.1: The left side shows the space-time diagram for the motion of a $q\overline{q}$-state, in which particles always have the same energy, i.e. the yoyo mode at rest. On the right hand side, the arrowed lines show the energy of the particles and the thick lines correspond to their separation, i.e. the field in between. The time evolution of the right hand side corresponds to only **one** of the squares of the left hand side.

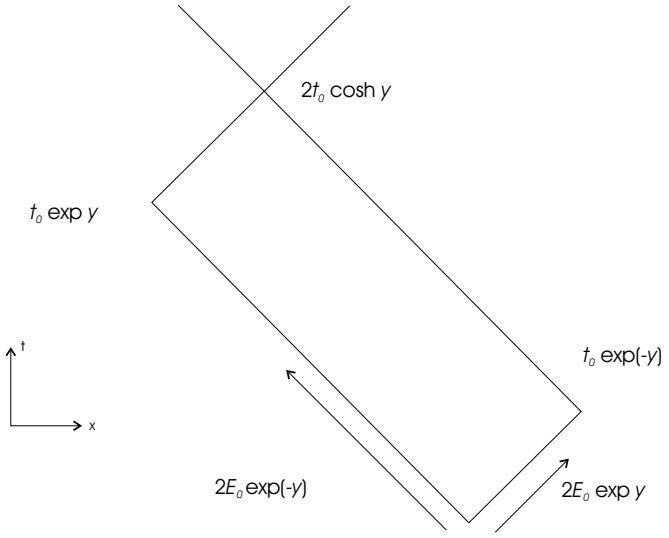

Figure 3.2: Space-time diagram of the $q\overline{q}$-pair after a boost in the positive direction.

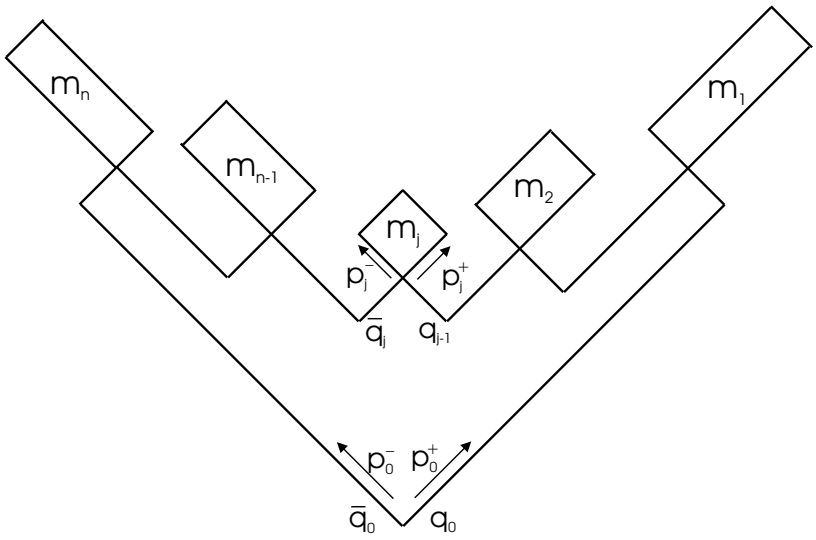

Figure 3.3: The fragmentation of a string.

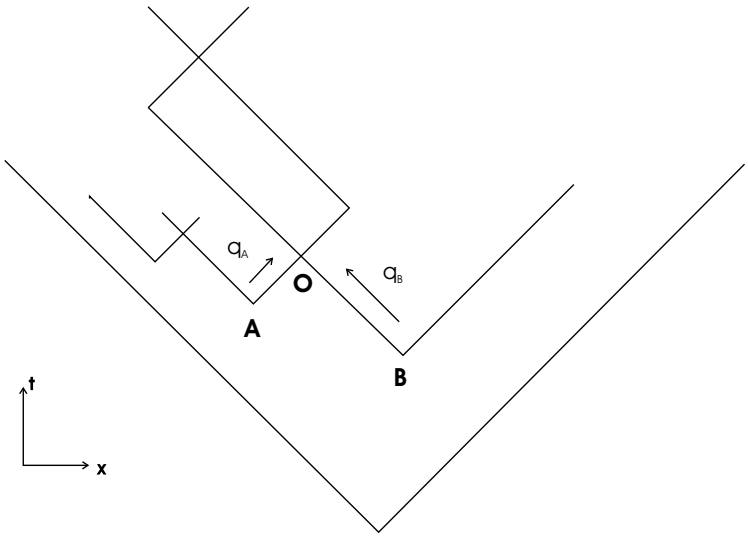

Figure 3.4: The Formation of a hadron from a quark coming from vertex A and a quark originating from B.

So we know that the mass of our meson is given by

$$m^2 = E^2 - p^2 = \kappa^2((x_A - x_B)^2 - (t_A - t_b)^2). \tag{3.16}$$

An important consequence of that equation is that the distance of the vertices A,B must be spacelike in order to have a real mass. Therefore the vertices are not causally connected and the vertices have to be independent of each other. This fact will be used when we derive the fragmentation function.
Another important consequence of Eq. (3.16) is that we have only one degree of freedom for every yoyo meson, namely $p_+ = E + p$ or $p_- = E - p$. That provides us with a way of ordering the decay process, namely along one of the lightcones. We start with a quark-antiquark pair $q_0, \overline{q}_0$ with lightcone energy-momenta p_0^+, p_0^- (cf. Fig. 3.3). If we order the process along the positive lightcone, we will first decide, which part of p_0^+ the first hadron gets. Once we decided, we know p_1^- by the mass constraint and we can go to the next vertex. So at the j'th vertex we make a decision for p_j^+ and the step in the negative lightcone p_j^- is always pinned down by the mass constraint. The same ordering can of course also be achieved along the negative lightcone. We continue the procedure until all states have physical masses. For the last step this is a problem since we are additionally constrained by energy-momentum conservation or in other words the p_j^+ for $j = 1, n$ have to add up to p_0^+. If that is not possible in the last step, one has to go through the whole iteration process again. In practice there are two circumstances, which weaken the constraints. The first one is that there are mesons and baryons with a width and so the mass constraint gets flexible. The second point is that we also assign a transverse momentum to the particles, which gives us another degree of freedom in order to fulfill energy-momentum conservation and the mass relation.
In the next section we will derive the fragmentation function, which determines the distribution of the step sizes z along the lightcones.

3.1.1 The fragmentation function

First we will define a new variable, namely the scaled lightcone components

$$z_\pm = \frac{p^\pm}{p_0^\pm}.$$

This is the variable we want to find a distribution for. The only difference is that in the definition above z is scaling with the original light cone momenta p_0. In the fragmentation process we will choose z to scale with the remaining lightcone momentum at the vertex.
We consider two adjacent vertices A,B and a hadron of mass m being produced in between. This event can be described by taking a certain amount of steps along the positive lightcone to reach A and then one further step to reach B or

by taking a certain amount of steps along the negative lightcone to reach B and then one further step to A. We call the lightcone coordinates at A and B x_{+j}, x_{-j} with $j = A, B$. Then by introducing the probability distribution H we can write the probability to arrive at vertex A as

$$H'(A)dx_{+A}dx_{-A} \equiv H(\Gamma_A)d\Gamma_A dy_A \tag{3.17}$$

with

$$\Gamma_A = \kappa^2 x_{+A}x_{-A} \qquad \text{and} \qquad y_A = \frac{1}{2}\log\frac{x_{+A}}{x_{-A}}.$$

In Eq. (3.17) we also used that H can only depend upon Γ_A since that is the only Lorentz invariant available. The corresponding probability to arrive at vertex B going along the negative lightcone is

$$H(\Gamma_B)d\Gamma_B dy_B. \tag{3.18}$$

Now we introduce the probability distribution f, we are interested in. Taking another step from A to B, respectively B to A, is thus given by the probabilities

$$f(z_+)dz_+ \qquad \text{and} \qquad f(z_-)dz_-. \tag{3.19}$$

By using that the probability for a certain fragmentation should be the same for going along the negative lightcone as for going along the positive lightcone, we can equate the two joint probabilities and get

$$H(\Gamma_A)d\Gamma_A dy_A f(z_+)dz_+ = H(\Gamma_B)d\Gamma_B dy_B f(z_-)dz_-. \tag{3.20}$$

Since none of the distributions depend on y_A and y_B we can take dy_A and dy_B to be equal. Furthermore we find by looking at Fig. 3.5 the following relations between the variables left

$$\Gamma_A = (1 - z_-)W_A W_B, \tag{3.21}$$
$$\Gamma_B = (1 - z_+)W_A W_B, \tag{3.22}$$
$$m^2 = z_- z_+ W_A W_B. \tag{3.23}$$

So we can eliminate Γ_A, Γ_B, W_A and W_B. By building the Jacobian for the transformation from $\Gamma_A, z_+ \to z_-, z_+$ and $\Gamma_B, z_- \to z_-, z_+$ we find the relation

$$d\Gamma_A \frac{dz_+}{z_+} = d\Gamma_B \frac{dz_-}{z_-}. \tag{3.24}$$

Using those relations, Eq. (3.20) reduces to

$$H(\Gamma_A(z_+, z_-))z_+ f(z_+) = H(\Gamma_B(z_+, z_-))z_- f(z_-). \tag{3.25}$$

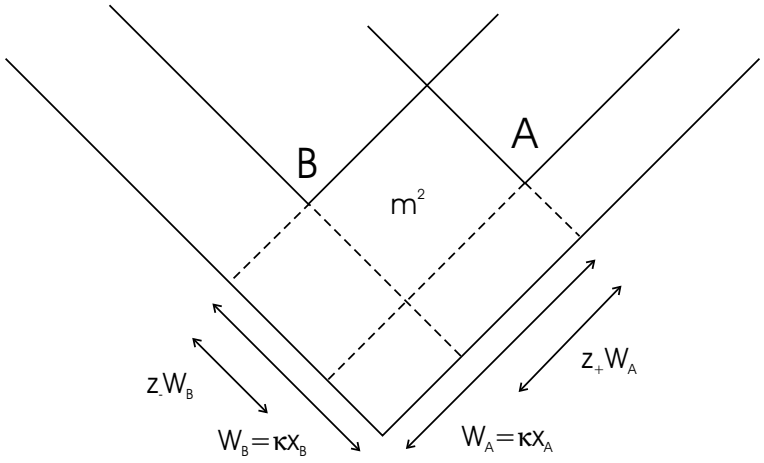

Figure 3.5: The production of a hadron with mass m between two adjacent vertices.

Taking the logarithm of that equation we obtain with $h(\Gamma) = \log H(\Gamma)$ and $g(z) = \log(zf(z))$

$$h(\Gamma_A) + g(z_+) = h(\Gamma_B) + g(z_-). \tag{3.26}$$

Now we differentiate with respect to z_+ and z_-, so that the g-dependence vanishes and after some algebra we are left with the following identity

$$\frac{dh(\Gamma_A)}{d\Gamma_A} + \Gamma_A \frac{d^2h(\Gamma_A)}{d\Gamma_A^2} = \frac{dh(\Gamma_B)}{d\Gamma_B} + \Gamma_B \frac{d^2h(\Gamma_B)}{d\Gamma_B^2}. \tag{3.27}$$

Since the left hand side depends only on Γ_A and the right side only on Γ_B, both sides have to be equal a constant, which we will call b. Then the differential equation we have to solve is

$$\frac{d}{d\Gamma}\left(\Gamma \frac{dh}{d\Gamma}\right) = -b. \tag{3.28}$$

By plugging in, one can easily check that the solution to that equation is

$$h(\Gamma) = -b\Gamma + a\log\Gamma + \log C \tag{3.29}$$

and therefore

$$H(\Gamma) = C\Gamma^a \exp(-b\Gamma). \tag{3.30}$$

Now we can plug back in that solution into Eq. (3.26) and get an equation for g. By assuming that the constant a, we introduced above, is the same for all vertices, we find that the solution for f is

$$f(z) = N\frac{1}{z}(1-z)^a \exp\left(-\frac{bm^2}{z}\right), \tag{3.31}$$

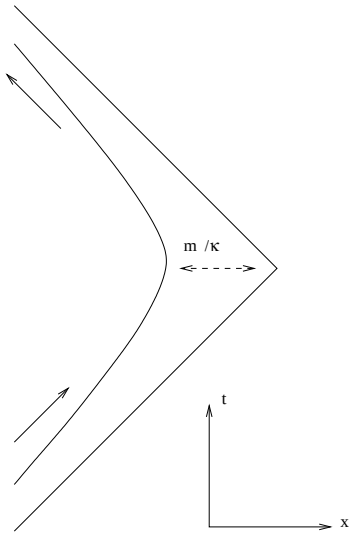

Figure 3.6: The motion in space time of a particle with mass m under a constant force $-\kappa$.

where N is a normalisation constant.
The values for a, b are

$$\begin{aligned} a &= 0.44, \\ b &= 0.37, \end{aligned} \tag{3.32}$$

which were fitted to data.

3.1.2 Massive quarks and baryons

So far we only considered mesons made of massless quarks. Now we will discuss the changes when one assigns masses to the quarks and we also discuss the treatment of baryons.
Massive quarks do not move along rectangles. They move along hyperbolas, which one can easily see by looking at the equation of motions (3.10,3.12).

$$m^2 = E^2 - p^2 = \kappa^2[(x_0 - x)^2 - (t_0 - t)^2]. \tag{3.33}$$

The asymptotes, however, are again the rectangles (cf. Fig. 3.6). We also note that the considerations for the fragmentation were independent of the mass of the particles. In addition we have to account for another physical effect. Due to energy-momentum conservation, a real massive quark-antiquark pair cannot be created at one point of the string. For that reason a virtual pair has to be created first, which then tunnels to a real pair. That effect can be calculated (cf. [GM83]) as follows. We start with a massive quark-antiquark pair which is produced in

the string at time $t = 0$. The longitudinal component of the momentum is given by

$$p_l^2 + p_t^2 + m^2 = 0 \quad \Rightarrow \quad p_l = i\sqrt{p_t^2 + m^2}. \tag{3.34}$$

At time $t > 0$ the virtual particles have moved a distance r apart and ate up the color field in between. So at that time p_l is given by

$$p_l = i\sqrt{p_t^2 + m^2 - (\kappa r)^2}. \tag{3.35}$$

The particles will become real when $p_l(r) = 0$, i.e. when $E_t = \sqrt{p_t^2 + m^2} = \kappa r$. The wave function in the classically forbidden region can be calculated in the WKB approximation. This is a quasiclassical approximation which one obtains by plugging the ansatz $\Psi = e^{\frac{i}{\hbar}\sigma(x)}$ into the Schrödinger equation for one dimension $\frac{\hbar^2}{2m}\Psi'' + (E - U(x))\Psi = 0$, which results in an equation for σ

$$\frac{1}{2m}\sigma'^2 - \frac{i\hbar}{2m}\sigma'' = E - U(x). \tag{3.36}$$

The prime means a derivative with respect to x. If we now expand σ in a power series in $\hbar$

$$\sigma = \sigma_0 + \frac{\hbar}{i}\sigma_1 + \ldots \tag{3.37}$$

and keep only the lowest order term, i.e. we approximate $\sigma = \sigma_0$, we get

$$\frac{1}{2m}\sigma_0'^2 = E - U(x) \tag{3.38}$$

and therefore

$$\sigma_0 = \pm \int \sqrt{2m(E - U(x))}dx, \tag{3.39}$$

which is just the integral over the classical momentum. So in our case we can write our wavefunction for the classical forbidden region in that approximation as

$$\Psi(x) = \Psi_c \exp\left[-i\int_{E_t/\kappa}^{x} p_l(r)dr\right], \tag{3.40}$$

where Ψ_c is the value of the wave function at $x = E_t/\kappa$. We chose the plus sign in the exponential in order to get an exponentially decaying wavefunction in the classical forbidden region. The integral for $x = 0$ can easily be performed and we get

$$R = \frac{\Psi(0)}{\Psi_c} = \exp\left(-\frac{\pi E_t^2}{4\kappa}\right). \tag{3.41}$$

The probability that the virtual pair tunnels to a real one is then given by the overlap of their wavefunctions at the origin

$$|R^2|^2 = \exp\left(-\frac{\pi E_t^2}{\kappa}\right). \tag{3.42}$$

The 4th power reflects the fact that both, the quark and the antiquark, have to tunnel to real particles. The production of s-quarks is therefore suppressed in comparison to the lighter u- and d-quarks.
The production of baryons is realised by the creation of diquark-antidiquark pairs. The diquarks are treated like quarks with a higher mass. Thus a baryon is a yoyo hadron made out of a quark and a diquark.
In the technical realisation the masses of the quarks and the diquarks are translated into suppression factors. The values for the suppression factors are

$$\begin{aligned}
\frac{P(uu)}{P(u)} &= 0.07 \\
\frac{P(s)}{P(u)} &= \begin{cases} 0.3 & \text{for} \quad \sqrt{s} \geq 20\text{GeV} \\ 0.4 & \text{for} \quad \sqrt{s} \leq 5\text{GeV} \\ \frac{11}{30} - \frac{1}{150}\sqrt{s}[\text{GeV}]^{-1} & \text{for} \quad 5\text{GeV} < \sqrt{s} < 20\text{GeV} \end{cases} \\
\frac{P(su)}{P(uu)} &= 0.4
\end{aligned} \tag{3.43}$$

Those parameters are taken from [Gei98]. The energy dependence of the strangeness suppression factor $\gamma = P(s)/P(u)$ was introduced in order to get a good agreement with experimental data on strangeness production in pp collisions. A comparison to data is shown in Section 3.1.5.
The particles which are implemented in our string model are

$$\pi, \eta, K, K^*, \rho, \omega, \phi, \eta'$$

and

$$p, n, \Delta, \Lambda, \Sigma, \Sigma^*.$$

We did not list the charmed particles because they are not produced at our energy regime due to their high suppression factors.

3.1.3 Annihilation processes

The Fritiof model is only capable to produce two excited hadrons, which fragment separately. Thus it is not possible to describe processes in which a quark from, for example, an incoming baryon and an antiquark from an incoming meson annihilate (cf. Fig. 3.7). An example for such a process is

$$\pi N \to YK, \tag{3.44}$$

where Y stands for a hyperon.
Due to that reason we underestimate the strangeness production in the region just above our threshold ($\sqrt{s} > 2$ GeV) because there the easiest way to produce a strange particle is through the annihilation processes, which we completely

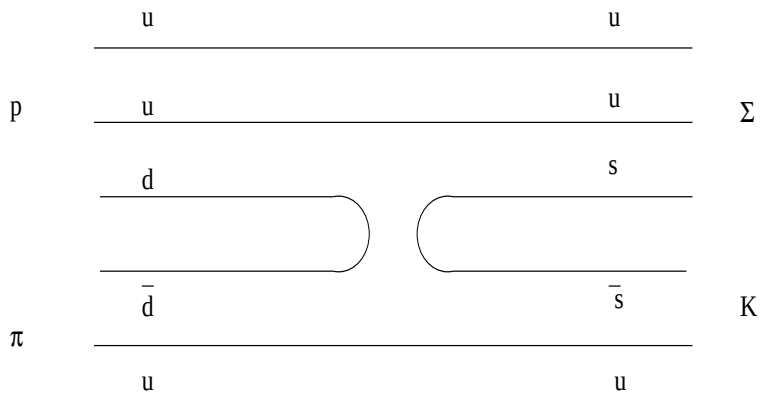

Figure 3.7: Quark Diagram for the process $\pi^+ p \to \Sigma^+ K^+$.

miss.
For that reason we included the annihilation by hand. In case of a reaction of a baryon with a meson we check if an annihilation between a quark and an antiquark is possible. This means that we split the hadron in its constituents and check whether a quark and antiquark with the same flavour exists. If it is possible we will choose according to the probability in Eq. (3.45) whether the Fritiof model is called or an annihilation takes place. In the latter case we put the remaining quarks (the quark content of the baryon and the meson **without** the antiquark and the quark with the same flavour as the antiquark) in **one** string which has the energy and momentum of both particles. Then the fragmentation is done according to the Lund Model. This is, of course, only a model description. In case the two quarks are annihilating, at least a gluon would have been emitted from the annihilation process. However, if one interprets that kind of processes as a meson and a baryon annihilating into a short living resonance which immediately decays, then we would have again only one object, which has to decay. Since the decay properties are unknown one simulates the decay by a string model. This is the way UrQMD interprets those reactions [Web02].
The probability for the annihilation is chosen such that we agree on the strangeness production in $\pi p \to$ strange particles (see Fig. 3.8). We see that directly above the threshold for string production the cross section with the old description descends to almost zero for the reasons we just mentioned. The data is taken from [BFMM88] and it is not obvious how to count that cross section. In our calculation we decided to have a 'strange particle' event, if at least one strange particle has been in the final state. In case of several strange particles we nevertheless count the event only once. The strange particles have been in our case the $\Lambda, \Sigma, \Xi, \Omega$ and all kaons. Due to these uncertainties we also compared exclusive channels to data from [BFMM88], where no question about the final state arises. Some of the comparisons are shown in Fig. 3.9. We see in all channels an improvement by implementing the annihilation processes, even though we do not

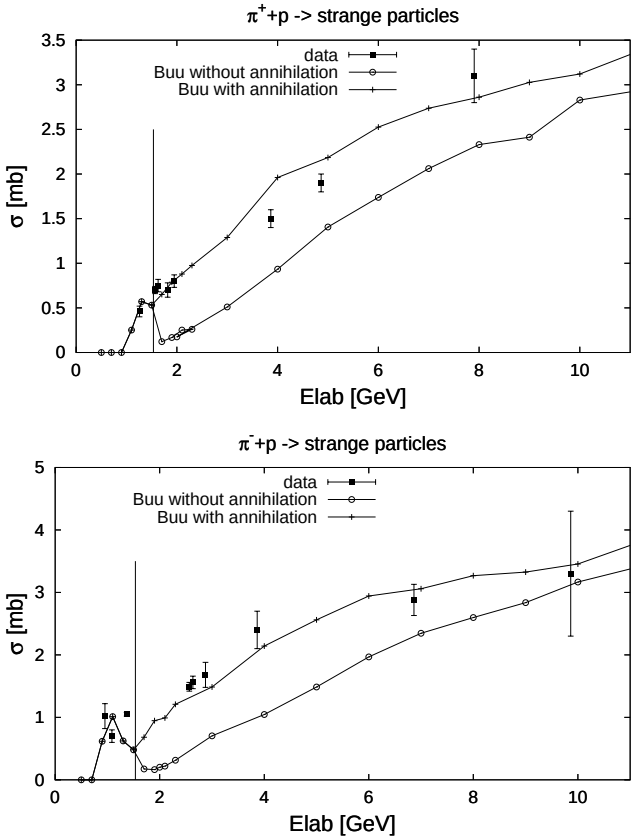

Figure 3.8: Strangeness production in πp in comparison to data from [BFMM88]. The vertical line corresponds to the threshold for the string model ($\sqrt{s} = 2$ GeV).

hit the data exactly in all reactions. The agreement at low laboratory momentum is of course due to the threshold for string production. Above the threshold the cross sections without the annihilation processes are falling down to zero as expected.

$$\text{Prob(annihilation)} = \max(0.85 - 0.17 \cdot \frac{\sqrt{s}}{\text{GeV}}, 0). \tag{3.45}$$

In some of the calculations, which will be presented later, we used a different strangeness suppression factor, namely $\gamma = 0.3$. In that case we have to readjust the probability for the annihilation processes

$$\text{Prob(annihilation)}_{\gamma=0.3} = \max(1.2 - 0.2 \cdot \frac{\sqrt{s}}{\text{GeV}}, 0). \tag{3.46}$$

There are two main reasons for the increase of the strange particle production by including the annihilation. The first one is that we completely miss some

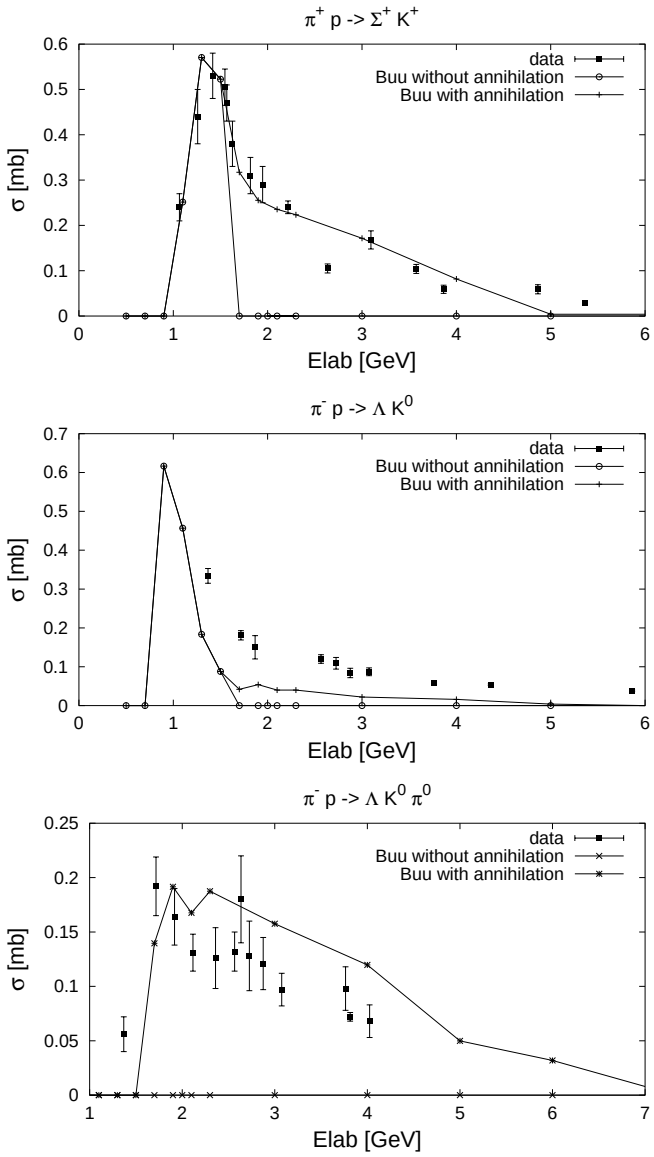

Figure 3.9: Exclusive cross sections for strangeness production in πp in comparison to data from [BFMM88].

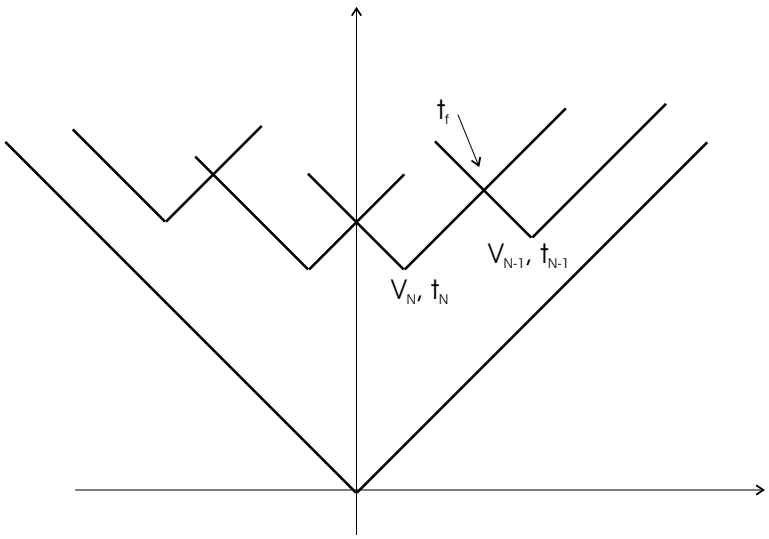

Figure 3.10: Decay of a string. t_f is the time, at which the quarks from the adjacent vertices meet first.

channels, which we already explained before. Another point is that the invariant energy per string decay is higher. If we have two strings instead of one, the two strings decay separately and therefore it will often occur that every string alone is below the threshold for strangeness production but if one puts the whole invariant energy into one string the string might decay into strange particles. By putting all the energy into one string, the invariant energy becomes higher and the production of strangeness more probable.

3.1.4 The Formation time

The application of a string model in a hadronic transport model raises the question of the formation time of the hadrons, which are formed in the string. The formation time is the time the constituent quarks of the respective hadron need in order to bind together and to form the hadron. One question which arises is, which is the point to define as formation point. One could for example use the string break-up points or the point where the quark trajectories of a yoyo state meet for the first time (cf. Fig. 3.10). If one defines one of those points as the formation point, one can in general calculate the formation time. We decided to let that question open and to use an effective formation time of

$$\tau_f = 0.8\,\mathrm{fm/c}. \tag{3.47}$$

This is a reasonable time since in this time a quark-antiquark pair can separate far enough to reach a distance which is of the order of the size of a hadron. Other

transport models as HSD and UrQMD use a similar value for the formation time, which will be discussed in Chapter 5. The formation time is defined in the rest frame of the particle and so one has to multiply with the γ-factor of the particle in the current system.
The next question which arises is, how to treat the hadrons, which are build out of at least one quark, which have been there from the beginning. Those hadrons are called the leading hadrons. It would be unreasonable to treat them in the same way as the newly produced particles because part of their constituents have always been there. On the other hand they also have to form and so it would be wrong to treat them as ordinary hadrons. We decided to parametrize our ignorance by reducing the cross sections of the leading hadrons during the formation time by a certain factor. It turned out that the data is best described, if we choose that factor to be $\frac{1}{3}$.

$$\sigma(\text{lead.hadron-hadron}) = \frac{1}{3}\sigma(\text{hadron-hadron}) \tag{3.48}$$

The comparison to data in photoproduction processes was done in [Fal]. After their formation time, all particles from the string decay react like ordinary particles.
We will raise the question of the formation time once more in Section 6.3 when we talk about string-string collisions and the lifetime of a string.

3.1.5 Comparison to data

In this section we want to compare the elementary processes with the data, available at the energies of interest. This means basically that we will show the particle spectra and particle multiplicities which are produced by our string model.

pp Collisions

The only baryon-baryon channel which offers enough data at our energies to compare with, is the *pp* channel. In Fig. 3.11 we show the inclusive π and K production cross sections as a function of kinetic energy. The data for the pions are taken from [A$^+$73, BFMM88] and the data for the kaons is a sample from [GR96, BFMM88]. We see that we describe pions relatively well, although we slightly overestimate π^+ at energies below 10 GeV and underestimate them at energies above 10 GeV. For the kaons we show two model calculations. One is the calculation with the energy dependent suppression factor, as it was explained in Section 3.1.2, and the other one is a calculation with a reduced suppression factor $\gamma = 0.3$. At energies below approximately 10 GeV we overestimate kaons in both cases, whereas the situation looks better with the reduced suppression factor. Above 10 GeV the error bars become very big and it is hard to make a precise

statement. We have to keep that in mind when we look at heavy-ion collisions. For K^- production the situation is similar. At energies below approximately 15 GeV we seem to overestimate K^- production, whereas at the higher energies it is again hard to make a statement due to the big error bars.
Next we will investigate rapidity and p_t distributions. We use the data from an old experiment done by Blobel et al. in 1973 [B+73]. They measured the inclusive production of $\pi^{\pm}, K^0_S, p, \Lambda, \Sigma^{\pm}$ and $\overline{\Lambda}$ at an incident beam momentum of 12 GeV/c, which corresponds to a kinetic energy of 11.1 GeV. In Fig. 3.12 we see the differential cross section for proton production together with the experimental data. In the determination of the cross section only inelastic events were taken into account. We overestimate the data around midrapidity which means that the stopping is too high.
Figure 3.13 shows the differential cross section for π production. The dashed line corresponds to the reduced suppression factor $\gamma = 0.3$. We see that the difference in the pion production is quite small and the pion yields increase only little. Therefore we will show in the following only the influence of the reduced suppression factor on strange particles. We underestimate the data around midrapidity for π^+, as well as for π^-. By looking at the proton rapidity spectra, which produced too much stopping, this result is unexpected. Since the stopping is too high, we would expect the pions to be overestimated. We have to remember that fact, when we discuss pion yields in heavy-ion collision. Next we look at p_t-spectra, which are shown in Fig. 3.14. The differential cross section is plotted as a function of the transverse momentum squared. We see that the slopes agree very well, whereas the multiplicity of the K^0_S is too high. This overestimation of strangeness was already seen when we looked at the K^+ and K^- yields as a function of energy. So we seem to produce too much strangeness in pp collisions. The situation improves slightly by employing the lower suppression factor, but the spectrum is still overestimated. We determined the K^0_S by

$$K^0_S = \frac{1}{2}(K^0 + \overline{K}^0). \tag{3.49}$$

3.1.6 πN Collisions

For the baryon-meson channel we do not have much data to compare with. Therefore we compare with other models, namely HSD [CB99] and UrQMD [Web02]. We will mention the differences and general ingredients of those transport models in Chapter 5, when we show the excitation functions for heavy-ion collisions. Here we only want to note that both codes use quite comparable string models. In Fig. 3.15 we see in the upper two graphs the π^+ rapidity distributions at a kinetic energy for the pion of 2 GeV and 4 GeV. The results show differences, but they are not very pronounced. The lower two graphs show the rapidity distributions for K^+ at an incident energy of again 2 GeV and 4 GeV. Here the

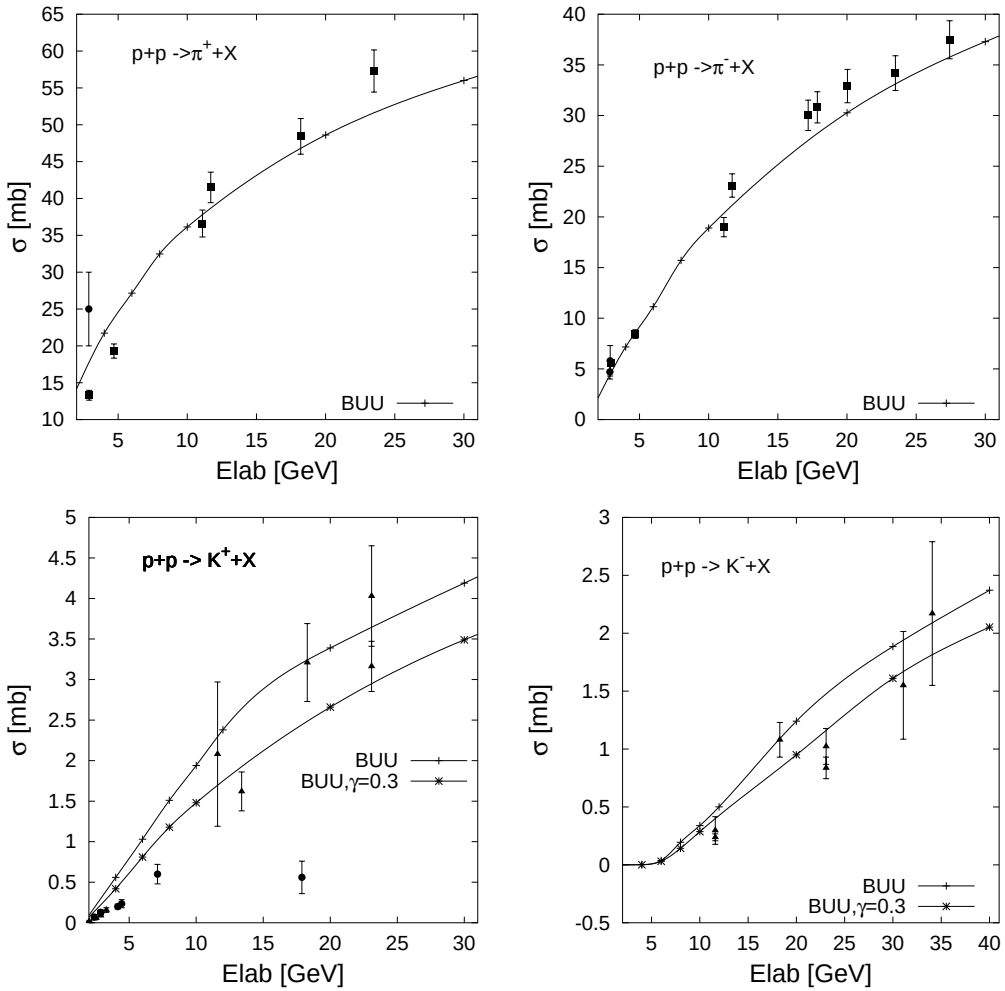

Figure 3.11: Inclusive cross section for π and K production in comparison with data from [A$^+$73](full squares), [GR96](full triangles) and [BFMM88](full circles) as a function of kinetic energy.

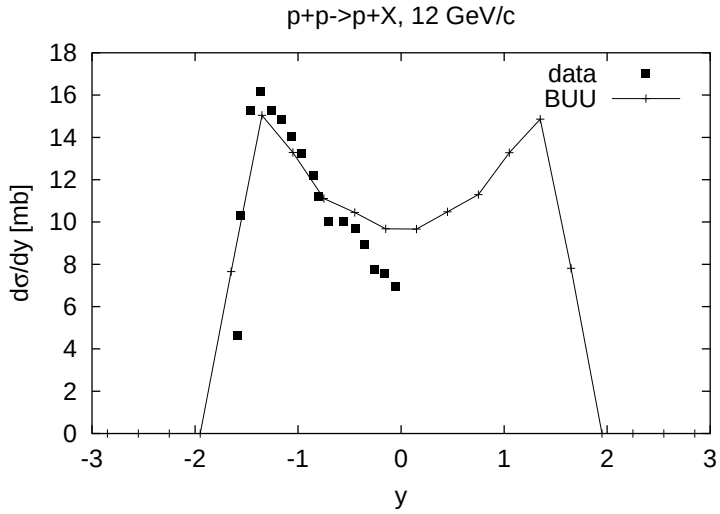

Figure 3.12: Inclusive differential cross section for p production in pp collisions at an incident momentum of 12 GeV/c in comparison with data from [B$^+$73]. Only processes with at least three particles in the final state have been taken into account.

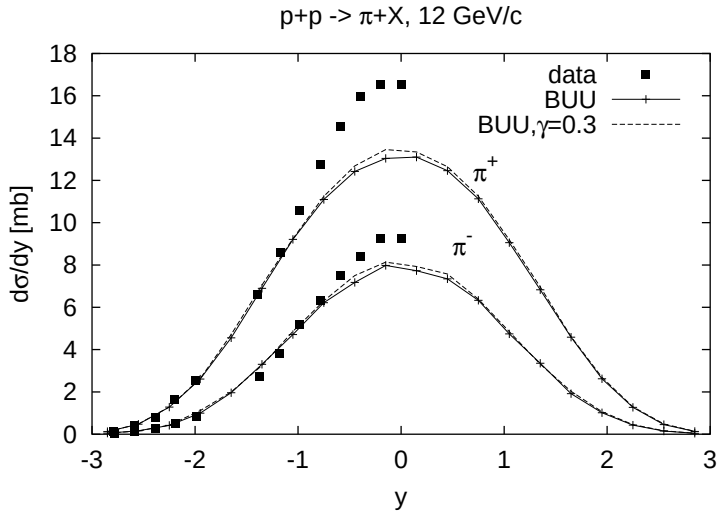

Figure 3.13: Inclusive differential cross section for π production, calculated with two different suppression factors, in pp collisions at an incident momentum of 12 GeV/c in comparison with data from [B$^+$73].

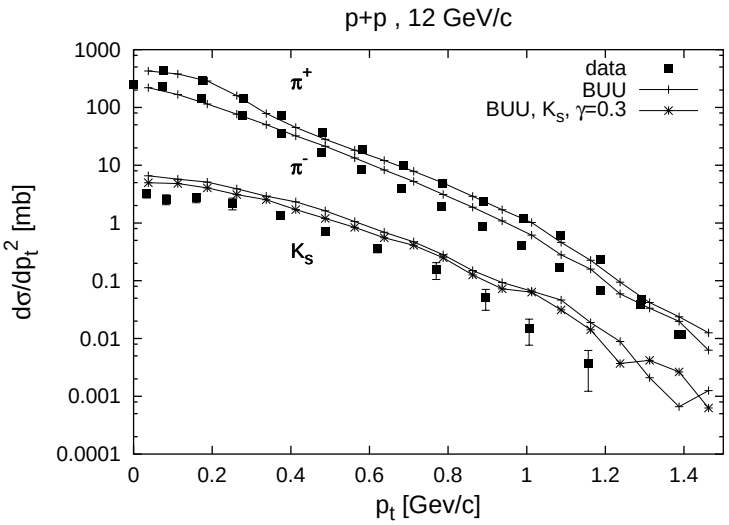

Figure 3.14: Differential cross section for π^+, π^- and K_S^0 production in pp collisions at an incident momentum of 12 GeV/c as a function of p_t in comparison with data from [B+73].

differences are big. Whereas at 2 GeV the UrQMD model produces less kaons by a factor of about 5 in comparison to HSD and our model, the situation changes drastically at 4 GeV. Here UrQMD produces twice as many kaons as HSD and our model gives results in between. The angular distribution also seems to be different, since the shape of the spectra is quite different. That difference is again more pronounced in the kaon spectra. Those uncertainties are surely a problem and it would be worthwhile to spend some effort on that issue in order to get more reliable models to simulate those collisions.

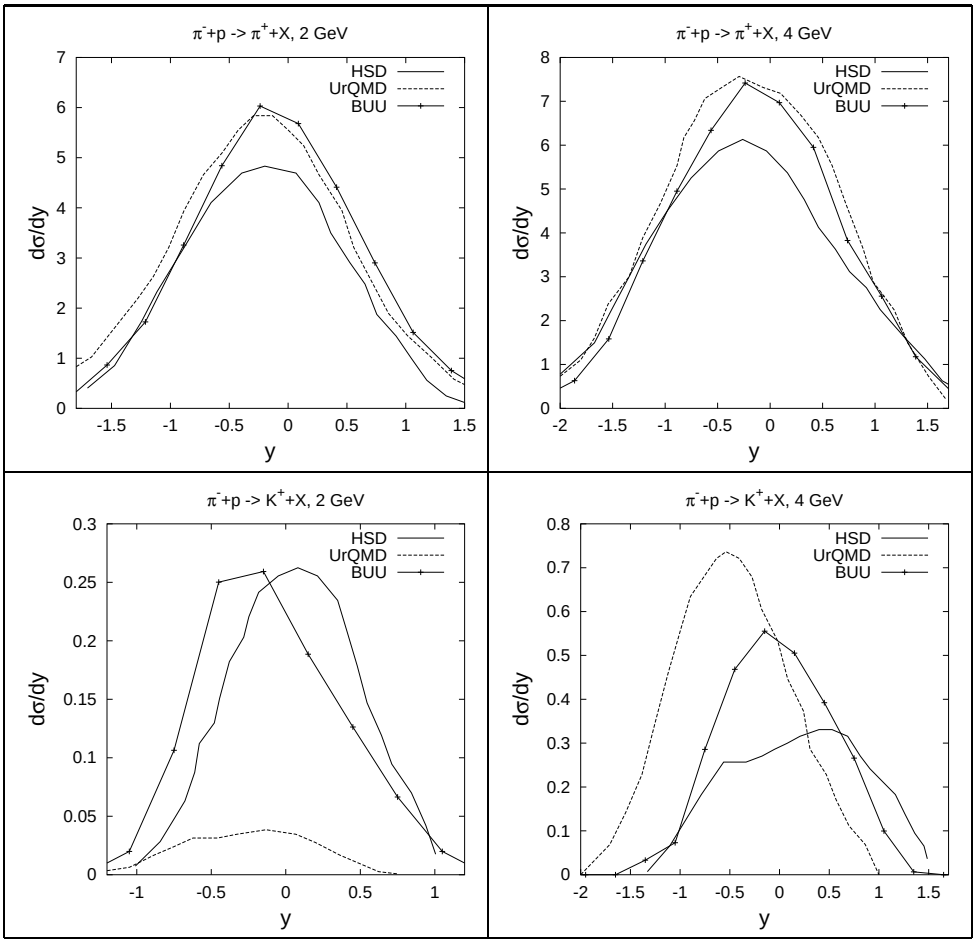

Figure 3.15: Differential production cross section for π^+ and K^+ in $\pi^- p$ collisions at 2 GeV and 4 GeV in comparison to HSD and UrQMD [WBCS03].

Chapter 4

From proton induced reactions to heavy-ion collisions

In order to clarify the reaction mechanism in heavy-ion collisions, it is necessary to understand the systematics of the underlying processes. As we increase the system size, we can study, for example, the effect of secondary collisions or check some otherwise experimentally not accessible cross sections, which will be explained in more detail in the next section. By increasing the system size we increase the density of the system. Thus we can also see how particle spectra evolve with increasing density and if our model within the standard parameters is able to reproduce the experimental measurements. That would be a sign for the correct implementation of the reaction dynamics.

4.1 Proton induced Reactions

We are going to compare our model to data, which was published by the E-802 collaboration at the AGS [Abb92]. The collaboration measured π, K and p m_t-spectra at an incident momentum of 14.6 GeV/c in proton induced reactions with Be, Al, Cu and Au targets. We will compare our model to the data on p+Be and p+Au. The spectra were fitted with an exponential function

$$\frac{d^2\sigma}{2\pi m_t dm_t dy} = Ae^{-m_t/T}. \tag{4.1}$$

The rapidity distributions are obtained as follows

$$\frac{d\sigma}{dy} = \int_{m_0}^{\infty}\int_{0}^{2\pi}\left(\frac{d^2\sigma}{2\pi m_t dm_t dy}\right) m_t dm_t d\phi = 2A\pi T^2(1+m_0/T)e^{-m_0/T}. \tag{4.2}$$

So we only need the parameters A and T from the fit to the m_t spectra in the respective rapidity interval. In our calculations we determined the rapidities in two different ways. First we calculated the spectra in the same way as the

experimentalists, which means that we determined the m_t spectra for one rapidity interval and calculated the rapidity in that interval through the fit parameters by using Eq. (4.2). In order to get a rapidity distribution, one has to repeat that procedure for the other intervals. Second we calculated them directly. If at low p_t the spectra had shown a flattening, there would have been a difference. Since we could not see a significant difference, we present the direct calculations.
In order to compare the particle production in each collision for various targets, the rapidity spectra were normalized to the inelastic cross section

$$\frac{dn}{dy} = \frac{1}{\sigma_{\text{inel}}} \frac{d\sigma}{dy}. \tag{4.3}$$

The values for σ_{inel} are

$$\sigma_{\text{inel}}(p + \text{Be}) = 208 \text{ mb}, \tag{4.4}$$
$$\sigma_{\text{inel}}(p + \text{Au}) = 1790 \text{ mb}. \tag{4.5}$$

which was measured by [DDG+73].
We start out by looking at the inverse slope parameters T and the rapidity spectra in p+Be reactions. Since the radius of Be is only about 2.5 fm, we do not expect an influence of the secondary collisions. A pion with $p = 1$ GeV/c for example has a γ-factor of about 7 and so the formation time is $\tau_f \approx 5.6$ fm/c. Therefore the pion will form outside the nucleus and will not react with other particles. That means that the process is a good test for the isospin averaged cross sections for $p + N$-reactions. In Fig. 4.1 we see the rapidity spectrum for protons. As in the pp collisions (cf. Fig. 3.12) we see that our model produces too much stopping because the calculated yields at midrapidity are too high. However, the spectrum has to be compared with some caution. The rise of the measured spectrum at rapidities above 2 might be due to a misidentification of particles. Positive charged kaons with a momentum between 3.5 GeV/c and 5.6 GeV/c are for example identified as protons. By taking this fact into account in our calculations, we also get a little increase at rapidities above 2 but it is not as pronounced as in the data. However, if we also count other positive charged particles with momenta above 3.5 GeV/c as protons we get the same increase. In the calculation which is shown in Fig. 4.1 protons were counted in the usual way.
The rapidity spectra of kaons and pions show the same behaviour as the spectra for pp collisions, namely we overestimate the kaons and we underestimate the pions (see Fig. 4.2). The deviations in the K^+ spectra are not very pronounced and with the suppression factor $\gamma = 0.3$ we even underestimate kaons. The K^- are overestimated with both suppression factors, whereas the lower suppression factor seems to be favored. In Fig. 4.3 we show the inverse slope parameters for K^+ and π^+. The pion slopes are well described, except at the larger and lower rapidities, where we overestimate the data. The K^+ slopes are overpredicted by

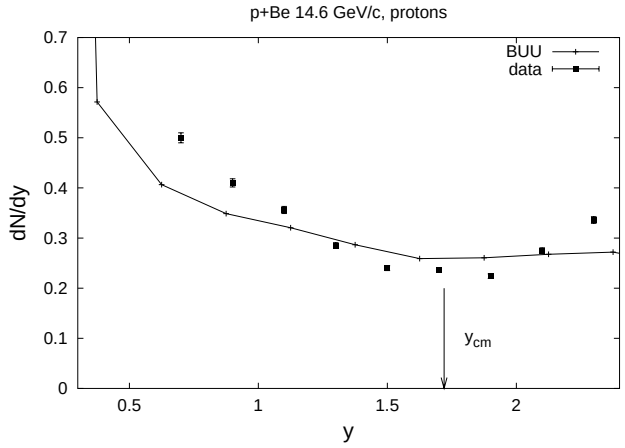

Figure 4.1: Rapidity distribution of protons for p+Be at 14.6 GeV/c in comparison to data from [Abb92]. The arrow indicates the nucleon-nucleon midrapidity.

about 20% at midrapidity. This might be compared to the slopes in pp collisions in Fig. 3.14. However, in Fig. 3.14 we only see the K_S slope integrated over the whole rapidity and unfortunately we did not find data on K^+ slopes as a function of rapidity in elementary reactions. The overestimation of the slopes should be kept in mind, as it will be important when we investigate the excitation function for the K^+ slopes in heavy ion collisions. There our model will underestimate the slopes, which we will see in Chapter 5.
Now we increase the target mass and investigate p+Au reactions. Whereas in p+Be we underestimated pions and overestimated the K production, we now agree on the K^+ production and agree well on the π production, too (see Fig. 4.5). We have to keep that development in mind while we further increase the system size. We also see that in the K^+ spectrum $\gamma = 0.3$ does not seem to be favored anymore, whereas the K^- spectra still favors the lower suppression factor. For K^+ we also show the calculation without the annihilation processes in order to show their influence on K^+ production. In Fig. 4.6 we see the inverse slope parameters as a function of rapidity for π^+ and K^+. For pions we see that the results of our calculations are still too high at larger rapidities. The kaons slopes seem to be described pretty well and we do not overestimate them at midrapidity anymore. The proton spectra in Fig. 4.5 are also in line with data. So we cannot see any significant deviations to data in p+Au at 14.6 GeV/c.

4.2 Si+Au

Now we want to increase the system size one step further and look at Si+Au reactions. The data were again taken by the E-802 collaboration [A$^+$94] at 14.6

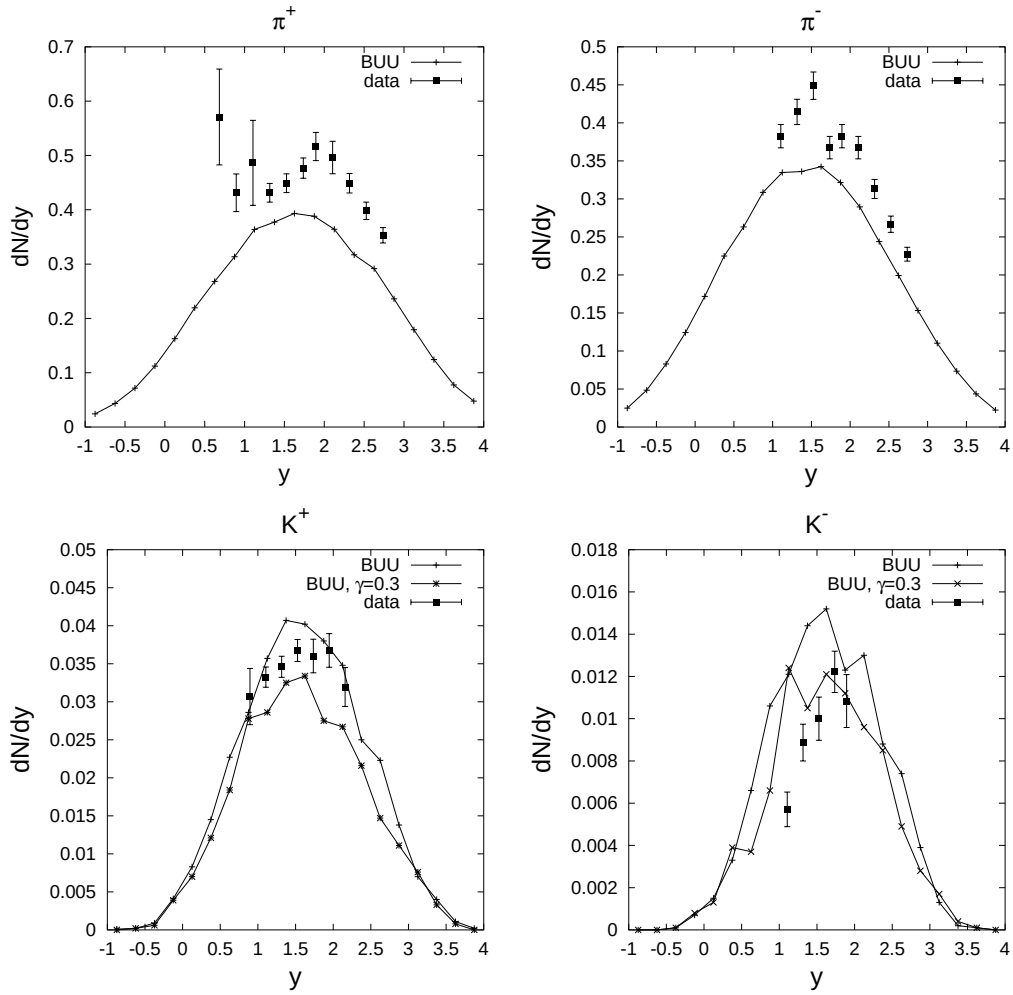

Figure 4.2: Rapidity distributions of π and K for p+Be at 14.6 GeV/c in comparison to data from [Abb92].

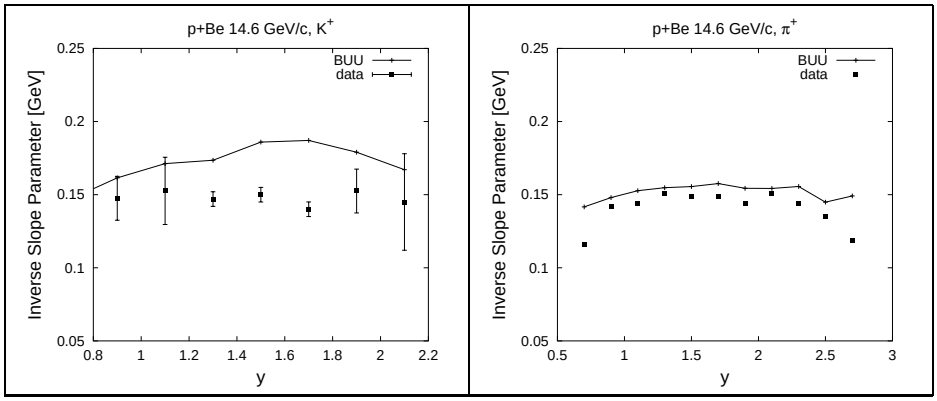

Figure 4.3: Rapidity distributions of inverse slope parameters for π^+ and K^+ for p+Be at 14.6 GeV/c in comparison to data from [Abb92].

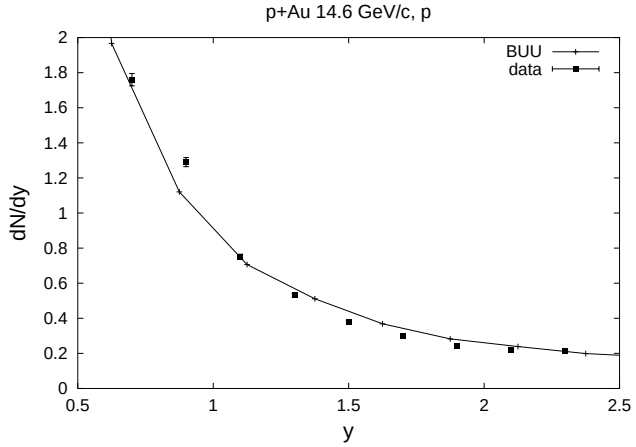

Figure 4.4: Rapidity distribution of protons for p+Au at 14.6 GeV/c in comparison to data from [Abb92].

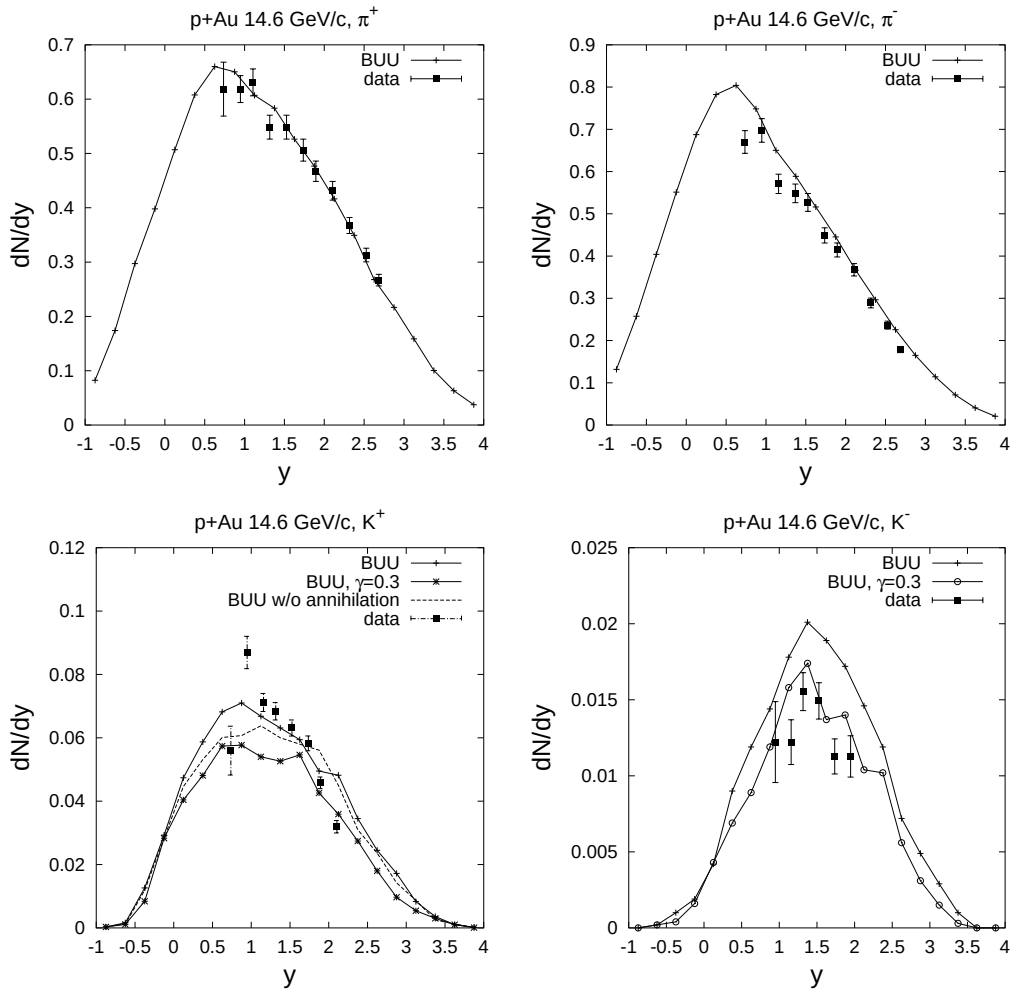

Figure 4.5: Rapidity distributions of π and K for p+Au at 14.6 GeV/c in comparison to data from [Abb92].

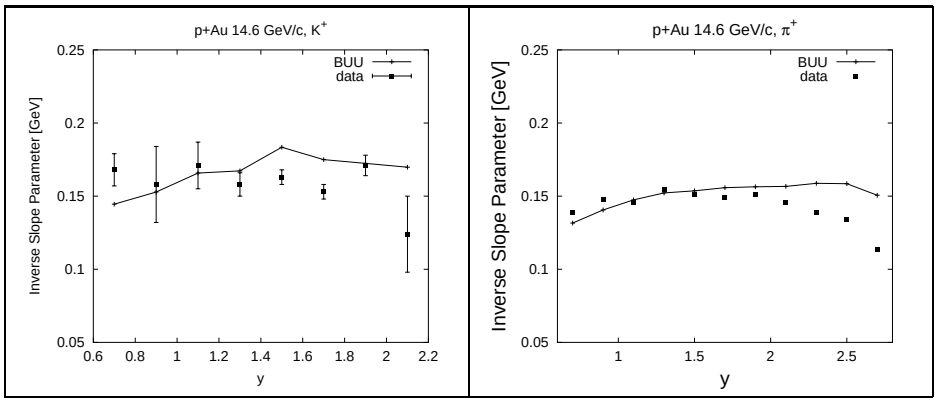

Figure 4.6: Rapidity distributions of inverse slope parameters for π^+ and K^+ for p+Au at 14.6 GeV/c in comparison to data from [Abb92].

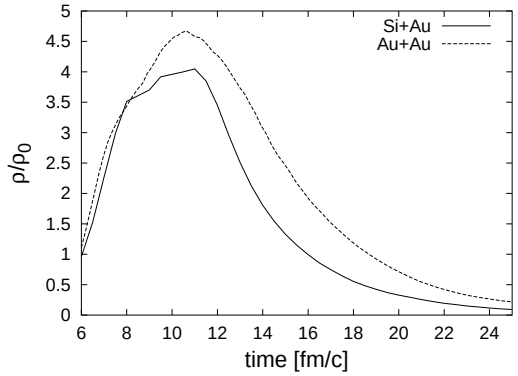

Figure 4.7: Baryon density in the central region in Au+Au at 11.6 GeV/c and Si+Au at 14.6 GeV/c as function of time.

GeV/c in order to be able to compare directly to the proton induced reactions. In Fig. 4.7 we see the baryon density in Au+Au at 11.6 GeV/c and Si+Au at 14.6 GeV/c as a function of time. The density was calculated as $\rho = \sqrt{j^\mu j_\mu}$ in the central region of the collision. In addition to the baryons, we also counted the baryonic strings with a weight which is equal to the factor by which the cross section is reduced (see Section 3.1.4). We see that in Si+Au we already reach high baryon densities, which are compatible to Au+Au collisions. In Fig. 4.2 a contour plot of the density profiles of the collisions is shown. We plotted the density as function of the x-coordinate and z-coordinate at y=0. We see that the high density region in Si+Au is much smaller than in Au+Au.
The events were characterized by the multiplicity of charged hadrons and central collisions were defined to be the upper 7% of the so characterized events. We will discuss the centrality selection in more detail in Section 4.3.1.

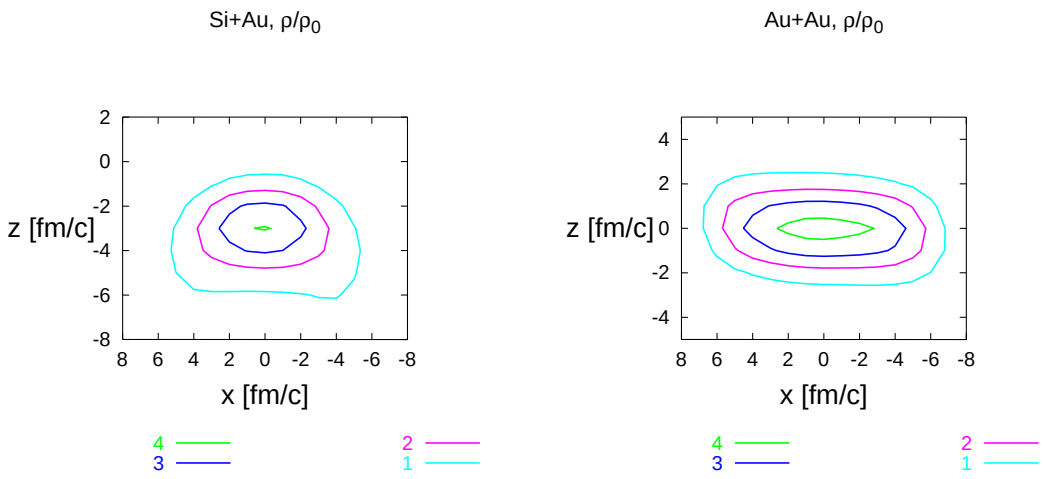

Figure 4.8: Contour Plots of the baryon density profile in Si+Au at 14.6 GeV/c and Au+Au at 11.6 GeV/c in units of ρ_0.

We see in Fig. 4.2 that the development of the π production continues in the same manner. In other words, the pions continue to increase in comparison to experiment and we are not agreeing anymore with the experimental yields. We see that the discrepancy is already quite pronounced in Si+Au collisions. This is a problem which we will also encounter in heavy-ion collisions at these energies and which is still an open problem. Since the behaviour of the spectra in the elementary reactions is the opposite, the reason seems to be in the secondary collisions. The K^+ rapidity distribution, however, is very well in line with experiment. This indicates that the implementation of the secondary collisions for K^+ is reasonable. However the overshooting in the K^- rapidity distribution might also indicate that the meson-meson cross sections are too high because this is one of the most important channels for K^- production as the number of mesons increase, which is the case in Si+Au. The most important of those channels is $\pi\rho \rightarrow K\overline{K}$, followed by $\pi\omega \rightarrow K\overline{K}$. In those channels the production of $K\overline{K}$ is p-wave suppressed and the threshold for $K\overline{K}^*$ and $K^*\overline{K}$ is of course higher. Since we had so much freedom in choosing the cross sections, we did not take this into account so far. In the future it should be investigated, how these modifications influence the kaon yields in Si+Au and in heavy-ion collisions. As in p+Au the K^- spectra suggest a strangeness suppression factor γ=0.3, whereas the K^+ spectra favors the old suppression factor. The slopes also show first serious disagreement with data. For both π^+ and K^+ the slopes of our calculations are not hard enough, which means that we seem to miss pressure in our system.

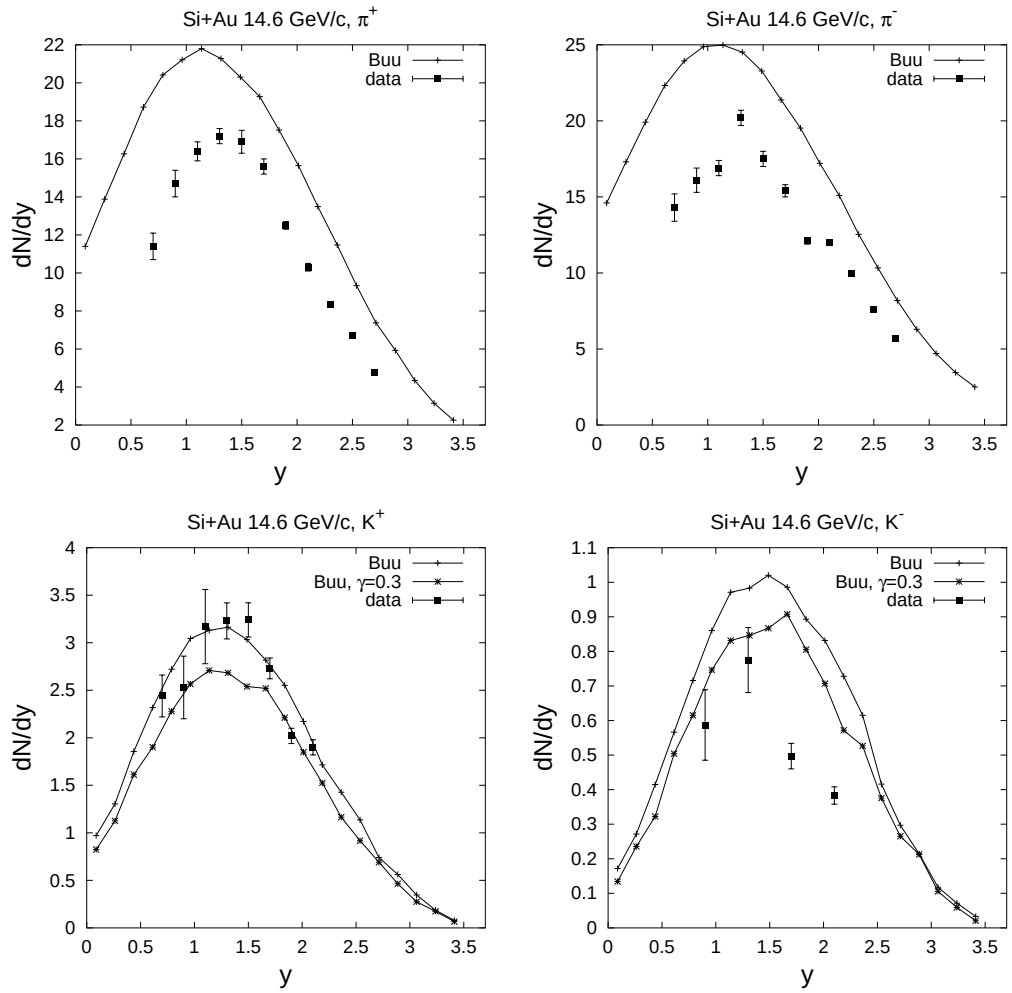

Figure 4.9: Rapidity distributions of π and K for Si+Au at 14.6 GeV/c in comparison to data from [A+94].

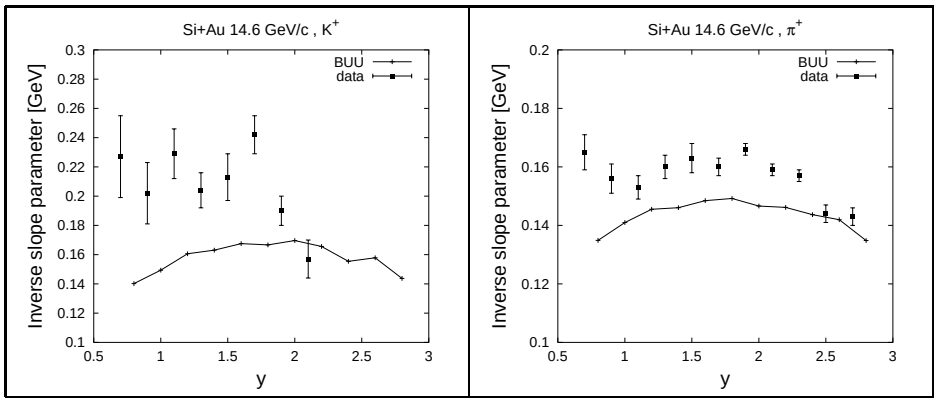

Figure 4.10: Inverse slope parameter as function of rapidity for π^+ and K^+ in Si+Au at 14.6 GeV/c in comparison to data from [A+94].

4.3 Heavy-Ion Collisions

Now we want to investigate heavy-ion collisions. In order to compare the development to the preceding chapters, we choose Au+Au collisions at 10.7 A·GeV. This energy is close to the energy region we just discussed and there is a lot of data at that energy. The experiment we are looking at used two different methods to determine centrality, which will be explained in the next section. This gives us the possibility to study the influence of centrality selection criteria. By studying the particle production as a function of centrality, we also have again the possibility to look at particle spectra with increasing system size.

4.3.1 Centrality selection

The impact parameter is experimentally not accessible and so one has to come up with an idea of how to characterize a collision. Two quantities, which are used frequently, are the energy measured near zero degrees and the total event multiplicity. The connection to the impact parameter is as follows. In case of a characterization of collisions by the total multiplicity N, which is the number of particles which hit a detector with a certain geometry, we can build the quantity $d\sigma/dN$. Now we can define another quantity

$$\sigma_N \equiv \int_{N_{\rm cut}}^{N_{\rm max}} \frac{d\sigma}{dN} dN, \tag{4.6}$$

where $N_{\rm cut}$ is the multiplicity cut which has to be chosen according to the desired centrality selection and $N_{\rm max}$ corresponds to the most central collision, which was detected. The most central 5% are, for example, determined by demanding that $\sigma_N/\sigma_{\rm inel} = 0.05$, which can be fulfilled with the right choice of $N_{\rm cut}$. Once we interpret σ_N as an area we can calculate the impact parameter. The zero degree

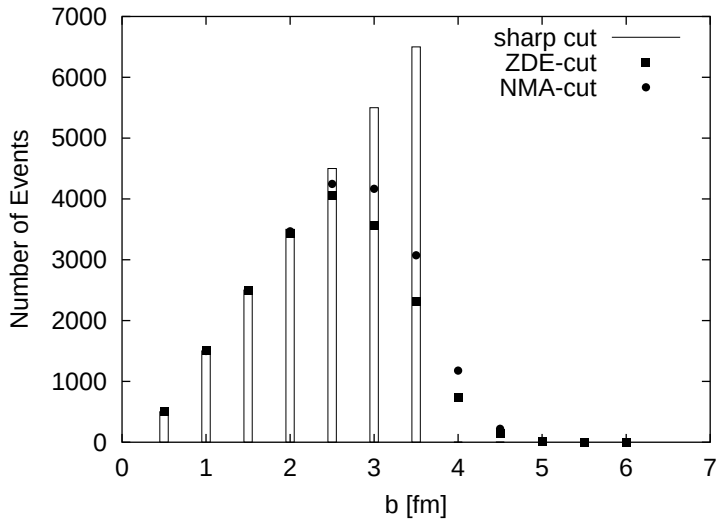

Figure 4.11: The number of collisions as a function of the impact parameter for three different centrality selections. 'ZDE' corresponds to a definition of centrality through the zero degree energy, 'NMA' corresponds to the definition by the multiplicity and 'sharp cut' stands for sharp cut off in the impact parameter in the theoretical simulation (see text).

energy method works the same way, except that we build the quantity $d\sigma/dZ$ instead of $d\sigma/dN$. Z is the energy of the nucleons, which did not collide and which therefore fly straight through the collision zone and can be detected at a low angle far behind the detector. If a collision satisfies one of the criteria it is called an event and the result contributes to the analysis.
Now we want to check which collisions we take into account by applying the different criteria for the centrality selection. In Fig. 4.11 we show the collisions contributing to the different criteria sorted according to their impact parameter. The first criterion which is labeled 'sharp cut' in the figure means that we only take into account collisions with an impact parameter lower than 3.5 fm. Due to the geometry larger impact parameters contribute more frequently according to the formula $dN \sim b\,db$. The squares and the circles correspond to the criteria, we just described. One sees that due to the statistical nature of those collisions, different events are contributing in the analysis depending on the centrality selection. Whereas the difference between the selection by the zero degree energy and the total event multiplicity is pretty small, the sharp cutoff seems to select different events. However, if one compares the particle spectra one cannot make out a difference. In Tab. 4.1 we listed the midrapidity yields of π^+ and K^+ for the three different criteria. Due to this agreement we decided to choose a sharp cut off for the calculation of the excitation functions in Chapter 5 in order to save computational time.

criterion	dN/dy_{K^+}(mid)	dN/dy_{π^+}(mid)	K^+/π^+(mid)
sharp	22.51	138.2	0.163
ZDE	23.0	141.1	0.163
NMA	22.88	141.4	0.162

Table 4.1: Midrapidity yields of K^+ and π^+ for different centrality selections. 'ZDE' corresponds to a definition of centrality through the zero degree energy, 'NMA' corresponds to the definition by the multiplicity and 'sharp cut' stands for sharp cut off in the impact parameter in the theoretical simulation (see text).

E_{ZCAL} class	E_{ZCAL} range [GeV]	$\%\sigma_{\mathrm{inel}}$	$\langle N_{pp} \rangle$
1	0-240	0-3	181
2	240-390	3-7	168
3	390-570	7-12	152
4	570-780	12-17	134
5	780-1020	17-24	113
6	1020-1290	24-32	89.5
7	1290-1590	32-43	62.5
8	> 1590	43-76	26.9

Table 4.2: Borders for E_{ZCAL}. The percentage of the inelastic cross-section (6.8 mb) to which the class corresponds is also listed.

4.3.2 Particle yields at 10.7 A·GeV/c

In this section we will compare our model to data taken by [A+99]. In that paper Au+Au collisions were characterized by two global observables simultaneously : the energy near zero degrees E_{ZCAL} and the total multiplicity. Particle spectra were measured for different event classes, which were defined according to Tab. 4.2 and Tab. 4.3 ,where N_{pp} is the number of projectile participants, which is estimated by the following formula

$$N_{pp} = 197 \left(1 - \frac{E_{\mathrm{ZCAL}}}{E_{\mathrm{beam}}^{\mathrm{kin}}} \right) \tag{4.7}$$

and $E_{\mathrm{beam}}^{\mathrm{kin}}$=2123 GeV is the kinetic energy of the beam. In the proton spectra in Fig. 4.12 we see that our model produces too much stopping, as we already observed in the elementary reactions. In heavy-ion collision this discrepancy might also be due to the lack of a potential. In a potential the protons will store some energy in the field, which they will get back after leaving the high density phase and so they will not loose that much energy. Another effect will be that we have less energy available for particle production, which would be a problem for

E_{ZCAL} range	$\mathrm{mult}_{\mathrm{NMA}}$ range	E_{ZCAL}	$\mathrm{mult}_{\mathrm{NMA}}$	Average $\mathrm{mult}_{\mathrm{NMA}}$
0-240	> 375	1	1	394.7
0-240	345-375	1	2	360.5
0-240	< 345	1	3	323.2
240-390	> 340	2	1	363.5
240-390	305-340	2	2	322.5
240-390	< 305	2	3	281.0
390-570	> 295	3	1	319.0
390-570	265-295	3	2	280.1
390-570	< 265	3	3	240.7

Table 4.3: Borders for the double event selection.

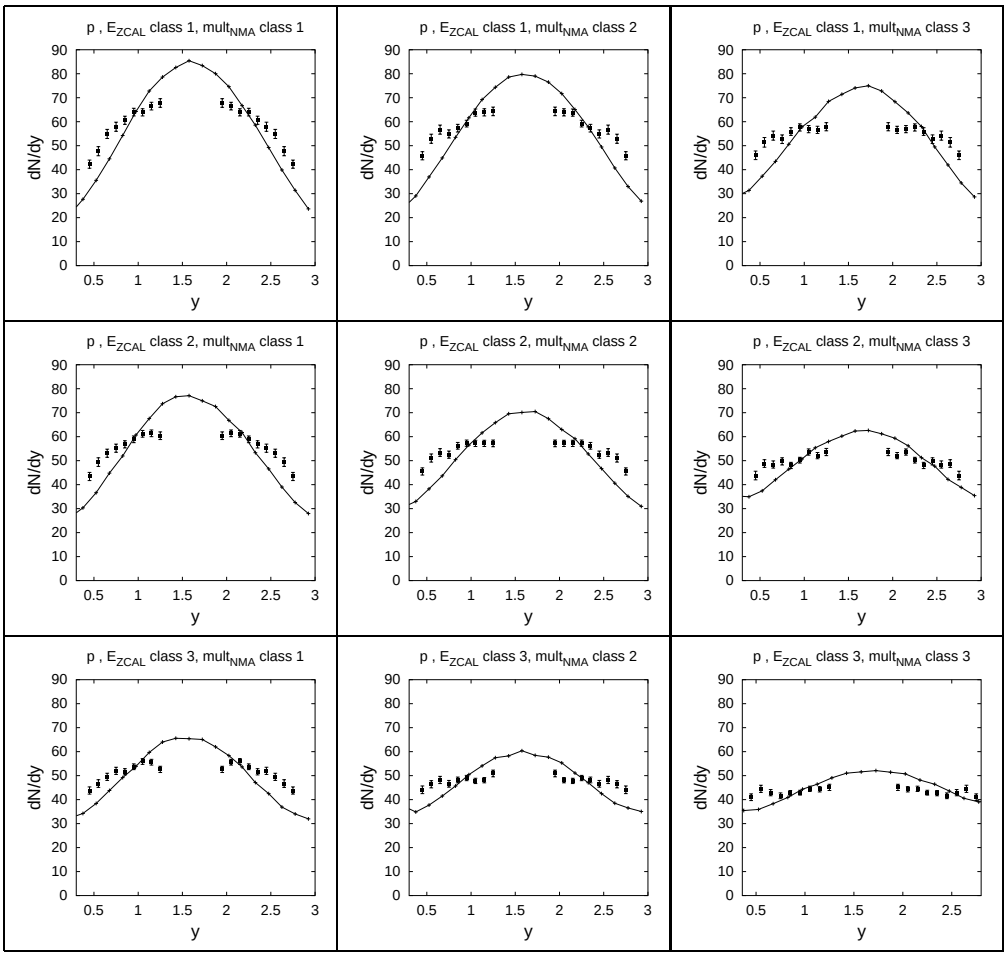

Figure 4.12: Proton rapidity spectra in Au+Au at 10.7 A·GeV double selected by the total multiplicity and the zero degree energy in comparison to data from [A+99]. The centrality decreases from the upper left corner to the lower right.

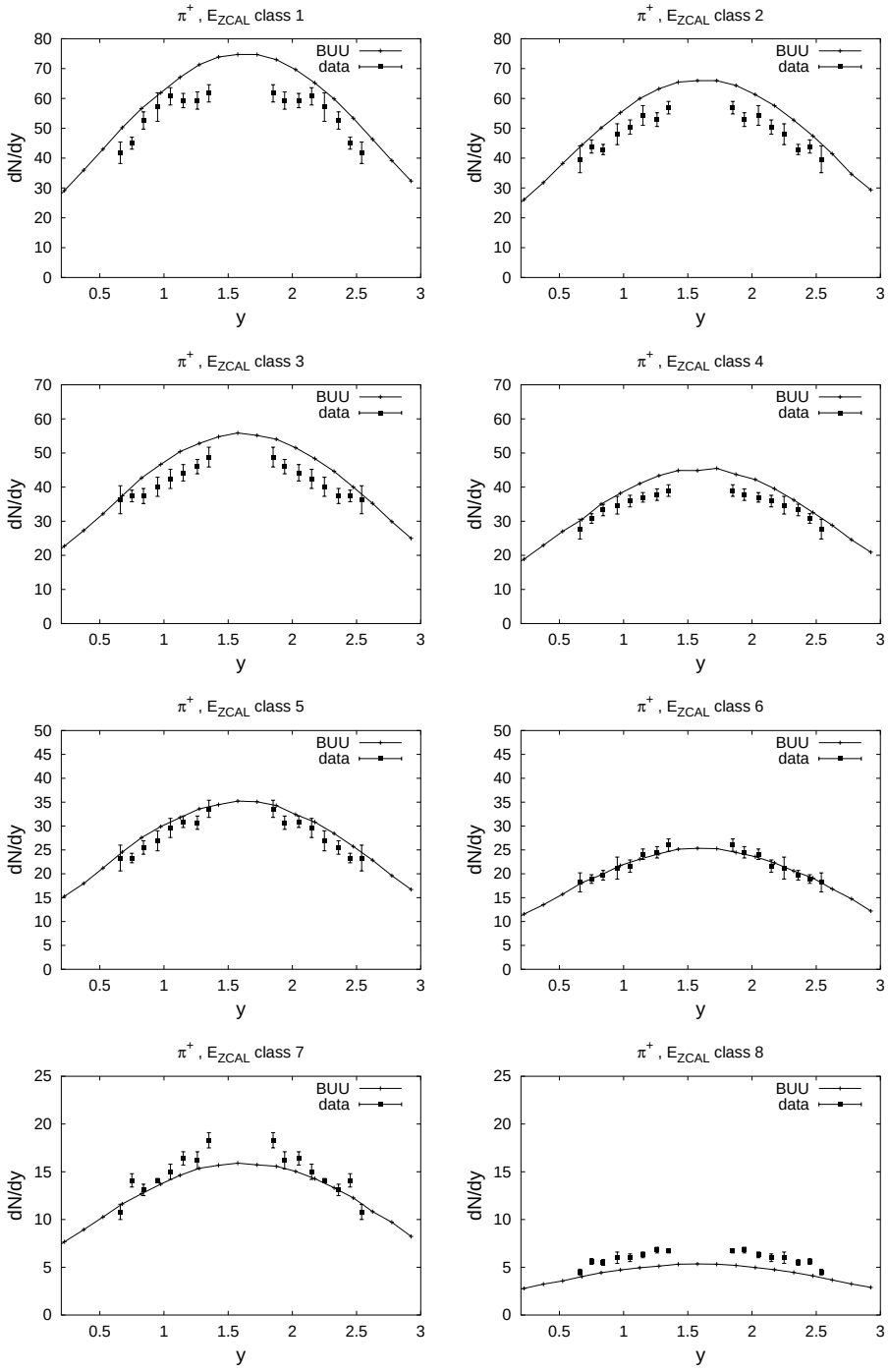

Figure 4.13: Rapidity spectra of π^+ in Au+Au at 10.7 A·GeV characterized by the zero degree energy in comparison to data from [A+99]. The centrality decreases from the upper left corner to the lower right.

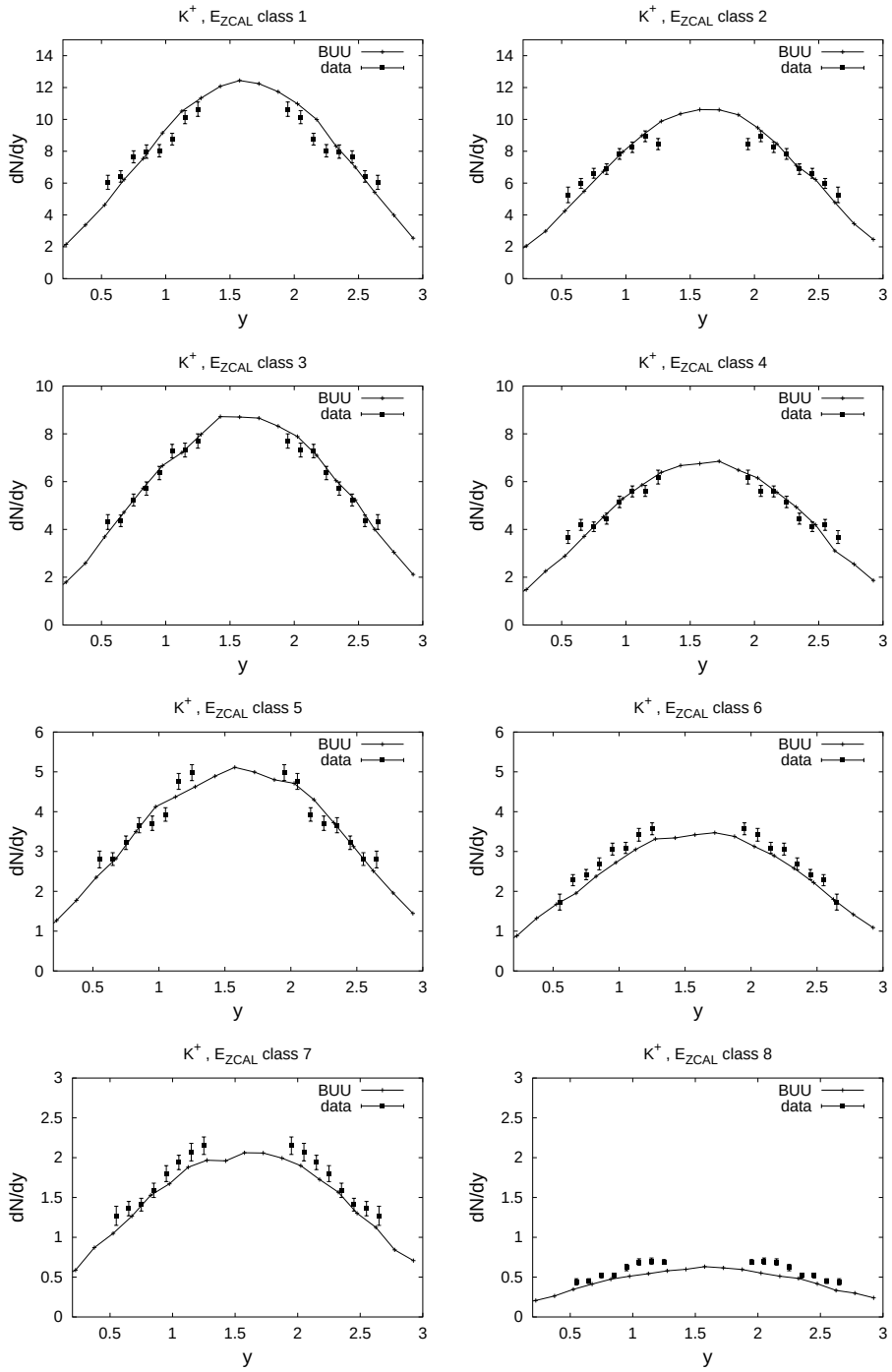

Figure 4.14: Rapidity spectra of K^+ in Au+Au at 10.7 A·GeV characterized by the zero degree energy in comparison to data from [A+99]. The centrality decreases from the upper left corner to the lower right.

the K^+ yields but an improvement for pions and K^-. As we already figured out in Section 3.1.5 we already had too much stopping in the elementary reactions, which might also be a reason for the disagreement with the experimental data. In Fig. 4.13 we see the pion spectra for different centralities selected by the energy measured at zero degree. They show the same development as in the preceding sections. As the centrality increases the data are overestimated, whereas for more peripheral collisions everything is fine and in very peripheral collisions we even underestimate pion production. The kaon spectra in Fig. 4.14 agree pretty well for all centralities. We will discuss the kaon production in more detail in the next section when we look at the production mechanisms for strangeness in central heavy-ion collisions.
Now we want to look at a quantity, which is called the fiducial yield. The fiducial yield is defined as

$$\text{fiducial yield} = \sum_{\text{rapidity intervals}} \frac{dN}{dy} dy \tag{4.8}$$

where the dN/dy are the rapidity distributions selected by zero degree energy and the sum runs between $0.6 < y < 1.3$. The fiducial yield for a specific particle is therefore the number of those particles in the rapidity interval, over which the sum is performed. When one divides the fiducial yield by the number of participant nucleons one gets a measure of how much the secondary collisions influence. If there are no secondary collisions at all for example, the fiducial yield divided by the number of participant nucleons should be flat. Any rise is due to secondary collisions, about which one can get information in that way. In Fig. 4.15 the fiducial yield for K^+ and π^+ per participant nucleon is plotted. The pion data shows a flat beginning whereas in more central collisions the pion yield increases more than linear. Our model shows a continuous quite linear increase, which indicates that the pion production at those energies is not completely understood. The deviations in the fiducial yield can also be due to missing absorption of pions. The kaons show a linear increase which we reproduce very well in our model. In Fig. 4.16 we see the ratio of fiducial yields K^+/π^+ again plotted versus N_{pp}. The data and our model both show a smooth increase as the number of participants increase but we are off as the density increases, which is of course due to the deviations in the pion sector.

4.3.3 Strangeness production

In this section we want to discuss the production of strangeness in a heavy-ion collision according to our model. In particular we want to show a picture, which tells us about the importance of the different channels for strangeness production at different energies. In Fig. 4.17 one sees the number of produced $\overline{s}$-quarks versus time for four different channels. We subtracted the absorption of $\overline{s}$-quarks so that we really see the net gain of strangeness. We see that almost half of the

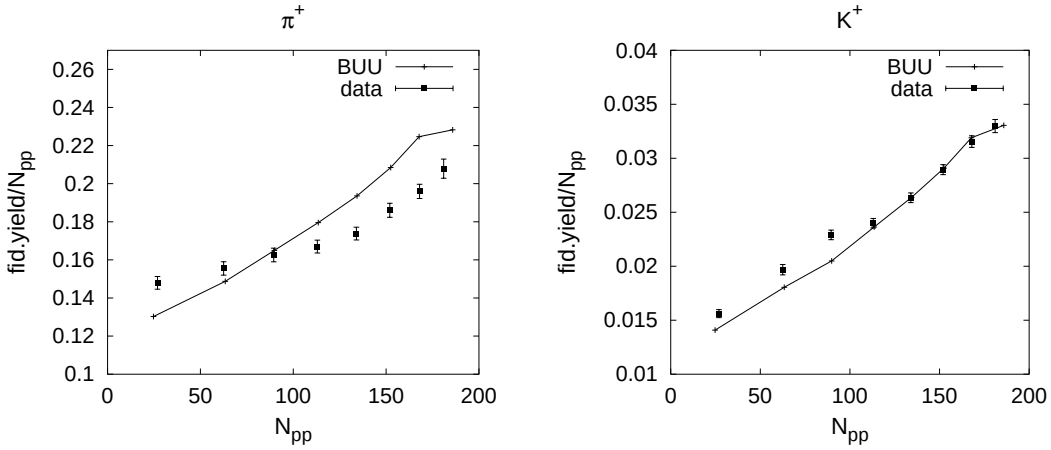

Figure 4.15: Fiducial yields for π^+ and K^+ divided by the number of participants as a function of the number of participants in Au+Au at 10.7 A·GeV in comparison to data from [A+99].

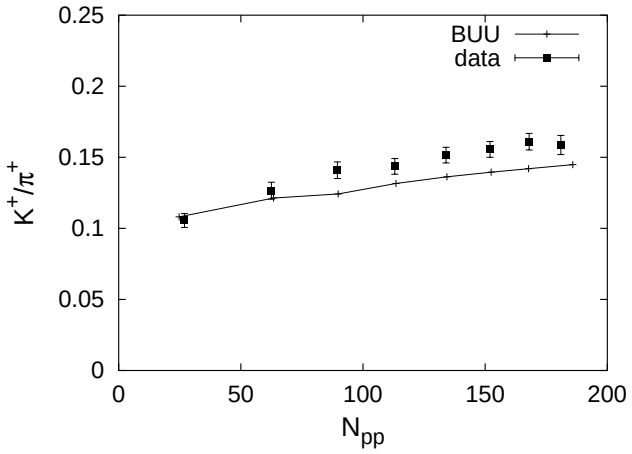

Figure 4.16: The ratio of fiducial yields K^+/π^+ plotted versus N_{pp} in Au+Au at 10.7 A·GeV in comparison to data from [A+99].

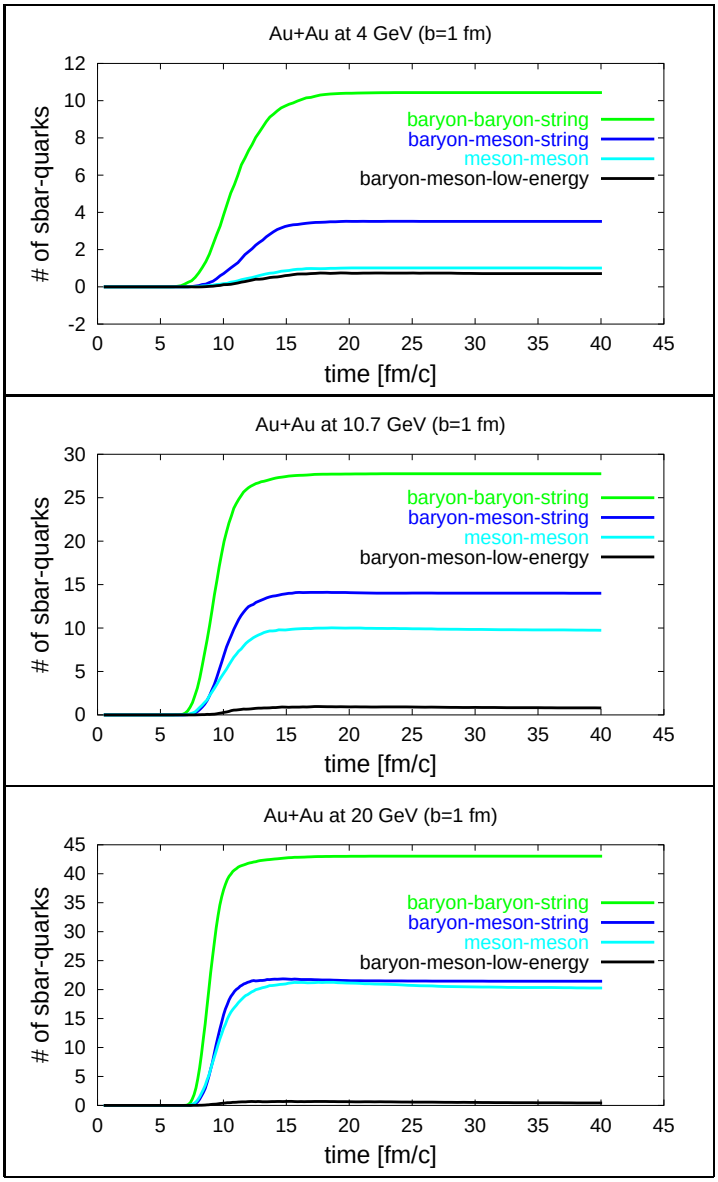

Figure 4.17: Contribution of different channels to strangeness production in Au+Au at 4 A·GeV, 10.7 A·GeV and 20 A·GeV.

strangeness is produced by secondary collisions. We counted only the creation of the $\overline{s}$-quark and we did not consider reactions or decays, as for example $K^* \to K\pi$ where the $\overline{s}$-quark is only shifted from a K^* to a K. We split all production channels into five different sectors. One section is the baryon-baryon channel at high energies or, in other words, the baryon-baryon reactions, which are simulated by the Fritiof string model. The collisions contributing to strangeness production are mostly the first collisions between the nucleons of the target and the projectile. We called the baryon-baryon collisions simulated by the Fritiof model 'baryon-baryon-string' in the picture. The baryon-baryon reactions at invariant energies below the Fritiof threshold, i.e. with $\sqrt{s} < 2.6$, are not plotted because they do not contribute to the strangeness production significantly at the energies we are looking at. We also plotted the contributions from the meson-baryon channels again split into the low-energy region below the threshold for string production and the reactions simulated by the Fritiof model. The fourth channel shows the contribution from the meson-meson collisions.
We see that at lower energies the meson-meson channel plays almost no role whereas at higher energies it becomes more and more important. The baryon-meson channel shows a similar behaviour and its contribution is even more important. The dominant channel is the baryon-baryon string channel and it will be interesting to see how the K^+ spectra evolve with energy. At the lower energies, where the baryon-baryon string channel dominates, we have therefore another possibility to gain information on the strangeness production in nucleon nucleon collisions. In heavy-ion collisions, however, one has to be careful because other effects, as for example a potential, might also influence particle yields.

Chapter 5

Excitation Functions

The K^+/π^+ ratio as a function of beam energy in heavy-ion collisions is of special interest because of its possibility of being a signature for the quark-gluon plasma. In the following we will compare midrapidity yields for pions and kaons in comparison to two other transport codes, HSD [CB99] and UrQMD [Web02], and to data from the experiments E866 and E917 at the AGS [A$^+$00b, A$^+$00a] and the NA49 at CERN [A$^+$02, Fri03]. The transport calculations by all models have been performed in the cascade mode.
The experiments at the AGS were using the multiplicity and the zero degree calorimeter for event characterization, which we already described in Section 4.3.1. The experiment at the AGS studied Au+Au collisions at 1.96 A·GeV, 4 A·GeV, 5.93 A·GeV, 7.94 A·GeV and 10.7 A·GeV. The measured m_t-spectra at 1.96, 4, 5.93 and 7.94 A·GeV in a slice of $0 < \frac{y-y_{nn}}{y_{nn}} < 0.25$ around midrapidity were fitted with the following functions

$$\frac{1}{2\pi m_t}\frac{d^2N}{dm_t dy} = \frac{dN/dy}{2\pi(Tm_0+T^2)}e^{-(m_t-m_0)/T} \qquad \text{for kaons} \qquad (5.1)$$

$$\frac{1}{2\pi m_t}\frac{d^2N}{dm_t dy} = \frac{dN/dy}{2\pi T_S^{2-\lambda}\Gamma(2-\lambda,/m_0/T_S)}m_t^{-\lambda}e^{-m_t/T_S} \qquad \text{for pions} \qquad (5.2)$$

where $dN/dy, T$ and λ are the fit parameters. In case of the pion the scaled exponentials were used because the pion spectra raise above an exponential at low m_t. The data at 10.7 A·GeV were fitted with the same functions but the width of the rapidity interval was chosen only half as big.
The experiment NA49 investigates Pb+Pb collisions at 20 A·GeV, 30 A·GeV, 40 A·GeV, 80 A· GeV and 160 A·GeV. We are interested in the first three energies. The data from the reactions at 20 A·GeV still have to be analysed and published and for the run at 30 A·GeV we found so far only the value for K^+/π^+. For event selection the so called Veto Calorimeter is used, which is based on the same principles as the Zero Degree Calorimeter at the AGS.
In Section 4.3.1 we showed the influence of the different methods for event selection. Since the differences are negligible within our accuracy, we used for

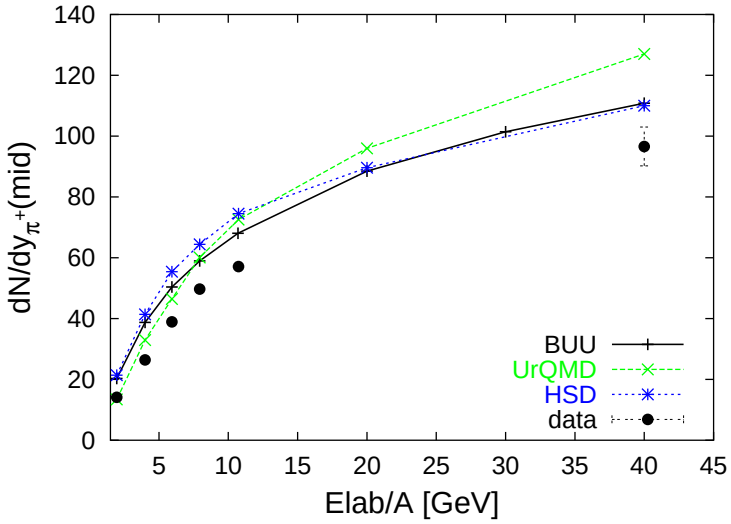

Figure 5.1: Midrapidity yields for π^+ as a function of energy in comparison to results of HSD, results of UrQMD and data from [A$^+$00b, A$^+$02, Fri03].

simplicity a sharp cut for the impact parameter. At the AGS this cut was chosen to be $b < 3.5$ fm and for the calculations at SPS energies we used $b < 4$ fm.
In Fig. 5.1, 5.2, 5.3 and 5.4 we see the midrapidity yields for π^+, K^+, K^- and $\Lambda + \Sigma_0$ as a function of energy. The BUU model overestimates the π^+, K^- and $\Lambda + \Sigma_0$ yields, whereas the results for K^+ are pretty well in line with data, except at the lower energies. At the lower energies the situation for all particles becomes better if we use a potential because the particle production decreases in that case. The reason for that is that some of the energy is stored in the field and will not be available for particle production. But so far we do not have a reliable potential at energies above 2 A·GeV in our model and we run it in the cascade mode. At higher energies the influence of the potential should decrease anyway. Nevertheless we did the same calculations with a potential in order to show the quantitative change. We described the potential already in Chapter 2 in Eq. (2.17). The parameters we use are chosen such that it describes the proton and neutron flow between 0.15 A·GeV and 2 A·GeV [LCGM00]. The results are shown in Tab. 5.1 together with data and the results of the cascade runs. One sees, that at 2 A·GeV and at 4 A·GeV the results really improve and even at 6 A·GeV the midrapidity yields for π^+ and K^+ are closer to data. Only the ratio is described better without potential above 4 A·GeV. In Fig. 5.8 we see the K^+/π^+ ratio calculated with and without potential. At lower energies we agree with data by using the potential, at intermediate energies we are too low and at energies above 20 GeV the two curves merge.
Another reason for the overestimation of K^+ at low energies is the fact that we already overestimate K^+ in elementary pp reactions, as we showed in Section

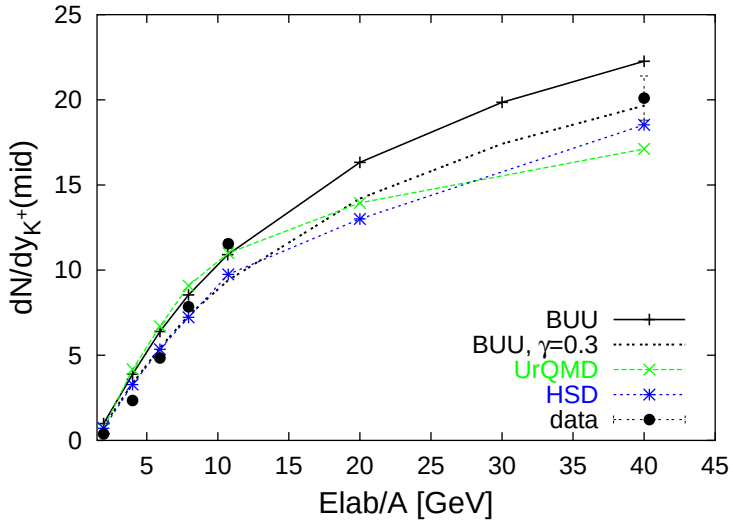

Figure 5.2: Midrapidity yields for K^+ as a function of energy in comparison to results of HSD, results of UrQMD and data from [A$^+$00b, A$^+$02, Fri03].

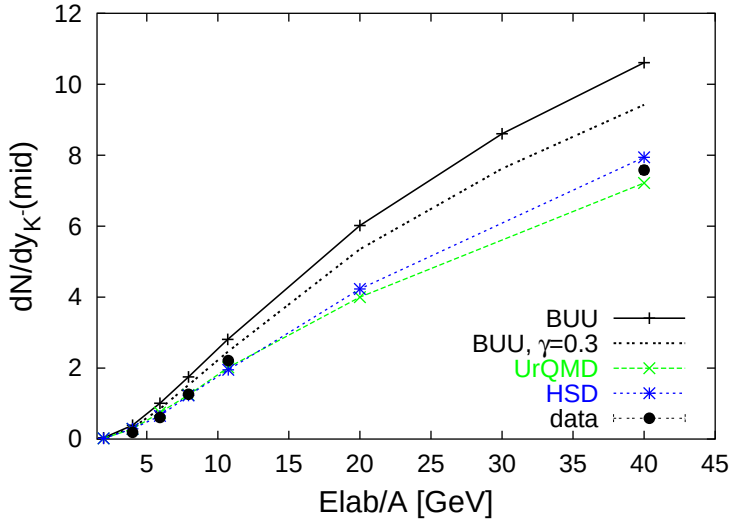

Figure 5.3: Midrapidity yields for K^- as a function of energy in comparison to results of HSD, results of UrQMD and data from [A$^+$00a, A$^+$02, Fri03].

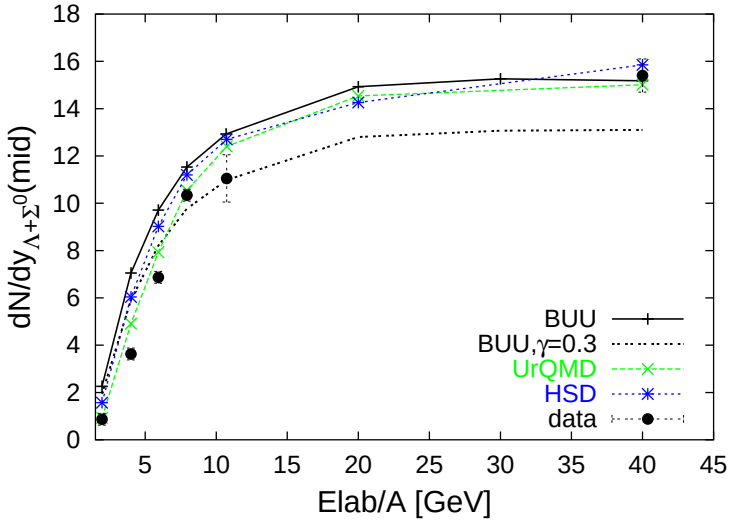

Figure 5.4: Midrapidity yields for $\Lambda + \Sigma_0$ as a function of energy in comparison to results of HSD, results of UrQMD and data from [M$^+$02, M$^+$03, A$^+$96, Pin02, Ant99].

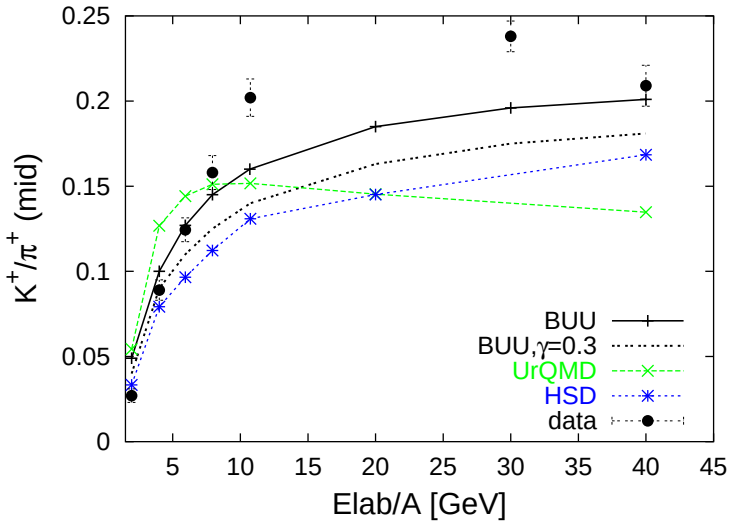

Figure 5.5: The K^+/π^+ ratio at midrapidity as a function of energy in comparison to results of HSD, results of UrQMD and data from [A$^+$00b, A$^+$02, Fri03].

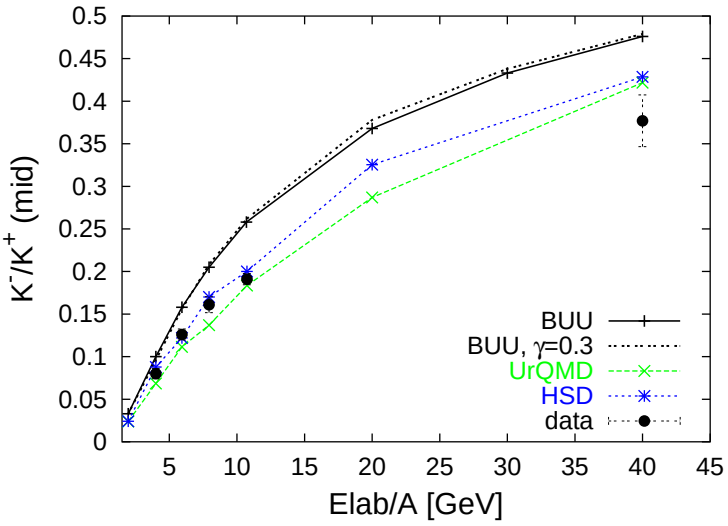

Figure 5.6: The K^-/K^+ ratio at midrapidity as a function of energy in comparison to results of HSD, results of UrQMD and data from [A$^+$00a, A$^+$02, Fri03].

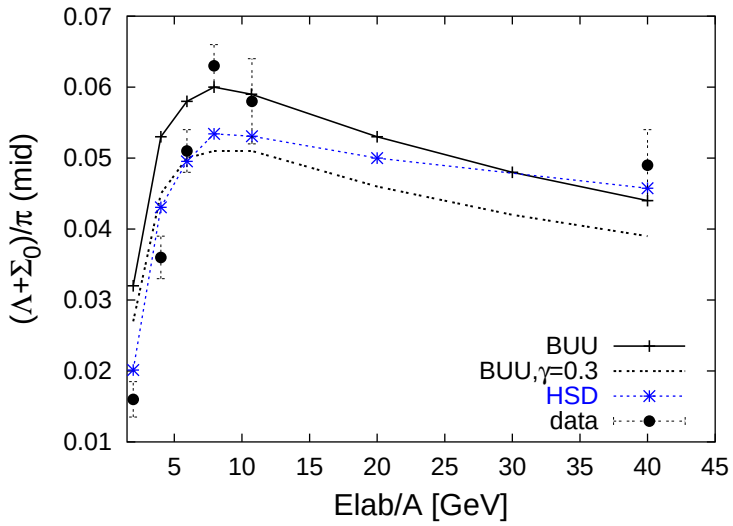

Figure 5.7: The $(\Lambda + \Sigma^0)/\pi$ ratio at midrapidity as a function of energy in comparison to data from [M$^+$02, M$^+$03, A$^+$96, Pin02, Ant99], where $\pi = 1.5(\pi^+ + \pi^-)$.

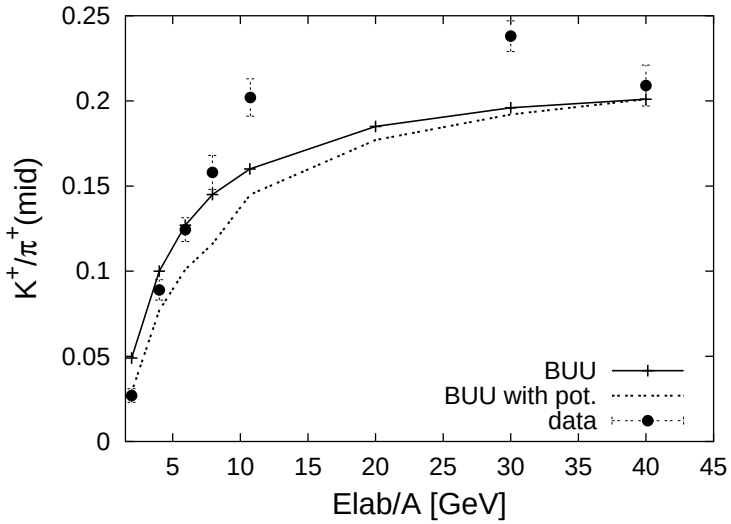

Figure 5.8: K^+/π^+ ratio as a function energy with and without potential in comparison to data from [A$^+$00b, A$^+$00a, A$^+$02].

Elab	$dN/dy_{\pi^+}(mid)$			$dN/dy_{K^+}(mid)$			$K^+/\pi^+(mid)$		
	wp	wop	data	wp	wop	data	wp	wop	data
2 GeV	17.71	20.3	14.1	0.56	0.99	0.381	0.032	0.049	0.027
4 GeV	34.69	38.74	26.4	2.9	3.89	2.34	0.084	0.10	0.089
6 GeV	45.91	50.39	38.9	5.12	6.39	4.84	0.11	0.127	0.1244
8 GeV	54.64	58.97	49.7	7.21	8.54	7.85	1.32	0.145	0.158

Table 5.1: Midrapidity yields for π^+ and K^+ at AGS energies calculated within the BUU model with and without potential in comparison to data, where wp corresponds to the calculations with potential and wop to the calculations without potential. The data are quoted without errors since they will only give an orientation.

3.1.5. As in Section 3.1.5 we also show the calculations with a strangeness suppression factor γ=0.3 in case of strange particles. The pions are not affected by the different choices of γ. In the K^+ excitation function it is hard to judge which γ describes data better. The deviations in the K^--excitation function increase with increasing energy. That might be due to too high cross sections for strangeness production in the meson-meson channel. This assumption is supported by the K^-/K^+ excitation function in Fig. 5.6. The reason for the rise in that function is on the hand due to the increasing probability of producing K^- instead of hyperons in nucleon nucleon collisions as the energy increases. But as we saw in Section 4.3.3 the meson-meson collisions become very important for strangeness production and here the number of produced K^+ is equal to the number of produced K^- and those reactions will strongly increase the K^-/K^+ ratio. The lower suppression improves the situation for the K^- yields but it has no almost no influence on the K^-/K^+ ratio. The $\Lambda + \Sigma^0$ yields are too high at low energies, which might be compensated by a potential as already mentioned. By choosing $\gamma = 0.3$ we see that we are closer to data except at 40 A·GeV. The slope of The $\Lambda + \Sigma^0$ excitation function is reproduced nicely with both suppression factors. The problem with hyperons at lower energies is of course linked to the problems with kaons, because they are mainly produced together at the lower energies and they are linked via the strangeness-exchange cross sections $\overline{K}N \leftrightarrow \pi Y$. The biggest problem occurs in the pion sector, where we are off at all energies and which cannot be explained. As we already saw, the same problem occurred in Chapter 4 when we increased the system size. A similar problem is observed at lower energies (0.4-1.5 A·GeV), where pions are also overestimated [LM03]. There the problem could be cured by employing a medium modified cross section for $NN \leftrightarrow N\Delta$. Since at higher energies the Fritiof string model is employed, one cannot just modify the resonances. Here one would also have to modify the string model and then the question arises how to treat the endless number of different final states.
Before we comment on the other two transport codes, we want to summarize the most important facts about the two codes in comparison to our code. For details we refer to [CB99] and [Web02]. Although the three codes are different in numerical realisation they are based on the same concepts : string and hadronic degrees of freedom. For the calculations in that work, none of the codes employed non standard modification, as for example an explicit phase transition to a quark-gluon plasma. All calculation have been performed in the cascade mode. The philosophy is that a common failure of all models should indicate the appearance of 'new physics'.

The UrQMD model

The UrQMD transport approach includes all baryon resonances up to 2 GeV

and all mesonic resonances up to 1.9 GeV as tabulated in the PDG [C+00]. Up to invariant energies of about 2 GeV the particle production is simulated by the production of resonances in inelastic collisions and their decay. At higher energies UrQMD includes the possibility to create an effective heavy resonance in the meson-baryon and the meson-meson channels. The decay of those effective resonances is simulated by the string fragmentation model. At even higher energies the resonance picture is left behind and the string model is used. The string model they use has a few differences to the string model we use. First of all the formation time, UrQMD uses, is of the order 1-2 fm/c and depends on the momentum and energy of the produced particle. This dependence comes from the fact that the so called yo-yo formation time definition is used, where the formation point has the coordinates of the quark trajectories intersection. The cross sections during the formation time is 0 for a particle with none of the original quarks and reduced by $\frac{1}{3}\cdot\#$(constituent leading quarks) in case of a leading particle. For a leading meson the cross section is reduced by 0.5. Another difference is the fragmentation function. For leading nucleons they use

$$f(x) = \exp\left(-\frac{(x-B)^2}{2A^2}\right), \tag{5.3}$$

where A=0.275 and B=0.42. For newly produced particles UrQMD uses

$$f(x) = (1-x)^2. \tag{5.4}$$

The suppression factors for strangeness production and diquark production are

$$\text{UrQMD}: \quad u:d:s:diquark = 1:1:0.35:0.1. \tag{5.5}$$

The HSD model

The HSD transport approach incorporates the baryon octet and decuplet states and N*(1440), N*(1535) as well as their antiparticles and 0^- and 1^- meson octets. In contrast to the resonance concept HSD includes the direct meson production in order to describe the cross sections. The HSD model uses the same string model we use and also the same formation time (see Chapter 3). Even though the string fragmentation function is the same (Eq. (3.31)), HSD uses different values for the parameters a and b, namely $a = 0.23$ and $b = 0.34$ GeV^{-2}. The influence of the different parameters is hard to quantify since our fragmentation depends on m_t. But qualitatively the difference is small and the fragmentation in HSD has a slightly higher probability to produce faster particles. The transverse momentum is also chosen according to a Gaussian but the width is taken to be $\sigma = 0.5$ GeV in HSD. The suppression factors are again the same as in our model.

Now we want to look at the results. In general one can say that the codes give very similar results and only in the K^- yields at midrapidity, we disagree with the other codes and data. The differences in the yields for other particles do not look very pronounced but they can be seen better when we look directly at the ratios in Fig. 5.5 and Fig. 5.6. HSD describes the ratio at low energies very well, whereas is cannot reproduce the slope in the ratio which seems to be too flat. At 40 A·GeV it catches up but it clearly does not reproduce the maximum at 30 A·GeV. UrQMD overestimates the ratio at the lower energies but seems to reproduce the slope in the ratio pretty well although it is decreasing to early. It is the only code, which shows a maximum in the ratio, even though it is at the wrong energy. We lie somehow in between the two other curves. We also overestimate the data at low energies and our slope is not steep enough. Therefore we catch up with data at 6 A·GeV. At 10 A·GeV and 30 A·GeV we are off and we also do not reproduce the maximum. The reason for the disagreement however is in all codes due to the high pion abundances and not due to the strangeness, which seems to be described well. In case of $\gamma = 0.3$ we describe the low energy data better but fail to describe the data at higher energies. The K^-/K^+ ratio is described well by HSD and UrQMD, whereas we are too high, as already discussed. In Fig. 5.7 we see the $\Lambda + \Sigma_0/\pi$ ratio as a function of energy, which shows the same peaky behaviour as the K^+/π^+ ratio. However, in that case we reproduce the peak and the slope even though we are again off at the lower energies. The peak in that ratio is, however, most probably due to a domination of mesons over baryons at higher energies and the production of hyperons in meson collisions is very improbable. The lower suppression factor again only improves the calculation at the lower AGS energies and worsens the situation at the higher energies.
In Fig. 5.9 we see the K^+/π^+ ratio in comparison to data with different versions of the BUU model. The calculations without the annihilation processes differ from the standard version at the AGS energies and shows no difference to the standard version at SPS energies. One sees that the annihilation processes increase the slope in the K^+/π^+ ratio. The meson-meson collisions influence the ratio significantly at energies above 6 A·GeV. That was expected since meson-meson collisions become more and more important at those energies.
In Fig. 5.10 we see the inverse slope parameters for K^+. We clearly cannot describe the slope at all energies and we do not reproduce the raise in the inverse slope parameter. This is a clear sign that we miss pressure producing mechanisms in our code. There are recent studies within the transport codes HSD and UrQMD, which show the same problems [BSS+04].

5.1 The Statistical Model

The statistical methods offer another possibility to interpret the data from the SPS and the AGS. The fundamental assumption for applying the statistical model

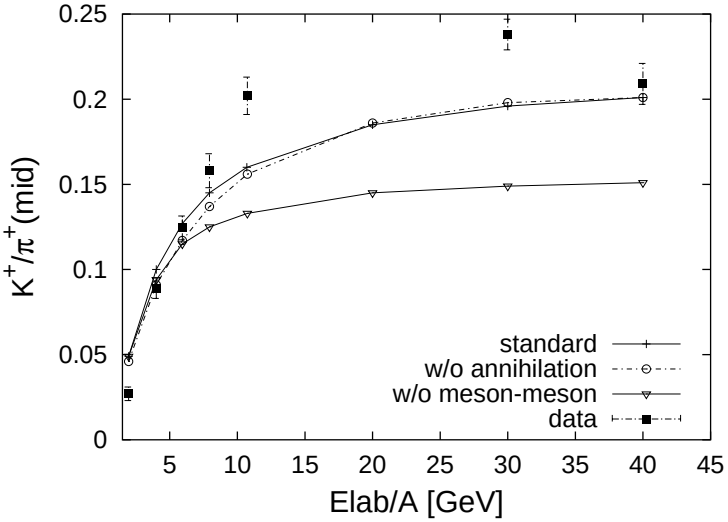

Figure 5.9: K^+/π^+ ratio calculated by the BUU model in the standard version, without annihilation processes and without meson-meson collisions in comparison to data from [A$^+$00b, A$^+$02, Fri03].

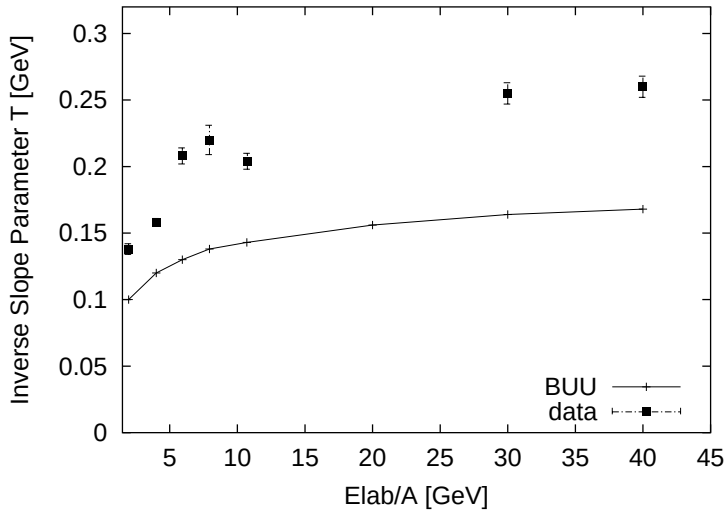

Figure 5.10: Inverse slope parameter for K^+ as a function of energy in comparison to data from [A$^+$00a, A$^+$02, Fri03].

is that the particles are in chemical and thermal equilibrium at freeze out. If one makes that assumption and starts the machinery of statistics, the abundances of particles can be well described with two parameters, the temperature T and the baryochemical potential μ_B. In the following we will describe the statistical model which is used in the calculations and afterwards compare the model calculations, which were done by [BMCOR02], to data and to our model.

5.1.1 The Grand Canonical ensemble

In case of a system with many particles one uses the grand canonical ensemble to describe the partition function, which is in that case given by

$$Z^{GC}(T, V, \mu_Q) = \mathrm{Tr}\left[e^{-\beta(H-\sum_i \mu_{Q_i} Q_i)}\right], \tag{5.6}$$

where H is the Hamiltonian of the system, $\beta = 1/T$ the temperature , the Q_i are the conserved charges and μ_{Q_i} are the chemical potentials that guarantee that the charges Q_i are conserved on the average in the whole system. The Hamiltonian is usually taken such as to describe a hadron resonance gas. The partition function of a hadron resonance gas can then be written as a sum of partition functions of the considered particles

$$\ln Z(T, V, \mu) = \sum_i \ln Z_i(T, V, \vec{\mu}), \tag{5.7}$$

where $\vec{\mu} = (\mu_B, \mu_S, \mu_Q)$, with the chemical potentials responsible for the conservation of baryon number, charge and strangeness. In case of a free Fermi gas $\ln Z_i$ is given by

$$\ln Z_i(T, V, \vec{\mu}) = \frac{V g_i}{2\pi^2} \int_0^\infty p^2 \ln(1 \pm \lambda_i \exp(-\beta\epsilon_i)) dp \tag{5.8}$$

with the fugacity

$$\lambda_i = \exp(\beta(B_i\mu_B + S_i\mu_S + Q_i\mu_Q)). \tag{5.9}$$

B_i, S_i and Q_i are the baryon number, the strangeness and the charge of the particle species we are looking at. g_i and m_i are the spin-isospin degeneracy factor and the mass. The plus sign inside the logarithm stands for fermions and the minus sign for bosons. Expanding the logarithm and performing the momentum integration in Eq. (5.8) we obtain

$$\ln(Z_i)(T, V, \mu) = \frac{V g_i}{2\pi^2 \beta} \sum_{k=1}^{\infty} \frac{(\pm 1)^{k+1}}{k^2} \lambda_i^k m_i^2 K_2(\beta k m_i), \tag{5.10}$$

where K_2 is the modified Bessel function. The average number of particles is then obtained by differentiating with respect to λ_i and multiplying by λ_i

$$\langle N_i \rangle(T, \vec{\mu}, V) = \frac{V g_i}{2\pi^2 \beta} \sum_{k=1}^{\infty} \frac{(\pm 1)^{k+1}}{k} \lambda_i^k m_i^2 K_2(\beta k m_i). \tag{5.11}$$

The strangeness chemical potential, the charge chemical potential and the volume are fixed by the three conservation laws

$$\text{baryon number}: \quad \sum_i \langle N_i \rangle B_i = Z + N, \tag{5.12}$$

where Z is the number of protons and N the number of neutrons of the colliding system;

$$\text{strangeness}: \quad \sum_i \langle N_i \rangle S_i = 0 \tag{5.13}$$

and

$$\text{charge}: \quad \sum_i \langle N_i \rangle = \frac{Z-N}{2}. \tag{5.14}$$

The number of independent parameters is therefore reduced to the temperature T of the system and the baryo-chemical potential. These two parameters can now be fitted to particle spectra at the energies of interest. In general it would now be possible to calculate all particle multiplicities. However, in the grand canonical ensemble the conservation laws are only valid in the average and in smaller system this approximation becomes questionable. That is why we want to look at the Canonical ensemble in the next section.

5.1.2 The exact conservation of charges

At low AGS energies and SIS energies one has to account for the exact conservation of the charges. In the following we will introduce the formalism, which is necessary in order to do that. We will see that this will introduce a suppression factor.
We will start out by rewriting the grand canonical partition function. For simplicity we will only consider a partition function with one conserved charge namely strangeness.

$$Z(\mu_s, V, T) = \mathrm{Tr}\left[e^{-\beta(H-\mu_S S)}\right] = \sum_{s=-\infty}^{\infty} \mathrm{Tr}_S[e^{-\beta H}]e^{s\beta\mu_S} = \sum_{s=-\infty}^{\infty} Z_S \lambda_S^s, \tag{5.15}$$

where $\lambda_S = e^{\beta\mu_S}$ is the fugacity and

$$Z_S = \mathrm{Tr}_S[e^{-\beta H}] \tag{5.16}$$

is the partition function which sums over all states with a total strangeness S. This is the canonical partition function with respect to strangeness conservation. We note that Z_S can be interpreted as the coefficient in the Laurent series for Z with respect to λ_S. Thus we may apply Cauchy's formula and take an inverse transformation to obtain

$$Z_S(T,V) = \frac{1}{2\pi i}\oint \frac{d\lambda_S}{\lambda_S^{s+1}} Z(\lambda_S, T, V) = \int_{-\pi}^{\pi} \frac{d\phi}{2\pi} \tilde{Z}(\phi, T, V) e^{-is\phi}, \tag{5.17}$$

where we chose the unit circle as integration path and $\tilde{Z}(\phi, T, V) = Z(\lambda_S = e^{i\phi}, T, V)$. Equation (5.17) is a projection procedure to get Z_S out of Z. Now we rewrite Eq. (5.6) and we only consider particles with strangeness ± 1 and 0 :

$$\tilde{Z} = \exp(N_{S=0} + N_{S=1}e^{i\phi} + N_{S=-1}e^{-i\phi}) \tag{5.18}$$

with

$$N_{S=0,\pm 1} = \sum_k Z_k^1, \tag{5.19}$$

where the sum over k runs over all particles having strangeness ± 1 and 0 and Z_k^1 is the one particle partition function which we get from Eq. (5.11) by keeping only the first term of the sum

$$Z_k^1 = \frac{V g_k}{2\pi^2} m_k^2 \frac{1}{\beta} K_2(m_k\beta) \exp(B_k\mu_B + Q_k\mu_Q). \tag{5.20}$$

Z_S is now obtained by

$$Z_S = Z_0 \frac{1}{2\pi} \int_0^{2\pi} d\phi e^{-iS\phi} e^{N_{S=1}e^{i\phi} + N_{S=-1}e^{-i\phi}}, \tag{5.21}$$

where $Z_0 = e^{N_{S=0}}$ is the partition function of all particles having zero strangeness. Rewriting the above equation as

$$Z_S = Z_0 \frac{1}{2\pi} \int_0^{2\pi} d\phi e^{-iS\phi} e^{\sqrt{N_{s=1}N_{s=-1}}\left(\sqrt{\frac{N_{S=1}}{N_{S=-1}}}e^{i\phi} + \sqrt{\frac{N_{S=-1}}{N_{S=1}}}e^{-i\phi}\right)} \tag{5.22}$$

and using the following relation for the modified Bessel functions $I_k(x)$

$$e^{\frac{x}{2}\left(t+\frac{1}{t}\right)} = \sum_{-\infty}^{\infty} t^k I_k(x), \tag{5.23}$$

we get

$$Z_S = Z_0 \frac{1}{2\pi} \int_0^{2\pi} d\phi \sum_{k=-\infty}^{\infty} I_k(x) \left(\frac{S_1}{S_{-1}}\right)^{k/2} e^{i\phi(S-k)}, \tag{5.24}$$

where $S_{\pm 1} = N_{S=\pm 1}$ and $x = 2\sqrt{S_1 S_{-1}}$. Thus for a hadron gas with net strangeness S we end up with

$$Z_S(T, V, \mu_B, \mu_Q) = Z_0(T, V, \mu_B, \mu_Q) \left(\frac{S_1}{S_{-1}}\right)^{S/2} I_S(x). \tag{5.25}$$

The calculation of the particle density n_k amounts to the replacement $Z_k^1 \to \lambda_k Z_k^1$ of the corresponding one particle partition function and taking the derivative of

the logarithm of the canonical partition function with respect to the fugacity λ_k and multiplying by λ_k

$$n_K^C = \lambda_k \frac{\partial}{\partial \lambda_k} \ln Z_S(\lambda_k)|_{\lambda_k=1}. \tag{5.26}$$

As an example we compare this result to the grand canonical result for the density of K^+. According to the formulas just derived the density for kaons in the canonical formalism is given by

$$n_{K^+}^C = \frac{Z_{K^+}^1}{V} \frac{S_{-1}}{\sqrt{S_1 S_{-1}}} \frac{I_{S-1}(x)}{I_S(x)}. \tag{5.27}$$

In the grand canonical approach the density is given by

$$n_{K^+}^{GC} = \frac{Z_{K^+}^1}{V} \lambda_s. \tag{5.28}$$

By looking at Eq. (5.18) we see that the strangeness neutrality condition requires

$$\lambda_S S_1 - \lambda_S^{-1} S_{-1} = 0, \tag{5.29}$$

which means that $\lambda_S = S_{-1}/\sqrt{S_1 S_{-1}}$. Therefore the difference of the two approaches is given by the ratio of the modified Bessel functions. The canonical suppression factor, which we call F_S thus reads

$$F_S = \frac{I_1(x)}{I_0(x)}. \tag{5.30}$$

The factor is quantified in Fig. 5.11, which is taken from [BMRS03]. It is plotted versus the participant nucleons multiplied with the particle densities of particles with $S = \pm 1$. We see that at the low AGS energies and at the SIS energies this suppression factor becomes quite important, whereas for higher energies it is almost 1.

5.1.3 Results

Now that we explained the basics of the formalism we want to compare calculations for the ratio of K^+/π^+ done with the statistical model to data and to our results. The calculations within the statistical model were performed in [BMCOR02]. They employed the canonical formalism, which we just described, except that they also considered multi strange particles. In that case the partition function reads

$$Z_{S=0}^C = \frac{1}{2\pi} \int_0^{2\pi} d\phi \exp\left(\sum_{n=-3}^{3} S_n e^{in\phi} \right) \tag{5.31}$$

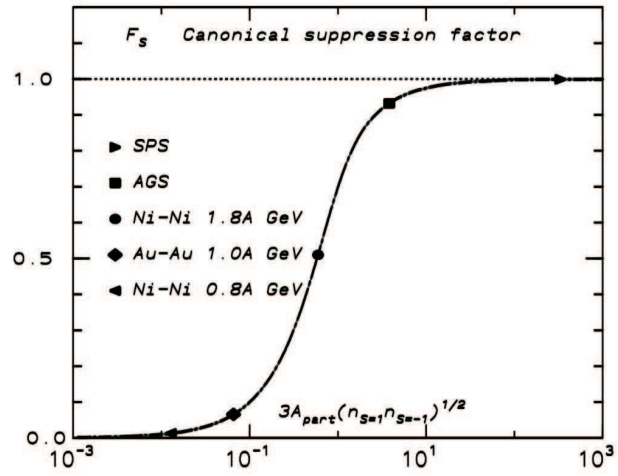

Figure 5.11: Canonical suppression factor (see text).

with the same notation as before. The result for that integral is given by

$$Z^C_{S=0} = e^{S_0} \sum_{n=-\infty}^{\infty} \sum_{p=-\infty}^{\infty} a_3^p a_2^n a_1^{-2n-3p} I_n(x_2) I_p(x_3) I_{-2n-3p}(x_1), \tag{5.32}$$

where $a_i = \sqrt{S_i/S_{-i}}$ and $x_i = 2\sqrt{S_i S_{-i}}$. The energy dependence of μ_B is parametrized as follows

$$\mu_B(s) = \frac{a}{1+\sqrt{s}/b}, \tag{5.33}$$

where $a = 1.27$ GeV and $b = 4.3$ GeV. At freeze-out the chemical potential is related to the temperature via the phenomenological condition of fixed energy per hadron, namely

$$\langle E \rangle / \langle N \rangle \simeq 1\,\text{GeV}. \tag{5.34}$$

The results of those calculations can be seen in Fig. 5.12. We see that our model produces nearly the same curve as the statistical model. That might indicate that the equilibrium condition is really fulfilled in a heavy-ion collision. However, in order to get chemical equilibrium we have to fulfill detailed balance. At the low-energy collisions below the threshold for string production this is indeed the case, but for the string reactions we do not have included any back reactions. It is not possible to include all back reactions since Fritiof produces a very large number of different final states. In [Cas02] first attempts have been made to include multi particle collisions, but only for a small number of reactions. It is hard to say which channels are the most important ones in order to fulfill detailed balance because it is not necessarily the case that if the reaction in one direction

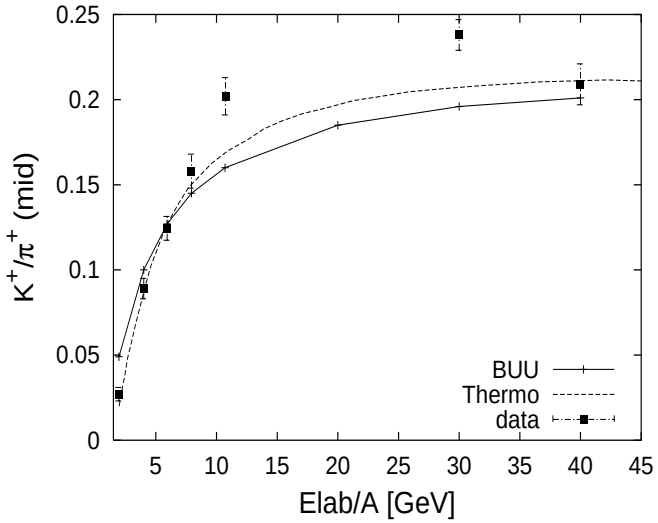

Figure 5.12: K^+/π^+ ratio as a function of energy in comparison to the statistical model and data from [A$^+$00b, A$^+$02, Fri03].

is important, the back reaction has also to be important. However, in our result it seems as if we are almost in equilibrium even without multi particle collisions but still it would be worthwhile to spend some effort on that issue.
In comparison to data the statistical model has also problems to describe the 10 A·GeV point and the data point at 30 A·GeV.

Chapter 6

Off-shell pions, resonance lifetimes and string-string collisions

As already mentioned the density in a heavy-ion collision at AGS and SPS energies can be pretty high and therefore collective effects can take place. In this chapter we want to investigate three different effects. First we will look at the effect of off-shell pions on the particle production. The motivation is that due to the width of those particles in the medium they can propagate with higher masses than usual and therefore the collisions can take place at higher invariant energies, which might have an influence on the particle production. Second we will investigate the influence of a modification of resonance lifetimes and especially the Δ lifetime. Δ resonances are produced abundantly in heavy-ion collisions and a modification of their lifetime might have an influence on the particle production. If a Δ lives longer for example, collisions will take place at a higher invariant energy in comparison to the collisions of the nucleon and the pion separately, which are bond together in the Δ. The third effect we will study are string-string collisions. Due to numerous high-energy collisions a lot of strings are created. As already mentioned in Chapter 3, the strings do not decay immediately, they have a formation time. So it is reasonable to introduce some kind of interaction for those objects, which will be discussed in Section 6.3.

6.1 Off-shell pions

The most frequently produced particles in a heavy-ion collision are the pions. Especially at the energies under consideration they are produced abundantly. As the pions propagate through the nuclear matter they might be absorbed by the nucleons and a resonance is created. Due to this absorption pions acquire a width in the medium. The spectral function for pions in a nuclear medium

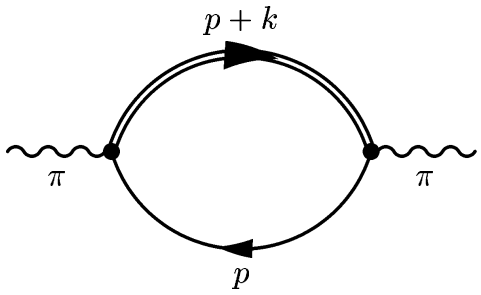

Figure 6.1: Feynman graph representing $-i\Pi$ (see text).

was calculated by different authors and we will use the results of the calculation performed by Larionov et al. [LM02]. That calculation was done on the basis of the Δ-hole-model [EW88]. In order to calculate the pion polarization function $\Pi(k)$, one has to evaluate the Feynman graph, which is shown in Fig. 6.1. The Lagrangian which was used in [LM02] is the following

$$\mathcal{L}_{\pi N\Delta} = \frac{f_\pi N\Delta}{m_\pi}\overline{\Psi}^\mu_\Delta \mathbf{T}\Psi_N\partial_\mu\pi + h.c., \tag{6.1}$$

where $\mathbf{T}$ is the isospin transition operator$(1/2 \to 3/2)$, Ψ^μ_Δ is the Rarita-Schwinger field of the Δ-resonance, Ψ_N and π are the nucleon and the pion fields. For details of the calculation we refer to [LM02]. The results for the imaginary and the real part of the polarization function are

$$\mathrm{Re}\Pi(k) = \int \frac{2d^3p}{(2\pi)^3}\frac{m_N}{E_N(\vec{p})}n(\vec{p})\frac{p_{rel}(s-m_\Delta^2)}{\Gamma_\Delta(s)\sqrt{s}}\frac{4}{3}\sigma_{\pi^+p\to\Delta^{++}}(s,k^2), \tag{6.2}$$

$$\mathrm{Im}\Pi(k) = -\int \frac{2d^3p}{(2\pi)^3}\frac{m_N}{E_N(\vec{p})}n(\vec{p})p_{rel}\frac{4}{3}\sigma_{\pi^+p\to\Delta^{++}}(s,k^2), \tag{6.3}$$

where p_{rel} is the pion momentum in the restframe of a nucleon. Using

$$\frac{4}{3}\sigma_{\pi^+p\to\Delta^{++}} = \sigma_{\pi p\to\Delta} + \sigma_{\pi n\to\Delta}, \tag{6.4}$$

we can rewrite Eq. (6.3) in a more intuitive form

$$\mathrm{Im}\Pi(k) = -\frac{\rho}{2}\left\langle \frac{m_N}{E_N(\vec{p})}p_{rel}(\sigma_{\pi p\to\Delta} + \sigma_{\pi n\to\Delta})\right\rangle, \tag{6.5}$$

where the averaging is performed with respect to the nucleon momentum and ρ is the nuclear matter density. In addition the pion polarization function is corrected

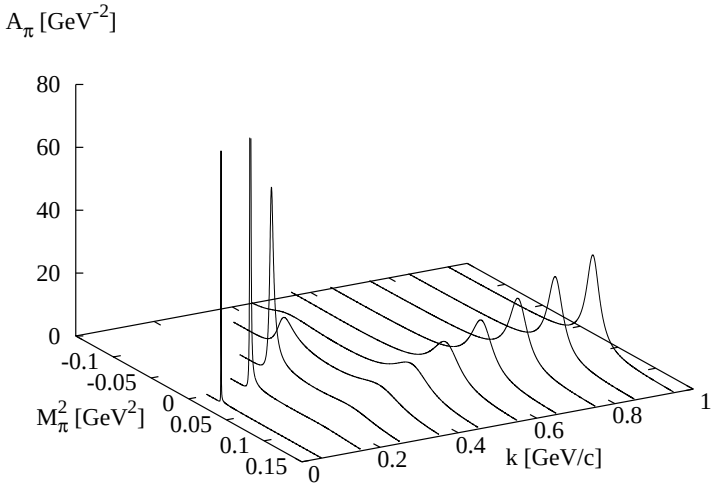

Figure 6.2: Pion spectral function in nuclear matter at the density $\rho = \rho_0$ and temperature $T = 5$ MeV shown versus mass squared and momentum.

for the repulsive interaction of holes and Δ resonances at short distances

$$\Pi_c(k) = \frac{|\vec{k}|^2 \Pi(k)}{|\vec{k}|^2 - g' \Pi(k)}, \tag{6.6}$$

with the Migdal parameter $g' = 0.5$. The pion four-momentum k has to be taken in the restframe of nuclear matter. The quantity we really wanted to know is the spectral function, which is given by

$$A_\pi(k) \equiv -\frac{1}{\pi} \mathrm{Im} G(k) = -\frac{1}{\pi} \frac{\mathrm{Im}\Pi_c(k)}{(k^2 - m_\pi^2 - \mathrm{Re}\Pi_c(k))^2 + (\mathrm{Im}\Pi_c(k))^2}, \tag{6.7}$$

where $G(k) = (k^2 - m_\pi^2 - \Pi_c(k))^{-1}$ is the pion propagator. The spectral function at normal nuclear matter density and $T = 5$ MeV is plotted in Fig. 6.2 versus momentum and M_π^2.
In case a resonance is decaying into a final state including a pion, the mass of the pion is determined according to the spectral function. A problem about the implementation is that we only modified the pions, which come out of those resonances, which decay into $N\pi$ and which come from the reaction $NN \to NN\pi$. That means that the Fritiof model is producing on-shell pions and that the meson resonances decay into on-shell pions, as well as some of the baryon resonances (see Tab. 2.1 for the decay channels). In Fig. 6.3 we see the number of pions per energy as a function of energy in order to show the importance of the string

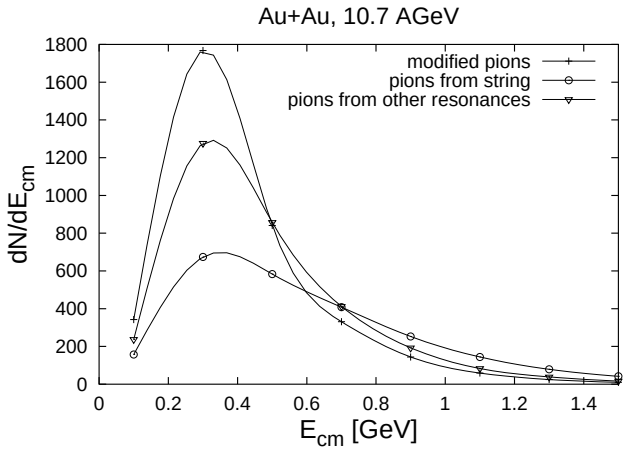

Figure 6.3: Number of pions from string decays and resonance decays per energy as function of the center of mass energy in Au+Au at 10.7 A·GeV at b=1 fm.

channel and the resonances, as for example the ρ, which have not been modified. We see that almost half of the pions are modified and therefore it is hard to predict the change which is induced by modifying the other half.
In order to get the pions back on their mass shell when they enter the vacuum, a scalar so called off-shell potential s_π is introduced. That potential has the following form

$$s_\pi(\vec{r},t) = \frac{M_\pi(t_{cr}) - m_\pi}{\rho_N(\vec{r}(t_{cr}), tcr)} \rho_N(\vec{r}(t), t), \tag{6.8}$$

where ρ_N is the density of nucleons in the local restframe of nuclear matter and t_{cr} is the creation time of the pion. The pion mass at time t is given by

$$M_\pi(t) = m_\pi + s_\pi(\vec{r},t), \tag{6.9}$$

which fulfills the desired requirements.
Figure 6.4 shows the results of our model in the standard mode and with the implementation of off-shell pions at an incident energy of 10.7 GeV in Au+Au. We see that the pion rapidity spectrum is not altered at all and the influence on the kaon spectrum is very small and can also be driven by statistics. In Fig. 6.5 we see the mass spectrum of all pions, which have been modified at some point of the collision. It is pretty symmetric about the on-shell mass and therefore we expect the average invariant energy of the system to stay the same. By looking at the number of collisions as a function of energy, we indeed saw that this quantity was not changed. A reason for that might be that just modifying the resonance decays as described above might not be enough and one also has to modify the string model and the other resonances. However since the effect on the collision dynamics is so small, it might also be that the pion masses are just not shifted enough in order to induce a change in such a big system.

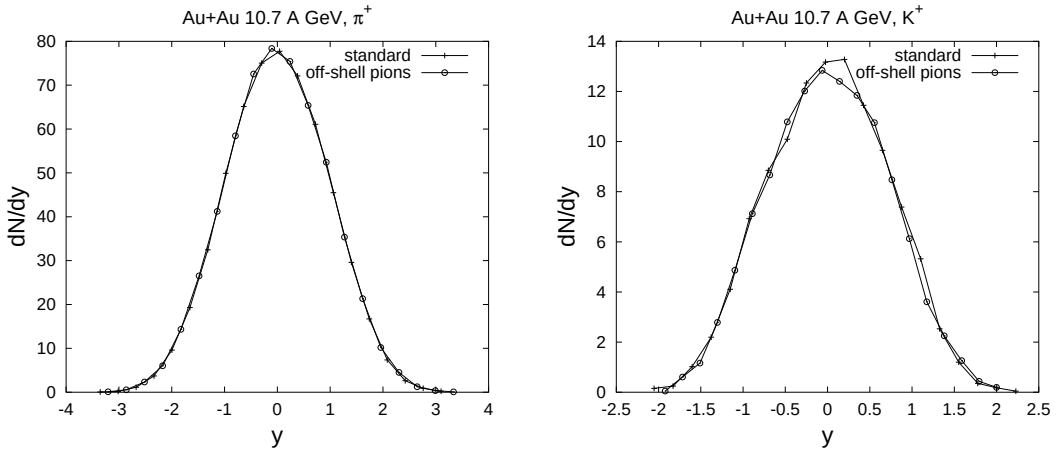

Figure 6.4: Rapidity spectrum of π^+ and K^+ in Au+Au at 10.7 GeV and impact parameter b=1 fm with off-shell pions in comparison to the standard calculations.

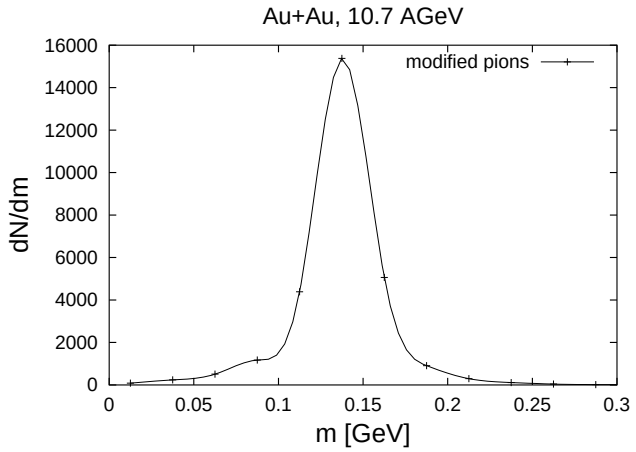

Figure 6.5: Mass spectrum of all modified pions during the whole collision in Au+Au at 10.7 A·GeV.

6.2 Resonance lifetimes

Usually the lifetime of the resonances is assumed to be given by

$$\tau = \frac{1}{\Gamma}. \tag{6.10}$$

In Chapter 2 we explained that in our model we propagate resonances explicitly and in that case the lifetime does not have to coincide with Eq. (6.10). The lifetime of a resonance as the intermediate state of a two body scattering depends on the relation between its width and the energy spread of the incoming particles ΔE [Joa75]. In general the lifetime of a resonance is given by

$$\tau = \frac{d\delta(E)}{dE}, \tag{6.11}$$

where E is the center-of-mass energy. That lifetime is the time delay of the wave packet due to the scattering. In [Leu01] Eq. (6.11) has been generalized to the decay of the Δ resonance with multiple final channels. In our model we take into account $\Delta \to N\pi$ and $\Delta \to N^{-1}NN$, where the second process is just another way of writing $N\Delta \to NN$. The result for the lifetime in [Leu01] is

$$\tau = \frac{1}{2}A(1-K), \tag{6.12}$$

with

$$A(\omega,\vec{p}) = \frac{\Gamma(\omega,\vec{p})}{(\omega - \vec{p}^2/2m - \mathrm{Re}\Sigma^+(\omega,\vec{p}))^2 + \Gamma^2(w,\vec{p})/4} \tag{6.13}$$

being the spectral function and

$$K \equiv \frac{\partial \mathrm{Re}\Sigma^+(\omega,\vec{p})}{\partial\omega} + \frac{\omega - \vec{p}^2/2m - \mathrm{Re}\Sigma^+(\omega,\vec{p})}{\Gamma(\omega,\vec{p})}\frac{\partial\Gamma(\omega,\vec{p})}{\partial\omega}, \tag{6.14}$$

where $\Gamma(\omega,\vec{p}) = -2\mathrm{Im}\Sigma^+(\omega,\vec{p})$. In the calculations we neglected $\mathrm{Re}(\Sigma^+)$ and for the Δ width we used the vacuum decay width with a parametrization from [EBM99]

$$\Gamma = \Gamma_0 \left(\frac{q}{q_0}\right)^3 \frac{m_\Delta}{E_{\mathrm{c.m.}}}\frac{\beta_0^2 + q_0^2}{\beta_0^2 + q^2} \tag{6.15}$$

with q being the pion momentum in the restframe of the Δ, $q_0 \equiv q(m_\Delta)$, $\Gamma_0 = 0.118$ GeV, and $\beta_0 = 0.2$ GeV. In Fig. 6.6 we see the dependence of the Δ lifetime as a function of the center-of-mass energy of the pion and the nucleon, where one can clearly see a difference. In the calculations we also changed all other resonances by using the same formula, but with the parameter of the respective resonance.

In the final results however one does not see a difference. In Fig. 6.7 we see that

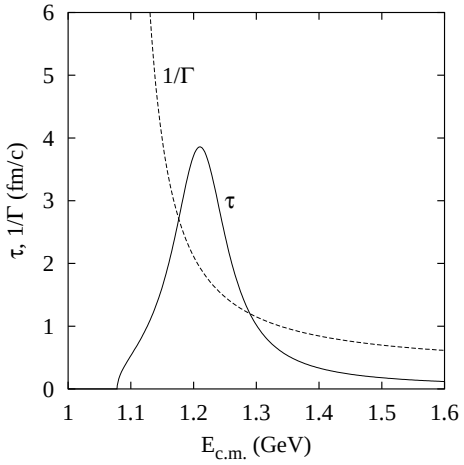

Figure 6.6: Resonance life time as a function of center-of-mass energy.

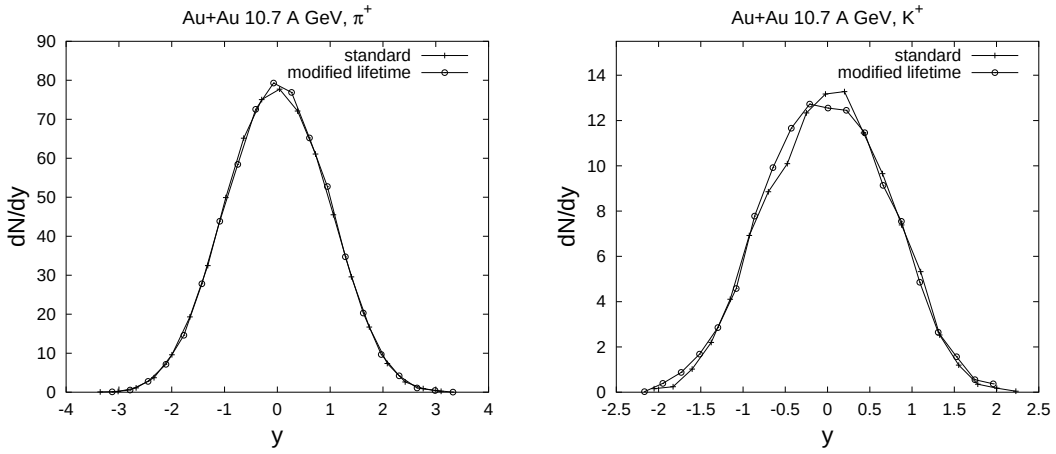

Figure 6.7: Pion and kaon rapidity spectra in Au+Au at 10.7 A·GeV with modified resonance lifetimes in comparison to the standard calculation.

there is no influence on the kaon and pion production. Again we looked at the number of collisions as a function of energy and again there was no significant change. One reason might be that in average the lifetime of the Δ is not changed, since, as we see in Fig. 6.6, the lifetime of the Δ is sometimes enhanced and sometimes suppressed. Another reason might again be that the change is just too small to change the dynamics of the complex system significantly. A similar very weak influence of the Δ lifetime choice on heavy-ion collisions at 1-2 A·GeV was reported in [LELU02].

6.3 String-String collisions

In collisions with an invariant energy above 2.6 GeV in case of a baryon-baryon collision and 2 GeV in case of a meson colliding with a baryon, we simulate events with the Fritiof string model. As already explained, the particles in the string have a formation time and during that time only the leading particles inside the string are allowed to scatter with a reduced cross section (see Chapter 3). Now we want to modify that picture slightly. We will divide the formation time into two parts, the production time and the new formation time. The production time is the time in which the string is treated as kind of a high resonance, which is explicitly propagated and which then decays according to the Lund fragmentation. In the standard picture the string immediately starts to decay and we only treat it through its decay products. Now we add another way of existence to a string life by introducing the production time. During that time we will treat the string as a single object, which can collide with other strings and particles. After that time we use the same description as before. The only difference is that the new formation time is shorter in such a way that if one adds the production and the new formation time, the old formation time is recovered. In the following we will discuss the details of the implementation and the choice of the new parameters.
First of all we have to pin down the value of the production time. This is for sure a very small time and we choose it to be

$$t_{\text{prod}} = 0.2\,\text{fm} \tag{6.16}$$

in the restframe of the string, which is of the order of the time steps, we are using in our simulation. So after the Fritiof model has produced a string, it is propagating as all other particles. We choose the value of the cross section with all other objects to be

$$\sigma_{\text{string-string}} = \sigma_{\text{string-particle}} = 30\,\text{mb}. \tag{6.17}$$

This value is of the order of the inelastic cross section for NN scattering at invariant energies above the threshold for string production. In order to preserve

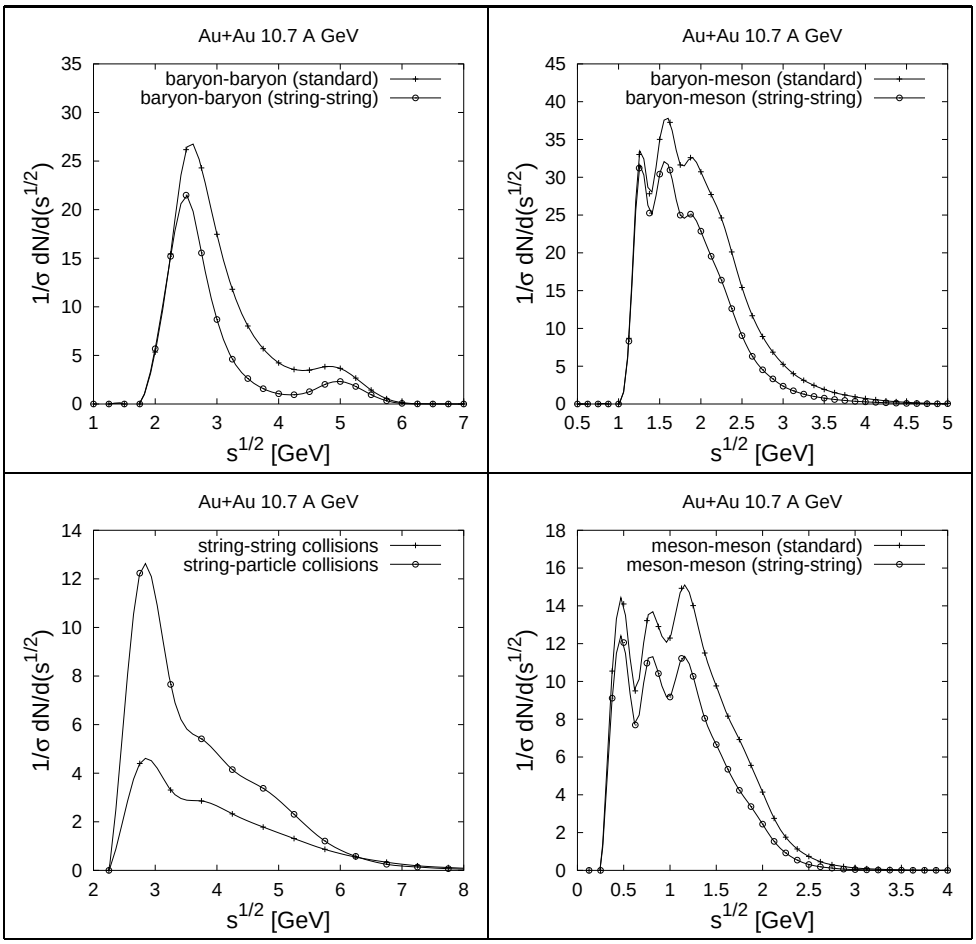

Figure 6.8: Number of collisions normalized to the total cross section as a function $\sqrt{s}$ in Au+Au at 10.7 A·Gev and b=1 fm in different channels.

baryon number we distinguish between baryon strings and meson strings, which are of course created out of baryons and mesons, respectively. In case of two colliding baryon strings we get two new baryon strings, which are treated the same way as all other strings. In case of a baryon string colliding with a meson string, we get with equal probability either one baryonic string or one mesonic and one baryonic string. The decay of the strings after the production time is then done by jetset as before.

In Fig. 6.8 we see the number of collisions divided by the total cross section as a function of $\sqrt{s}$. We see indeed that the string-string collisions take place at a higher invariant energy in comparison to the other channels. The number of collisions is also quite comparable to the other channels. On the other hand we also notice that the number of reactions in the other channels decrease. The reason is of course that the produced particles now live in the string for a while and

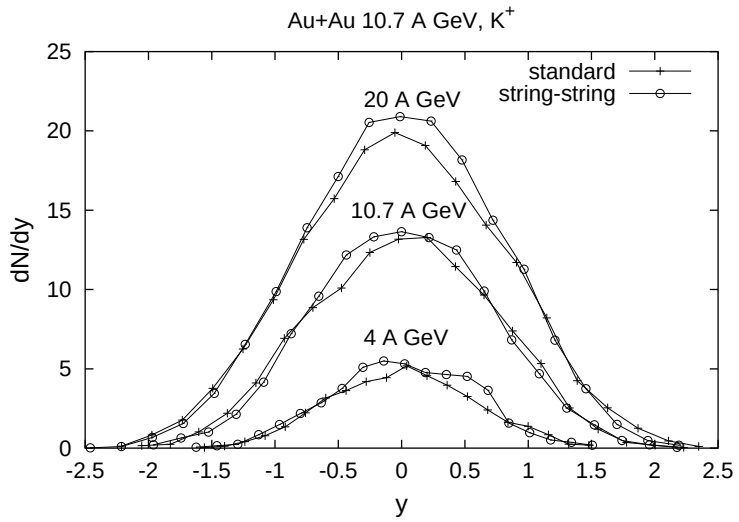

Figure 6.9: K^+ rapidity spectra in Au+Au at 4 A·GeV, 10 A·GeV and 20 A·GeV with and without string-string collisions.

they are not available as collision partners. This reduction in the other channels is quite sizeable, especially if one recalls that the cross sections for strangeness production in e.g. the meson-meson channels is pretty high above the threshold of about 1 GeV in comparison to other channels. Therefore we can understand why the rapidity spectra of π^+ and K^+ in Fig. 6.9 and Fig. 6.10 show no significant change. We compared rapidity spectra at three different energies in order to investigate the influence of the number of strings. The number of strings is of course higher at higher energies but obviously the results are not sensitive to that. We also looked at the m_t spectra for pions and kaons and again we did not find a change.

An advantage about the stiffness of the model against the changes is that we can gain more trust in the results of the model. The drawback is that those results do not describe all of the data and so some changes are necessary. Another drawback is that we can neither exclude nor prove the existence of certain processes or medium modifications.

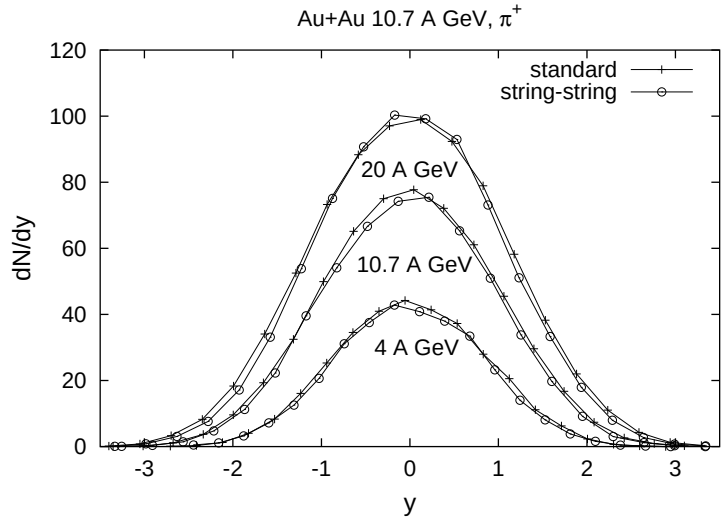

Figure 6.10: π^+ rapidity spectra in Au+Au at 4 A·GeV, 10 A·GeV and 20 A·GeV with and without string-string collisions.

Chapter 7

Summary and Outlook

In this work we have performed a systematic study of kaon and pion production in heavy-ion collisions at energies in the range from 2 A·GeV to 40 A·GeV within the BUU model. The first chapters were devoted to the presentation of our model and the description of the new implementations. Then we studied the influence of the system size at energies around 10 A·GeV, the particle production as a function of energy and the influence of off-shell pions, Δ lifetime and string-string collisions.
The system size dependence showed no ambiguities for K^+ and we reproduced the rapidity spectra in p+Au and Si+Au very well. The number of K^+ as a function of centrality in Au+Au at 10.7 A·GeV were also predicted nicely. Only in p+Be and in pp collisions at lower energies we overestimated K^+. This was improved by employing a lower strangeness suppression factor, but at the same time the agreement in p+Au, Si+Au and Au+Au for K^+ got worse. The K^- yields on the other hand were overestimated in almost all systems and here a reduced suppression factor is favored. The overshooting in bigger systems at higher energies, however, is more likely to be due to the meson-meson cross section as pointed out in Chapter 5. The pion yields also started to deviate as we increased the system size and there was a clear sign that our cascade model misses some kind of reaction dynamics, which reduces pions.
The excitation functions for the pions, kaons, lambdas and sigmas were studied in Chapter 5. The biggest deviation appeared again in the results for pions. Here we could confirm the results, which have already been obtained by HSD and UrQMD, namely that the π^+ are overestimated at all energies. Due to the high number of pions we could not reproduce the peak in the K^+/π^+ ratio, but we are close to the statistical model. The disagreement with data is also not big enough to make any statement on the appearance of new physics. Since the kaon yields could be reproduced, the reason for the peak does not seem to be strangeness enhancement but 'pion reduction'.
The modifications we implemented in Chapter 6 did not have a significant influence on the particle production, which shows that the influence of the secondary

collisions is pretty robust against small changes. The idea behind all those modification has been to increase the invariant energies of the collisions in order to enhance the production of heavy particles. Since the densities in high-energy heavy-ion collisions are very high, medium modifications or multi particle collisions become more and more probable. Unfortunately the system is too complex in order to get a clean sign for one of those effects.
Another problem is the string model. We saw that the string model has already problems in describing excitation functions of the elementary reactions. However, the spectra in p+Be and especially in p+Au looked better and therefore the averaged cross section of pp and pn seems to be well produced. If that is the case and there is such a difference between np and pp reactions, the question is of course how nn reactions behave. In a heavy-ion collision, those will be the most frequent collisions. Therefore it is very difficult to trace back the reasons for the deviations in the excitation functions for Au+Au collisions. Thus it would be reasonable to spend some thoughts on a better description of the elementary reactions since they are one of the foundations of a transport model. A problem with that is of course that for most channels like almost all baryon-meson and meson-meson channels, there is no data and therefore it will be difficult to say if a model is describing the elementary reactions right. However, it should at least be able to describe the data on pp collisions, which is available.
An interesting and important point is that in the elementary reactions and in small systems, we always overestimated kaons and underestimated the pions. As the system size increases, we see the opposite effect and we overestimate pions and underestimate kaons. That is a clear sign of reaction dynamics which have not been completely understood and which will be interesting to study further.
Another open problem in our model is the potential at AGS energies. In our model we overestimated all particle yields at the lower AGS energies and our stopping was too high. That seems very much to be due to the missing potential, which should be investigated.
The potential might also be important for the generation of the additional pressure, which we seem to miss by looking at the K^+ slopes as a function of energy. Here we also confirmed calculation by other transport models that the K^+ slopes are underpredicted in heavy-ion collisions at those energies. Here it will be interesting to study whether this increase of the slopes is due to some pre-hadronic phase or if it can be explained in hadronic terms.
Due to the high abundance of particles, the energy range from 2 A·GeV to 40 A·GeV seems to be very well suited for the study of the strong interactions. An interesting mechanism, which might influence the model predictions, is the multi particle scattering. Those reactions are also important in order to fulfill detailed balance in case of the string model and they are another way to gather more energy in one collision and therefore increase the production of heavy particles and the pressure in the system. However, it is questionable and it will be interesting to further investigate if at those high densities a description in terms of hadrons

is still reasonable or if one deals with some kind of pre-hadronic phase.
The question, which was raised in the introduction, if there is a sign for a quark-gluon plasma, cannot be answered for the reasons mentioned above.

Appendix A

Deutsche Zusammenfassung

Eines der Ziele der Schwerionenphysik ist die Entdeckung des Quark-Gluon Plasma. Bei einer Einschussenergie von etwa 30 A·GeV ist die Dichte in einer Schwerionenkollision am höchsten und ein Phasenübergang von hadronischen Freiheitsgraden zum Quark-Gluon Plasma ist möglich. Wir untersuchten in dieser Arbeit Schwerionenkollisionen mit Hilfe eines Transportmodells in einem Energiebereich zwischen 2 und 40 A·GeV und suchten nach Anzeichen für diesen Phasenübergang. Eines der möglichen Anzeichen ist eine erhöhte Produktion von Strangeness, da strange Quarks leichter durch die Fusion von Gluonen in einem Quark-Gluon Plasma erzeugt werden, als in hadronischen Reaktionen. Experimente haben in der Tat ein Maximum im K^+/π^+ Verhältnis als Funktion der Energie bei etwa 30 A·GeV gefunden.
Die ersten zwei Kapitel dieser Arbeit galten der Präsentation des BUU Transportmodells, das auf der BUU Gleichung basiert. Da wir, wie gesagt, dieses Modell bei Energien zwischen 2 und 40 A·GeV einsetzen, verlassen wir teilweise den Resonanzbereich und verwenden für diese Kollisionen bei höheren Energien das Fritiof String Modell. Das Modell wurde anschliessend an Systemen mit steigender Grösse getestet. Angefangen bei pp Kollsionen, über pA Reaktionen zu Schwerionenkollisionen wurden die Rapiditätspektren von Pionen und Kaonen mit den experimentellen Daten verglichen. Dabei war auffällig, das, obwohl die Pionen in elementaren Reaktionen unterschätzt wurden, bei steigender Systemgrösse die Pionen überschätzt wurden.
Anschliessend untersuchten wir die Produktion von Pionen und Kaonen als Funktion der Einschussenergie. Dort stellten wir wiederum fest, das wir zu viele Pionen produzieren, was frühere Rechnungen mit anderen Transportmodellen, HSD und UrQMD, bestätigte. Ebenso auffällig war, dass obwohl wir die K^+ zufriedenstellend beschreiben, die K^- überschätzt werden. Unser berechnetes K^+/π^+ Verhältnis ist in guter Übereinstimmung mit dem thermischen Modell, allerdings wird das Maximum bei 30 A·GeV nicht reproduziert. Die Abweichung ist jedoch nicht gravierend genug, um eine Aussage über Hinweise auf die Existenz oder das Ausschliessen eines Quark-Gluon Plasmas zu treffen. Eine grössere Abweichung

fanden wir in den K^+ 'slopes' als Funktion der Energie. Das rasche Ansteigen der 'slopes', welches man in den Daten beobachtet, konnte nicht reproduziert werden. Ebenso unterschätzen wir die 'slopes' bei allen Energien, während in elementareren Reaktionen, wie p+Be oder p+Au, keine Probleme auftraten. Dies bestätigt wiederum Rechnungen mit den Transportmodellen HSD und UrQMD und man spekuliert, dass der zusätzliche Druck durch prähadronische Freiheitsgrade in der Frühphase der Kollision hervorgerufen wird.
Im letzten Kapitel untersuchten wir die Einflüsse von Off-shell Pionen, Resonanz Lebensdauern und String-String Kollisionen, konnten aber keine Auswirkung auf die Spektren von Kaonen und Pionen finden.
Es wird interessant sein, in der Zukunft neue Daten in dem Energiebereich zwischen 2 und 40 A·GeV zu bekommen, um die Frage nach prähadronischen Freiheitsgraden und dem Phasenübergang zu hadronischen Freiheitsgraden genauer zu untersuchen.

Bibliography

[A+73] M. Antinucci et al., *Multiplicities of charged particles up to ISR energies*, Lett. al Nuovo Cimento **6** (1973), 121.

[A+94] T. Abbott et al., *Charged hadron distributions in central and peripheral Si+A collisions at 14.6 AGev/c*, Phys. Rev. C **50** (1994), no. 2, 1024.

[A+96] S. Ahmad et al., *Lambda production by 11.6 GeV/c Au beam on Au target*, Phys. Lett. B **382** (1996), 35.

[A+99] L. Ahle et al., *Simultaneous multiplicity and forward energy characterization of particle spectra in Au+Au collisions at 11.6A GeV/c* , Phys. Rev. C **59** (1999), no. 4, 2173.

[A+00a] L. Ahle et al., *An Excitation Function of K^- and K^+ Production in Au+Au Reactions at the AGS*, Phys. Lett. B **490** (2000), 53.

[A+00b] L. Ahle et al., *Excitation Function of K^+ and π^+ Production in Au+Au Reactions at 2-10 A·GeV*, Phys. Lett. B **476** (2000), 1.

[A+02] S.V. Afanasiev et al., *Energy dependence of pion and kaon production in central Pb+Pb collisions*, Phys. Rev. C **66** (2002), 054902.

[Abb92] T. Abbott, *Measurement of particle production in proton induced reactions at 14.6 GeV/c*, Phys. Rev. D **45** (1992), 3906–3920.

[And87] B. Andersson, *A Model for low-p_t Hadronic Reactions with Generalizations to Hadron-Nucleus and Nucleus-Nucleus Collisions*, Nucl. Phys. B **281** (1987), 289.

[And98] Bo Andersson, *The Lund model*, Cambridge Univ. Press, 1998.

[Ant99] F. Antiori, *Production of strange and multistrange hadrons in nucleus-nucleus collisions at the SPS.*, Nucl. Phys. A **661** (1999), 130–139.

[B+73] V. Blobel et al., *Multiplicities, topological cross sections, and single particle inclusive distributions from pp interactions at 12 and 24 GeV/c*, Nucl. Phys. B **69** (1973), 454–492.

[BFMM88] A. Baldini, V. Flaminio, W.G. Moorhead, and D.R.O. Morrison, *Landolt-Börnstein*, vol. 12, Springer, Berlin, 1988.

[BKWX91] G.E. Brown, C.M. Ko, Z.G. Wu, and L.H Xia, *Kaon production from hot and dense matter formed in heavy-ion collisions*, Phys. Rev. C **43** (1991), 1881.

[BM90] W. Botermans and R. Malfliet, *Quantum transport theory of nuclear matter*, Phys. Rept. **198** (1990), 115.

[BMCOR02] P. Braun-Munziger, J. Cleymans, H. Oeschler, and K. Redlich, *Maximum Relative Strangeness Content in Heavy-Ion Collisions Around 30 A·GeV*, Nucl. Phys. A **697** (2002), 902–912.

[BMRS03] P. Braun-Munziger, K. Redlich, and J. Stachel, *Particle production in heavy-ion collisions*, nucl-th/0304013 v1 (2003).

[BSS+04] E.L. Bratkovskaya, S. Soff, H. Stöcker, M. van Leeuwen, and W. Cassing, *Evidence for nonhadronic degrees of freedom in the transverse mass spectra of kaons from relativistic nucleus-nucleus collisions?*, Phys. Rev. Lett. **92** (2004), no. 3, 032302.

[C+00] C. Caso et al., *(Review of Particle Properties)*, Eur. Phys. J. C **15** (2000).

[Cas02] W. Cassing, *Antibaryon production in hot and dense nuclear matter*, Nucl. Phys. A **700** (2002), 618–646.

[CB99] W. Cassing and E.L. Bratkovskaya, *Hadronic and electromagnetic probes of hot and dense nuclear matter*, Phys. Rept. **308** (1999), 65–233.

[CBM+97] W. Cassing, E.L. Bratkovskaya, U. Mosel, S.Teis, and A. Sibirtsev, *Kaon versus antikaon production at SIS energies*, Nucl. Phys. A **614** (1997), 415.

[Dan84] P. Danielewicz, *Quantum theory of nonequilibrium processes. I.*, Ann.Phys. **152** (1984), 239.

[DDG+73] S.P. Denisov, S.V. Donskov, Yu.P. Gorin, R.N. Krasnokutsky, A.I. Petrukhin, Yu.D. Prokoshkin, and D.A. Stoyanova, *Absorption cross sections for pions, kaons, protons and anti-protons on complex nuclei in the 6 GeV/c to 60 GeV/c momentum range*, Nucl. Phys. B **61** (1973), 62.

[EBM99] M. Effenberger, E.L. Bratkovskaya, and U. Mosel, *e^+e^--pair production from γA reactions*, Phys. Rev. C **60** (1999), 044614.

[Eff99] M. Effenberger, *Eigenschaften von Hadronen in Kernmaterie in einem vereinheitlichten Transportmodell*, Ph.D. thesis, Justus-Liebig-Universität Giessen, 1999.

[EW88] T. Ericson and W. Weise, *Pions and Nuclei*, Clarendon Press Oxford, 1988.

[Fal] T. Falter, *PH.D. thesis*, to be published.

[Fri03] V. Friese, *Strangeness from 20 AGeV to 158 AGeV*, Preprint nucl-ex/0305017 v1 (2003).

[Gei98] Jochen Geiss, *Die Produktion von Strangeness und Charmonium in Kern-Kern Kollisionen*, Ph.D. thesis, Justus-Liebig-Universität, Giessen, 1998.

[GM83] N.K. Glendenning and T. Matsui, *Creation of $q\overline{q}$ pairs in a chromoelectric flux tube*, Phys. Rev. D **28** (1983), no. 11, 2890.

[GR96] M. Gaázdzicki and D. Röhrich, *Strangeness in Nuclear Collisions*, Z. Phys. C **71** (1996), 55–63.

[Joa75] Joachain, *Quantum collision theory*, North Holland Publishing Company, 1975.

[K+84] T. Kodama et al., *Causality and relativistic effects in intranuclear cascade calculations*, Phys. Rev. C **29** (1984), 2146.

[KB62] L.P. Kadanoff and G. Baym, *Quantum statistical mechanics*, Benjamin, New York, 1962.

[KHu] KHuK, *Hadronen- und Kernphysik 2003, Status und Perspektiven.*

[KL95] Che Ming Ko and Bao-An Li, *Formation of superdense matter in high energy heavy-ion collisions*, Phys. Rev. C **52** (1995), no. 4, 2037.

[LCGM00] A.B. Larionov, W. Cassing, C. Greiner, and U. Mosel, *Squeeze-out of nuclear matter in peripheral heavy-ion collisions and momentum-dependent effective interactions*, Phys. Rev. C **62** (2000), 064611.

[LELU02] A. B. Larionov, M. Effenberger, S. Leupold, and U.Mosel, *Resonance lifetime in Boltzmann-Uehling-Uhlenbeck theory: Observable consequences*, Phys. Rev. C **66** (2002), 054604.

[Leu01] S. Leupold, *Lifetime of resonances in transport simulations*, Nucl.Phys. A **695** (2001), 377.

[LM02] A.B. Larionov and U. Mosel, *Off-shell pions in Boltzmann-Uehling-Uhlenbeck transport theory*, Phys. Rev. C **66** (2002), 034902.

[LM03] A.B Larionov and U. Mosel, *The $NN \longrightarrow N\Delta$ cross section in nuclear matter*, Nucl. Phys. A **728** (2003), 135–164.

[M+02] A. Mischke et al., *Lambda production in central PB+PB collisions at CERN SPS energies*, J. Phys. G **28** (2002), 1761.

[M+03] A. Mischke et al., *Energy dependence of lambda and anti-lambda production at CERN SPS energies*, Nucl. Phys. A **715** (2003), 453–457.

[MS92] D.M. Manley and E.M. Saleski, *Multichannel parametrization of πN scattering amplitudes*, Phys. Rev. D **45** (1992), 4002.

[Pin02] C. Pinkenburg, *Production and collective behaviour of strange particles in Au+Au collisions at 2 A·GeV - 8 A·GeV*, Nucl. Phys. A **698** (2002), 495–498.

[RM82] J. Rafelski and B. Müller, *Strangeness Production in the quark-gluon plasma*, Phys. Rev. Lett. **48** (1982), 1066.

[WBCS03] H. Weber, E.L. Bratkovskaya, W. Cassing, and H. Stöcker, *Hadronic observables from SIS to SPS energies - anything strange with strangeness?*, Phys. Rev. C **67** (2003), 014904.

[Web02] Henning Weber, *Untersuchung der Hochddichtephase von relativistischen Schwerionenkollisionen*, Ph.D. thesis, Johann Wolfgang Goethe - Universität, Frankfurt, 2002.

[Wer93] K. Werner, *Strings, Pomerons, and the Venus model of hadronic interactions at ultrarelativistic energies*, Phys. Rept. **232** (1993), 87–299.

[WLS+99] F. Wang, H. Liu, H. Sorge, N. Xu, and J. Yang, *Sytematic study of the kaon to pion multiplicity ratios in heavy-ion collisions*, nucl-th/9909001 (1999).

[WPK+88] G.M. Welke, M. Prakash, T.T.S. Kuo, S. Das Gupta, and C. Gale, *Azimuthal distributions in heavy-ion collisions and the nuclear equation of state*, Phys. Rev. C **38** (1988), 2101.

Acknowledgments

I am especially thankful to Prof. Dr. Ulrich Mosel for putting me up in his institute and for his dedicated support. His advices and the numerous discussions were of crucial importance for the success of that work. I am also grateful for the possibilities, Prof. Dr. Ulrich Mosel offered me, to attend international workshops, conferences and lecture weeks.
I also want to thank Alexei Larionov, who always took the time to answer any kind of question, which have been arising during my diploma thesis. The numerous discussions on many physical topics have been very valuable for that work. Special thanks also go to Thomas Falter for answering any kind of question and for implementing his treatment on formation times in my code. The manifold discussions with him on the string model also improved my understanding for that model.
I am also thankful to Prof. Dr. Dr. Cassing for pointing out important improvements on the model and for answering and discussing physical questions. I also thank Prof. Dr. Carsten Greiner for the interest in my work and for valuable discussions.
Since I had to perform a lot of numerical calculations in that work, a special thank goes to the computer administration team, Prof. Dr. Horst Lenske, Christoph Keil and Frank Frömel, who provided the stability of the computational resources.
A special thank also goes to my room mate Oliver Buss for the excellent atmosphere in our office and the discussion with him on a variety of physical questions always have been productive.
I am also thankful to my family who supported me in any kind of unphysical problems. I also thank my room mates at home, who always respected my work.
Last but not least, I also thank Elke Jung, who was a great help in any kind of bureaucratic affairs.

Ich versichere, dass ich die vorliegende Arbeit selbständig, ohne andere als die angegebenen Hilfsmittel und Quellen verwendet zu haben, verfasst habe.

Giessen, den